THE ENERGY SPECTRUM OF ULTRA HIGH ENERGY COSMIC RAYS

by

Tareq Ziad AbuZayyad

A dissertation submitted to the faculty of
The University of Utah
in partial fulfillment of the requirements for the degree of

Doctor of Philosophy

Department of Physics

The University of Utah

May 2000

THE UNIVERSITY OF UTAH GRADUATE SCHOOL

SUPERVISORY COMMITTEE APPROVAL

of a dissertation submitted by

Tareq Ziad AbuZayyad

This dissertation has been read by each member of the following supervisory committee and by majority vote has been found to be satisfactory.

Chair: Charles C. H. Jui

Carleton DeTar

Steve Krueger

Pierre Sokolsky

Orest Symko

THE UNIVERSITY OF UTAH GRADUATE SCHOOL

FINAL READING APPROVAL

To the Graduate Council of the University of Utah:

I have read the dissertation of Tareq Ziad AbuZayyad in its final form and have found that (1) its format, citations, and bibliographic style are consistent and acceptable; (2) its illustrative materials including figures, tables, and charts are in place; and (3) the final manuscript is satisfactory to the Supervisory Committee and is ready for submission to The Graduate School.

Date	Charles C. H. Jui Chair, Supervisory Committee

Approved for the Major Department

Valy Vardeeny
Chair/Dean

Approved for the Graduate Council

David S. Chapman
Dean of The Graduate School

ABSTRACT

The Energy Spectrum of Ultra High Energy Cosmic Rays is measured by the first of two High Resolution Fly's Eye detectors in the monocular mode. The data set collected in the period of May 1997 to June 1999 was used for the measurement. A new reconstruction procedure (profile constrained geometry fit) was developed to analyze the data. This procedure gives reasonably good energy resolution, but poor x_{max} resolution. Resolution and systematics are discussed in the thesis. The spectrum measurement results are consistent with previous measurements in normalization and general shape. The spectrum appears to continue beyond the Greisen-Zatsepin-Kuz'min cutoff.

To my parents Haifaa and Ziad AbuZayyad

CONTENTS

CHAPTERS

LIST OF TABLES

LIST OF FIGURES

ACKNOWLEDGEMENTS

I wish to thank my advisor Prof. Charles C. H. Jui for his invaluable help. He guided me throughout my work with the HiRes group and taught me alot about "doing physics". Thanks also to John Mathews and Stan Thomas who were instrumental in getting the detector up and running. In his capacity as program manager, John has been the person to go to whenever I had a non physics-related problem and he was always helpful. Thanks also to Lawrence Wiencke for his help with the atmospheric analysis.

I also wish to thank Hongyue Dai and Matthew Kidd for many useful discussions early on in my work, as well as, for their well written analysis code which I used as a basis for much of my own programs. I owe thanks to many other members of the HiRes group who have helped with the detector construction, operation, and running, as well as, with all the usual tasks an experiment at this scale demands.

My graduate studies have kept me away from my home and family for a long time. I wish to express my most sincere appreciation for my parents, brothers, and sisters for their emotional support and their patience.

This research was funded by the National Science Foundation through its support of research at the University of Utah. Finally I would like to thank the US Army Dugway Proving Ground for hosting the HiRes detector sites.

CHAPTER 1

INTRODUCTION

Cosmic Rays (CR) measurements focus on three areas: energy spectrum, composition, and anisotropy. The energy spectrum refers to the variation of the observed flux with energy; composition, the particles species (p,He,...); and anisotropy, the distribution of arrival directions of the particles over the sky.

The flux of CR at the highest energies is too low for direct measurement to be practical. Indirect measurements are, however, possible. High energy cosmic rays interact with the atmosphere to produce Extensive Air Showers (EAS). These showers can be detected by ground arrays of scintillation detectors spread out over a large area or by optical detectors which observe the fluorescence light emitted by atmospheric Nitrogen molecules in response to the passage of charged particles of the shower. Fluorescence light is emitted isotropically. Hence, a localized detector can observe a large volume of the atmosphere and achieve an acceptance similar to that of a large ground array, even with the $\sim 10\%$ duty cycle of fluorescence detectors. Recall that, fluorescence detectors only take data on clear moonless nights, while ground arrays operate continuously.

The High Resolution Fly's Eye (HiRes) is a fluorescence detector. It was designed to study the spectrum, composition and anisotropy of CR with energies above 3×10^{18} eV. HiRes comprises a number of detector units, each consisting of a mirror (light collector), a cluster of photo-multiplier tubes at the focal plane, and readout electronics. The detector units are located at two sites (eyes) separated by a distance of 12.6 km. The division of mirrors among two sites allows for "stereo" observation of an EAS which allows a more accurate reconstruction than would be possible with a single eye. Although "stereo" mode is the preferred mode of operation of HiRes, each eye can act as an independent detector running in "monocular" mode.

This dissertation reports on the first results from the monocular observations made by the HiRes-I site between 1997 and 1999. The second site has been under construction during this period and only recently began data-taking. Data collected by the first completed site of HiRes, referred to as HiRes-I or BigH, was used to study the energy spectrum above 3×10^{18} eV. In particular, to look for the Greisen-Zetsepin-Kuz'min (GZK) cutoff at 6×10^{19} eV.

1.1 Organization

Below is an outline of the contents of this thesis. Each chapter begins with an overview of the material in that chapter.

Chapter 2 provides the science objectives of the spectrum measurement. A brief review of high energy cosmic rays physics is presented. The measured properties of CR are related to the questions of origin, acceleration, and propagation, which are the central questions from the point of view of High Energy Astrophysics. A compilation of previous spectrum measurements is also presented. The last section introduces the idea of the GZK cutoff and discusses some of its implications.

Chapter 3 deals with extensive air showers in the atmosphere. This chapter provides a descriptive picture of shower development and discusses the various physical models and processes which explain the observed features of extensive air showers. EAS detection using the fluorescence method is introduced along with an outline of the procedure used to estimate the CR primary energy from the measured EAS properties.

Chapter 4 presents a description of the HiRes-I (BigH) detector. Details specific to BigH, such as the detector layout and optimization, are given. The HiRes detector and its various components are described in detail elsewhere. Where appropriate, I refer the reader to other references. However, some overlap with other documents is unavoidable.

Chapter 5 describes the detector calibration. Both the calibration systems and procedures are described. Emphasis is placed on the tube gain calibration using the "roving Xenon flasher". Atmospheric monitoring and calibration are also discussed.

Chapter 6 describes the detector Monte Carlo (MC). The detector Monte Carlo plays a major role in the spectrum measurement. The detector aperture and the energy resolution are calculated using the MC simulation. In the MC, as well as in the reconstruction programs, we employ models of shower development, light generation and transmission, the detector optics and electronics. Detailed descriptions of these models and the simulation of the tube response are given. For the most part, the same calculational steps are used for both the MC and reconstruction; differences between the MC and reconstruction codes are highlighted.

Chapter 7 provides an overview of the data analysis chain and describes the framework in which data analysis is performed. The raw data, data structures and programs used to manipulate the data are explained. Data analysis is broken down into consecutive stages or "passes". The first two passes are described in this chapter. These passes perform the event building from raw data packets (PASS0) and apply the calibration information to the tubes signals and trigger times (PASS1).

Chapter 8 continues with data analysis. After an introduction to shower reconstruction, this chapter describes each of the remaining data analysis "passes": The Rayleigh filter (PASS2), shower-detector plane fitting (PASS3), event filtering and selection (PASS3a, PASS3b), and finally, track and profile reconstruction (PASS4). The resolution of the reconstruction algorithms and the associated systematic effects are discussed.

Chapter 9 describes the calculation of the spectrum and shows results for the spectrum measurement. The chapter also contains a discussion of the results in relation to the GZK cutoff and the conclusions drawn from these results.

CHAPTER 2

UHECR PHYSICS

Cosmic rays from outside the solar system arrive at Earth with energies from $\sim 10^{9}$ eV up to and higher than 10^{20} eV. The observed flux appears to be isotropic. Cosmic rays with energies $\sim 10^{18}$ eV and higher are referred to as Ultra High Energy Cosmic Rays (UHECR). Our research, as the title of this thesis indicates, is primarily interested in this region of the energy spectrum.

Cosmic rays with energies less than $\sim 10^{18}$ eV are believed to be of galactic origin [1][2]. Particle acceleration in this case is provided by shock waves generated by supernovae explosions into the interstellar medium or the stellar wind of the exploding star [3]. Above 3×10^{18} eV, CR origin is not yet known. Several possible acceleration sites and mechanisms have been proposed. The most widely accepted of these is that, CR are accelerated in radio galaxy hot spots: shock waves generated by radio galaxies [3]. There are no known galactic sources of CR with energies above 10^{20} eV. Extra-galactic sources such as radio galaxies and active galactic nuclei could produce these particles, figure 2.1 examines the size and magnetic field constraints placed on UHECR sources. In the case of extra-galactic sources, the propagation of the UHECR from their source to earth becomes a problem because of the heavy energy loss they would incur from interactions with the Cosmic Microwave Background (CMB) radiation and other matter and radiation fields they encounter. The interaction with the CMB is responsible for the predicted GZK cutoff in the energy spectrum around 6×10^{19} eV. The recent review article by Beirmann [3] discusses various origin models, and should be consulted for a more thorough and complete discussion.

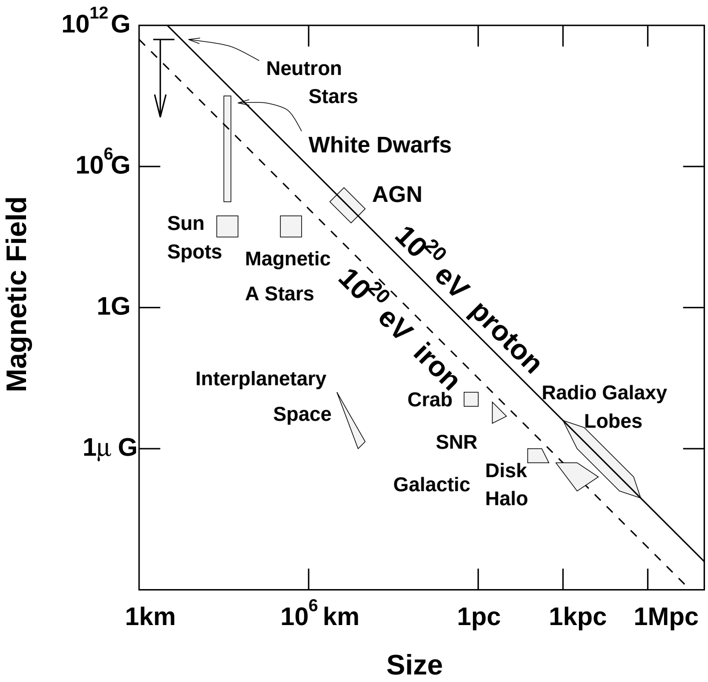

Figure 2.1. Hillas diagram of possible sources of $10^{20}\,eV$ cosmic rays. The maximum energy of a particle that can be accelerated by a given source increases with the size and the magnetic field in the accelerating region. [4]

The observed flux of CR is a strong function of energy. A flux on the order of 1 particle per cm^2 per steradian per hour at 10^{12} eV decreases to less than 1 particle per km^2 per steradian per year at 10^{20} eV. The energy spectrum follows roughly a power law with an index of ≈ -3 over the full energy range. The upper end of the spectrum is shown in figure 2.2. As can be seen from the figure, small spectral index changes are observed at three energies: at 3×10^{15} eV (the "knee"), between 10^{17} and 10^{18} eV where the spectrum steepens even further, and finally at 3×10^{18} eV (the "ankle") where the spectrum recovers to an index value of -2.7[4]. It is not yet known, whether the flux of CR terminates at some maximum energy or not. Greisen [5] and independently Zatsepin and Kuz'min [6] predicted that a cutoff should be present at $\sim\ 6 \times 10^{19}$ eV resulting from the interaction of high energy protons with the cosmic microwave background radiation. However, several events with energies above the predicted cutoff have been observed, leaving open the question of a maximum allowed energy. The highest reported energy for a CR event still stands at 3.2×10^{20} eV, for an event observed by the Fly's Eye detector in 1991[7]. The Greisen-Zatsepin-Kuz'min (GZK) cutoff is of central importance to this study, and will be discussed further.

2.1 Experiment and Theory

Before an interpretation of experimental results can be given in terms of theoretical models, a few points regarding the measurements should be clarified. Cosmic rays with energies greater than 10^{14} eV are observed indirectly, through the extensive air showers they generate in the atmosphere. The indirect nature of the measurement introduces many uncertainities, both experimental and theoretical, into the estimate of the primary CR particle's energy. For example, we are dependent on model calculations of shower development for the estiamte of the primary energy. Uncertainities in the geometrical reconstruction of the EAS track and atmospheric clarity are examples of experimental sources of uncertainity. The net result of these factors is that the CR energies can be estimated to within 20% at best.

Due to fluctuations in shower development, the primary particle type can not

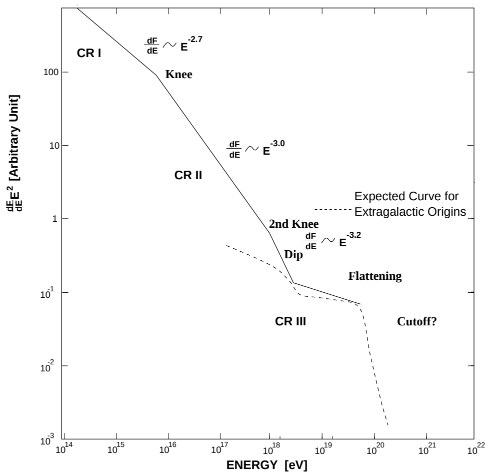

Figure 2.2. A schematic drawing of the energy spectrum of cosmic rays above $10^{14}\,eV$. [4]

be identified on an event-by-event basis. Therefore, composition is determined only on a statistical basis. Showers generated by different particle types differ slightly in their average behavior. Showers generated by iron nuclei develop higher in the atmosphere than those produced by protons. Furthermore the muon content of iron showers is, on average, greater than that of proton showers. These differences allows the identification of populations of “heavy” (iron,) and “light” (proton) primaries. The assignment of a particular event to either population can be done on the basis of how close the behavior of the particular event is to the average behavior.

Anisotropy studies are complicated by the presence of magnetic fields in the intersteller medium, which bend the path of a charged particle travelling through space. Irregularities in the magnetic field and the random nature of the deflections mean that, in general, the arrival direction of the particle does not point back to the particle’s point of origin. However, above 10^{19} eV, the gyroradius of a proton in the galactic magnetic field becomes larger than the galactic radius and thus the deflections to its path are small enough for its arrival direction to be a meaningful indicator of its origin.

Relating the observations to theoretical models is not difficult, at least at a qualitative level. At the knee region, for example, the steepening in the spectrum and the composition change from mixed to heavy can be understood in terms of CR propagation through the galaxy. According to a simple diffusion model (which has been revised to account for better understanding of the galactic magnetic field,) CR are confined well in the galaxy up to a critical energy $E_{cr} = HLZ \simeq 3 \times 10^{15}\, eV \times Z$, where H is the magnetic field strength, L is the length scale of the magnetic turbulence, and Z is the charge of the particle [8]. Above E_{cr}, cosmic rays more easily escape from the galaxy because of their increased gyroradius. This model predicts: (a) a decrease in the flux above the critical energy, (b) a change in the composition because of the charge dependence of the confinement efficiency, and (c) an enhancment in the anisotropy above the knee [8].

Anisotropy may be difficult to observe due to the scrambling of the arrival directions of CR by magnetic fields. Neglecting this complication for the moment, and if instead of asking for point sources, we merely classify the sources of cosmic rays as galactic, extragalactic but local (local supercluster of galaxies), or cosmological, then for each of the above we can expect to see, respectively, anisotropy towards the galactic plane, anisotropy towards the supergalactic plane, or an isotropic flux.

2.2 Recent results

The "knee" region is well below the energies of interest to HiRes. The interested reader is referred to the review article by Kalmykov and Khristiansen [8], which contains a detailed discussion of the knee region of the spectrum, in addition to the ultra high energy regime ($> 10^{18}$ eV). For the sake of completeness, it should be mentioned that, at the "knee", the spectrum steepens from a spectral index of -2.7 to -3.0. An apparent change from a mixed composition to a predominantly heavy composition has also been reported in the region $10^{14} - 10^{16}\, eV$ [9].

Above 10^{17} eV the Fly's Eye experiment measured the CR energy spectrum both in monocular (figure 2.3) and stereo (figure 2.4) modes [1]. The stereo spectrum shows more structure, in the region below 10^{19} eV, than the monocular spectrum, as a result of the improved resolution. On the other hand, the integrated monocular exposure of the monocular Fly's Eye detector was an order of magnitude greater than the stereo exposure. The 3.2×10^{20} eV event was seen only in the monocular sample.

The dip in the stereo spectrum at 3×10^{18} eV was observed by other experiments as well, although it was not as pronounced as the Fly's Eye's and was shifted up in energy slightly (Yakutsk [10], AGASA [11][12]). In addition to the spectrum results, Bird et. al, also reported a composition measurement in the same energy range, figure 2.5. The composition changes from heavy below $10^{17.5}$ eV to light around 10^{19} eV.

One possible explanation of the dip at 3×10^{18} eV in the stereo spectrum and the composition change is that the observed flux is the sum of two components: a heavier component of galactic origin dominating below 10^{18} eV, and a light extragalactic component taking over at energies greater than 3 EeV [1].

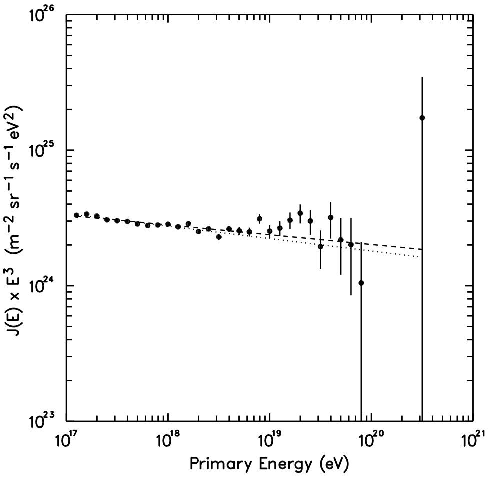

Figure 2.3. The Fly's Eye monocular spectrum.

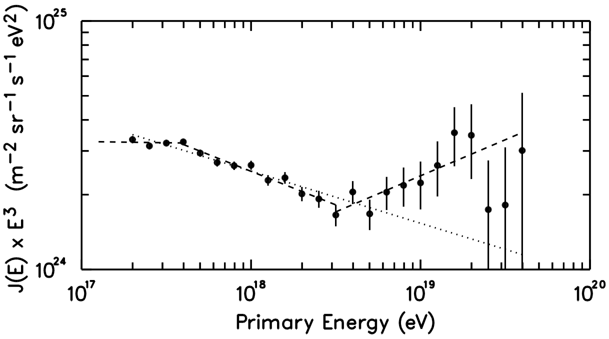

Figure 2.4. The Fly's Eye stereo spectrum.

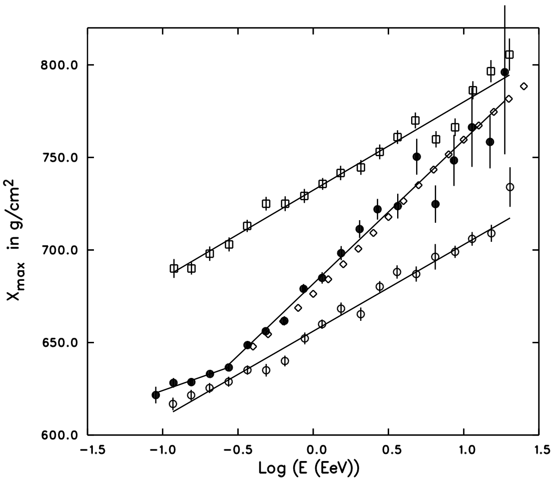

Figure 2.5. The Fly's Eye composition

The most recent measurement of the spectrum comes from the AGASA collaboration [13]. A most important feature of the AGASA spectrum is that it extends above 10^{20} eV. At the time of the publication, they had observed a total of six events above 10^{20} eV. AGASA's composition measurements are consistent with those of the Fly's Eye group [14].

2.3 The GZK cutoff

In the inter-galactic medium, a proton with sufficiently high energy ($> 6 \times 10^{19}$ eV) has a finite probability of colliding with a cosmic microwave background photon. In this collision the proton and photon combine in a delta resonance which then decays to a proton and a neutral pion (equation 2.1). The attenuation length for protons, due to this process, is on the order of 30 Mpc.

$$p + \gamma_{2.7K} \rightarrow \Delta^*(1232MeV) \rightarrow p + \pi^0 \tag{2.1}$$

The GZK cutoff in the energy spectrum is due to this interaction and should be observed if the CR are of extra-galactic origin. The nominal cutoff is at 6×10^{19} eV, assuming isotropic source distribution, however it is not expected to be a sharp cutoff. Instead the flux may be suppressed above the cutoff. Heavier nuclei photodisintegrate and turn out to have an even shorter attenuation length.

The above discussion assumes that cosmic rays can be accelerated to energies above the GZK cutoff in the first place. The acceleration of cosmic rays to energies greater than 10^{20} eV, however, poseses a serious challenge to theorists. The problem lies in the size and magnetic field strength requirements of the accelerating region. Figure 2.1, originally due to Hillas [15], shows possible sources of cosmic rays. Sources which lie above the lines marked 10^{20} eV proton (iron), are capable of accelerating protons (iron nuclei) to above 10^{20} eV. As can be seen from the figure, not many candidates exist. In considering candidate sources, one must also consider their distance from Earth, as the GZK effect becomes significant for distant sources.

An extension of the spectrum beyond $10^{20}eV$ is still possible. Some top-down CR production models use the fact that neutrinos can travel cosmological distances with very little attenuation, to get around the GZK cutoff. A possible scenario would be the production of UHE neutrinos from the decay of "X-particles", and the subsequent conversion of the neutrinos into UHE electrons in the Earth's atmosphere [16]. The observed events with energies above the GZK cutoff can be explained as the result of the electromagnetic cascades generated by these electrons. The hypothetical X-particles, supermassive gauge bosons and Higgs bosons, are produced by the collapse or annihilation of topological defects produced in the early universe [17].

CHAPTER 3

EAS PHYSICS

The collision of a high energy cosmic ray particle with an air nucleus initiates a cascade of relativistic particles in the atmosphere. The cascade contains a large number of particles (10^{11} charged particles at the shower maximum development for a 10^{20} eV primary) and has a lateral extent on the order of hundreds of meters to several kilometers, hence the name extensive air shower. The passage of the EAS particles through the atmosphere generates Čerenkov and scintillation (air fluorescence) light. In addition to ground arrays that sample the shower particles at a fixed elevation, detection of the Čerenkov or the air fluorescence light provide additional techniques for observing EAS.

Above 10^{15} eV, observation of EAS provides the only practical method for the observation of cosmic rays. The energy, particle type, and arrival direction of the CR are inferred from the measured properties of the shower. In practice, simple models of shower development involving a handful of parameters, are used to relate the observed shower properties to the energy and mass composition of the primary CR. These models are typicaly phenomenological parameterizations of more detailed and elaborate calculations which take into account the fundemental interactions and the details of transport through the atmosphere of the shower particles. Sophisticated models of EAS are usually implemented in Monte Carlo programs such as AIRES [18] and CORSICA [19]. A detailed discussion of the different models of EAS development is beyond the scope of this work, brief mention will be made, however, of some of the issues that may have an effect on the interpretation of the results of our measurement.

3.1 Shower Development

In terms of the type of secondary particles, an EAS is composed of three components: (a) A hadronic core, (b) an electromagnetic component and (c) a muonic component. The hadronic core feeds the electromagnetic component primarily through the decay of neutral pions and kaons, and the muonic component through the decay of charged pions and kaons. As the shower develops, the hadronic and electromagnetic components grow to a maximum size (number of particles), at which point, the average energy of the particles becomes insufficient for the production of more particles. Subsequently, the number of particles diminishes after that point. The number of muons also grows to a maximum but decreases very slowly because of their small ionization losses and their relatively long half-life.

Whether a shower particle interacts or decays depends on the type of particle and the types of interaction (strong, electromagnetic, weak) the particle participates in. An interaction length and a decay length can be defined for each particle and calculated based on elementary particle theory. A particle will typically interact or decay according to the competing process with the shortest characteristic length. Because the probability of interaction depends on the amount of matter the particle penetrates, interaction lengths are usually measured in g cm^{-2}. On the other hand, decay lengths depend on the particle's half-life and energy (Lorentz factor) and are therefore measured in meters. The atmospheric density follows an exponential profile with altitude, and so, the competition between the different interactions is also altitude dependent.

3.1.1 Hadronic Core

The dominant processes in the hadronic core are:

$$incident + target \longrightarrow pions + kaons + \ldots \tag{3.1}$$

In the case of the first interaction, the incident particle is the primary nucleon and, in subsequent collisions it can be any of the hadrons produced in previous interactions. In a typical collision, more than 2/3 of the particles produced are pions, followed by about 10% kaons. Other hadrons, including neutrons and protons, are also produced.

Two variables that are often used to characterize hadronic interactions are the *inelasticity* and *multiplicity* of the collision. The first is the fraction of the incident particle's energy, in the laboratory system, that is available for particle production. The second is the number of produced particles, of a given species, for an incident particle colliding with a target particle. Another important parameter is the collision cross section. The inelastic proton-air cross section is particularly important in determining the shape of the shower deveolpment.

The collision parameters described above can not be calculated from theory (QCD), instead accelerator measurements and phenomenological models based on the measurements and on theory are used to estimate their values. The models also allow for the extrapolation of these parameters to the UHE regime. The extrapolations are model dependent and can not be expected to be accurate when applied at energies several decades higher than the energies where the measurements were made. This fact is a major source of uncertinity in the interpretation of experimental extensive air shower data.

Extensive air showers generated by nuclei involve nucleus-nucleus interactions. These interactions can be treated in the framework of the superposition model. In this scenario, a shower generated by a nucleus with atomic number A and energy E is equivalent to the superposition of A proton showers, each with energy E/A. This approximation predicts the average behavior correctly, however, it underestimates the fluctuations in shower development. A more refined "fragmentation" model, which is based on analysis of low energy cosmic rays data, gives similar results for the average behavior, but results in larger fluctuations [20].

3.1.2 Electromagnetic Cascade

A third of the pions produced in the hadronic collisions are π^0's. These decay electromagnetically into two photons ($\pi^0 \longrightarrow \gamma + \gamma$). Neutral pions have a much shorter lifetime ($10^{-16}\,$s) than the $\pi^{\pm}$'s, and their decay is essentially instantaneous even with time dilation effect. Each photon produced by the π^0's decay initiates an electromagnetic cascade, the result of alternating pair production and Bremsstrahlung. In pair production, a photon in the field of a nucleus produces an electron-positron pair ($\gamma \longrightarrow e^- + e^+$), each of which then loses some of it's energy in the production of additional photons via Bremsstrahlung ($e^\pm \longrightarrow e^\pm + \gamma$).

The radiation length for electrons is defined by the exponential rate of energy loss by Bremsstrahlung, $-dE/dx = E/X_0$. In air, we have $X_0 = 36.5\,\mathrm{gm\,cm^{-2}}$. In a similar fashion, a radiation length can be defined for pair production, the value for which is approximately equal to that for Bremsstrahlung. In an electromagnetic cascade, the number of particles doubles, and the energy per particle is halved, over each interval of $X_0 \ln 2$. This multiplicative process continues as long as the photons have sufficient energy to pair produce and to insure that the above two processes dominate over other energy loss mechanisms. At lower energies, Compton scattering and to a lesser extent the photo-electric effect contribute more significantly to photon energy loss. For low energy electrons, ionization losses dominate.

3.1.3 Muonic Component

Muons are mainly produced via the decay of charged pions ($\pi^\pm \longrightarrow \mu^\pm + \nu$). Charged kaons decay can also produce muons, either directly, or by producing charged pions which in turn decay into muons.

Muons ionization losses are small and their decay times are long. Therefore, they survive to reach the ground. Although the number of electrons in the shower is much greater than the number of muons, the fact that muons are much more penetrating than electrons means that they can be selectively detected by underground detectors (e.g. scintillators buried underground or shielded by an absorber such as lead.)

The number of muons at ground level depends upon the energy and the mass composition of the incident CR. Mass composition measurements done by ground arrays are based on this dependence. Air fluorescence detectors, such as HiRes, can not measure the muon content of the EAS. Thus, muons are largely irrelevant to our measurement and will not be discussed further.

3.2 Shower Parameters

The fluorescence and Čerenkov light that HiRes observes are produced primarily by electrons. For the calculation of light yield, it is neccesary to know the number of electrons in the shower (the shower size) at different points along the shower trajectory. Hillas's analytical treatment of EM cascades leads to a simple parameteric formula which gives the number of electrons as function of a parameter known as the age (s) of the shower. This parameterization was adapted by Gaisser for CR initiated showers.

3.2.1 Longitudinal Profile

The Gaisser-Hillas formula gives the approximate number of electrons as a function of atmospheric depth along the shower axis:

$$N_e(x) = N_{max} \times \left(\frac{x - x_0}{x_{max - x_0}} \right)^{(x_{max} - x_0)/\lambda} \exp\left(\frac{x_{max} - x}{\lambda} \right) \tag{3.2}$$

where x is the atmospheric slant depth along the shower track, x_0 the depth of the point of first interaction, x_{max} the depth of shower maximum (i.e. where $N = N_{max}$), and λ a scale constant with a value of $70\,\mathrm{gm\,cm^{-2}}$. The shower age is given by $s = 3/(1 + 2x_{max}/x)$, with both x and x_{max} measured from the point of first interaction. The first interaction point is the location of the initial collision of the CR particle with the atmosphere. The value of x_0 depends on the collision cross section, and hence the energy and mass composition of the particle. In the UHE regime, the initial collision typically occurs within the first $100\,\mathrm{gm\,cm^{-2}}$. The depth of shower maximum, x_{max}, depends on the position of x_0, the shower energy, and composition. The *elongation rate, $dx_{max}/d\ln(E)$,* relates the depth of maximum of an average shower to the shower's energy [21]. For a given shower type, i.e. proton or iron, the depth of shower maximum increases linearily with the logarithem of the energy, which implies a constant elongation rate. Figure 2.5 shows the results of the Fly's Eye composition measuremnt, The figure shows the measured x_{max} vs. energy ditribution along with Monte Carlo predictions for pure proton and pure iron distribution. It can be seen from the figure that, typical values for x_{max} fall in the range $600 - 800\,\mathrm{gm\,cm^{-2}}$, for showers with energies in the UHE regime.

3.2.2 Electron Lateral Distribution

EAS are intrinsically three dimensional, that is to say, they have a measureable lateral width. For HiRes, shower reconstruction requires that the lateral width be included in the modeling of the showers. This is especially true for close by showers.

The lateral distribution of electrons (particle density) is given approximately by the Nishimura-Kamata-Greisen (NKG) formula [22]:

$$\rho(r) = \frac{N}{r^2} f\left(s, \frac{r}{r_M}\right) \tag{3.3}$$

where N is the total number of electrons, s is the shower age, r_M is the Moliere radius for multiple scattering, and f is the Nishimura-Kamata function:

$$f\left(s, \frac{r}{r_M}\right) = \left(\frac{r}{r_M}\right)^{s-2} \left(1 + \frac{r}{r_M}\right)^{s-4.5} \frac{\Gamma(4.5 - s)}{2\pi\Gamma(s)\Gamma(4.5 - 2s)} \tag{3.4}$$

3.3 Light Production

The ultra-relativistic particles in the shower produce Čerenkov light, because in most sases, their speed exceeds that of light in air. The Čerenkov radiation is beamed forward along the shower axis and accumaletes along the shower trajectory, leading to a very intense light beam within a few degrees of the shower axis. The amount of Čerenkov light produced and the angular distribution of the light pulse depend on the number and lateral distribution of electrons in the shower as well as the energy distribution of electrons. For the analysis of HiRes data, we use parameteric formulae based on previous measurements and Monte Carlo simulations to describe the Čerenkov light. These will be described in detail in section 6.2.

Air fluorescence is another light production mechanism. Electrons in the EAS excite the Nitrogen molecules in the atmosphere. The Nitrogen molecules then relax by emitting fluorescence light isotropically. Most of the emitted light is in the Ultraviolet region with wavelengths in the range $300 - 400\,\mathrm{nm}$. The emission

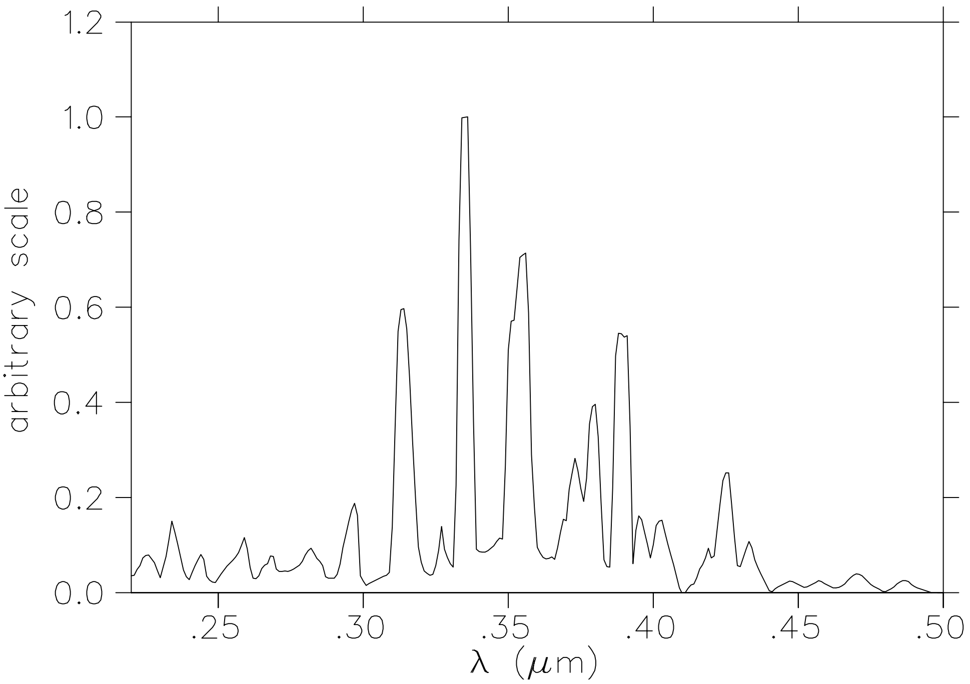

Figure 3.1. Nitrogen fluorescence spectrum.

spectrum is shown in figure 3.1 [23]. Again, the details of the calculations used in the data analysis will be described in section 6.2.

When a shower is observed from the side, the light signal received from the shower is dominated by fluorescence light. This is important for the energy determination of observed showers because, as discussed in section 6.1, the energy is estimated based on the integral of the shower size along the shower trajectory. The shower size is, in turn, inferred from the amount of collected fluorescence light (equation 6.13), after correcting for direct and scattered Čerenkov light.

CHAPTER 4

THE HIRES DETECTOR

The High Resolution Fly's Eye (HiRes) detector consists of two sites that can operate independently or as one "stereo" detector. The two sites are located at Little-Granite mountain (HiRes-I), and Camel's Back Ridge (HiRes-II) at the U.S. Army Dugway proving grounds in Utah. While the two sites are operated independently, the data collected can be analyzed either in monocular mode for each site, or together in stereo mode. This disseertation will report on the first results from the monocular observation made by HiRes-I. The HiRes-I site will therefore be the main focus of this chapter.

4.1 Overview

The High Resolution Fly's Eye (HiRes) detector is the successor of the University of Utah's Fly's Eye detector that was operated from 1981 to 1992. HiRes employs larger mirrors, smaller photo-multiplier tubes, and improved electronics over the original Fly's Eye. As part of the R&D effort for HiRes, a prototype detector with 14 mirrors (HiRes-I prototype) that used the new optics and a new sample and hold (S/H) electronics system was operated from 1994-1996 at Little-Granite Mountain. At the same time, development work on a FADC electronics system was carried out. The prototype detector operated in conjunction with a four mirror prototype at Camel's Back (HiRes-II prototype) and with the CASA-MIA detectors at the original Fly's Eye II site.

In September 1996, a study performed by the members of the HiRes collaboration indicated that a re-deployment of the prototype detector mirrors coupled with the addition of eight more mirrors (four HiRes II mirrors and four to be manufactured) could be used to construct a detector to study the high end of the

Table 4.1. BigH mirrors: Mirrors are numbered from 1 to 22. The table also identifies where the electronics rack and PMT cluster for each mirror came from, PMT manufacturer, and the electronics revision.

BigH Mirror	Start Date	Old Rack Number	Old Cluster Number	PMT Manufacturer	Electronics Revision
1	May 97	1	8	EMI	3
2	May 97	10	3	Philips	3
3	May 97	4	4	EMI	3
4	May 97	2	2	EMI	3
5	May 97	9	10	Philips	3
6	May 97	7	6	EMI	3
7	May 97	8	12	Philips	3
8	May 97	6	1	Philips	3
9	May 97	5	13	EMI	3
10	May 97	12	11	Philips	3
11	May 97	13	7	EMI	3
12	May 97	3	14	Philips	3
13	May 97	14	9	Philips	3
14	May 97	11	5	Philips	3
15	June 97	3@HR2	3@HR2	Philips	4
16	June 97	2@HR2	2@HR2	Philips	4
17	April 98	New	New	Philips	3R&4C
18	-	4@HR2	4@HR2	Philips	4
19	April 98	New	New	Philips	4
20	June 97	1@HR2	1@HR2	Philips	4
21	March 98	New	New	Philips	4
22	March 98	New	New	Philips	4

energy spectrum. To obtain the largest possible aperture at 10^{20} eV, the mirrors are configured in a “ring” that covers the full azimuthal range. The mirrors have an elevation angle coverage of $3° - 17°$. This strategy of redeployment also has the benefit of ensuring maximum stereo coverage at the earliest possible time frame as the HiRes-I detector comes on-line in 1999. In addition to reconfiguring the prototype mirrors, some minor hardware modifications were required to improve detection of EAS at large distances ($\sim 30\,km$), these are given on page 35.

In the early months of 1997 we began the process of moving the prototype

Figure 4.1. A schematic representation of the HiRes-I detector components.

mirrors to their new positions and, in May of the same year, test operation of the new detector began with 14 mirrors. Additional mirrors were added to the detector as they became available. Table 4.1 summarizes the redeployment of the prototype mirrors. The date of installation and start of operation is shown for each mirror, along with the origin (in the prototype detectors) of its PMT cluster and electronics rack. Note that the HiRes detector units employ two types of PMTs and that the S/H electronics used come in two revisions. It can be seen from the table that mirror 18 is missing, this mirror will be added to the detector at a later date.

4.2 The HiRes-I (BigH) Detector

Within the HiRes collaboration, the redeployed HiRes-I detector is usually refered to as BigH, to distinguish it from the HiRes-I prototype. BigH currently operates 21 detector units (mirrors), connected via Ethernet to a main data acquisition computer. The mirrors are also connected to a GPS based Central-Timing (CT) crate through dedicated timing cables. Each detector unit consists of a spherical mirror, a cluster of photo-multiplier tubes, and associated electronics. For nightly calibration of the detector, light from a YAG laser is guided through optical fibers to the detector units. Figure 4.1 shows a schematic representation of the detector illustrating the different components and their interconnections.

The layout of the HiRes-I site is shown in figure 4.2. The mirrors are housed in twelve shelters surrounding a central facility where the Data Acquisition (DAQ) computer and the CT crate are located. Five of the shelters shown in figure 4.2 are buildings which previously housed prototype mirrors (including one corn silo), and were designed to point towards the CASA-MIA site. This fact accounts for the odd positioning of the detector units within the buildings. seven new shelters, housing the 14 original HiRes-I prototype mirrors were built for this stage of the experiment. Over the site, the mirrors are oriented such that they form a ring covering the full

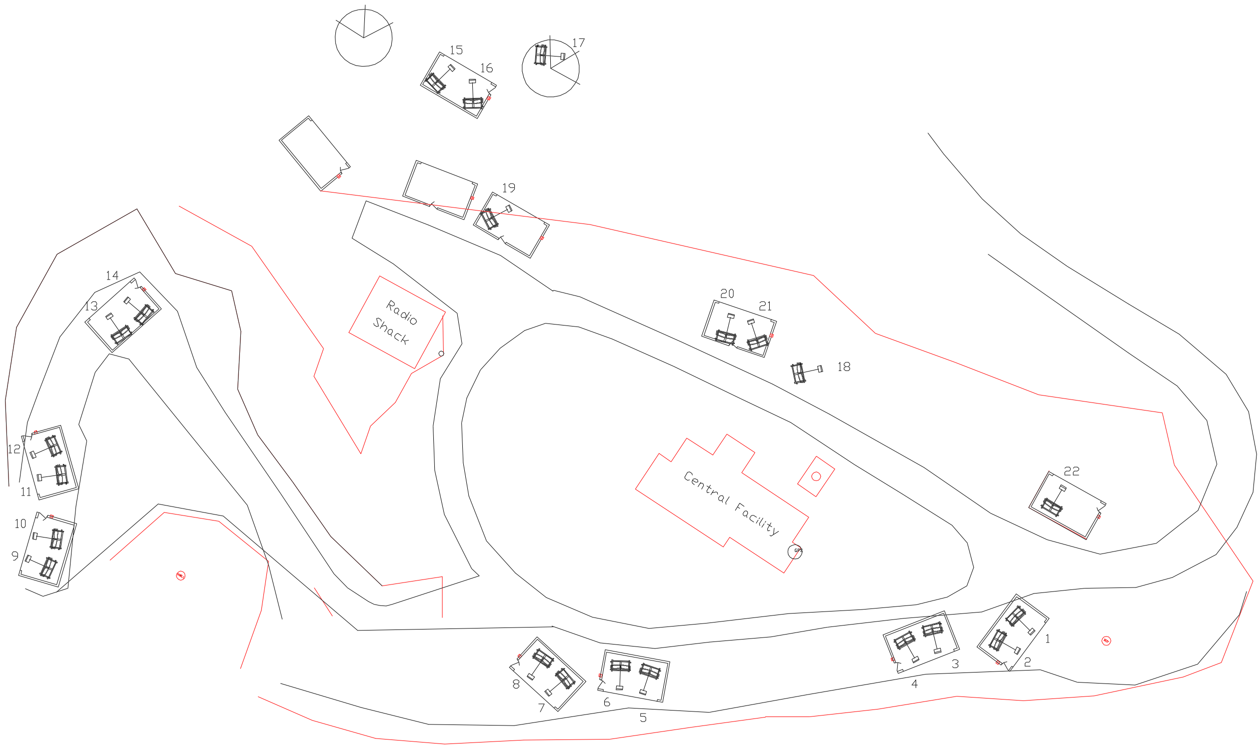

Figure 4.2. The physical layout of the HiRes-I detector.

azimuthal range, with each mirror axis pointing at an elevation angle of about 10°. The vertical coverage of the mirrors extends between 3°-17° in elevation. Figure 4.3 shows an event display used at HiRes-I, with the mirror numbers indicated. The outer edge represents 3° above the horizon, while the center of the display is the zenith.

The central DAQ computer at HiRes-I was originally a DEC Alpha-station 200.

It was replaced with a generic Pentium-II PC running Linux in late 1998.

Five of mirror buildings are buildings that were used by the prototype, including one corn crib. This accounts for the odd positioning of the detector units within the buildings. Seven of the buildings, housing the first 14 detector units, were built for this stage of the experiment. Inside the buildings, the mirrors are oriented such that they form a ring that covers the full azimuthal range, with the mirror axis pointing at an elevation angle of about 10°, figure 4.3 shows an event display (no events are shown) of the BigH detector. On the display, the outer edge represents 3° above the horizon, while the center of the display is the zenith. The main DAQ computer is a pentium PC running Linux.

4.3 Detector Unit

As already mentioned, BigH uses “recycled” detector components from the HiRes-I and HiRes-II prototype detectors. The additional units were built according to the same specifications as the HiRes-II prototype mirrors. Kidd [24] provides a detailed description of the HiRes-I prototype detector components and operation. Wilkinson [25] describes both prototype detectors and gives a very detailed account of the timing system hardware and operation. The description below is intended to complement those given in the above references and will highlight the hardware and software modifications made.

4.3.1 Mirror

HiRes uses spherical mirrors assembled from four glass segments. The total area of a mirror is $4.18\,\mathrm{m}^2$. Obscuration of the mirror by the PMT cluster results in an effective mirror area of $3.72\,\mathrm{m}^2$. The mirror reflectivity has a mild wavelength dependence as shown in figure 4.4. The reflectivity levels shown in this figure were measured from a “clean” mirror. In the field, dust collecting on the mirrors reduces the reflectivity by about 10%. An operational value of 0.8, representative of the actual reflectivity in the field over the wavelength band of 300 - 400 nm, is assumed in this analysis.

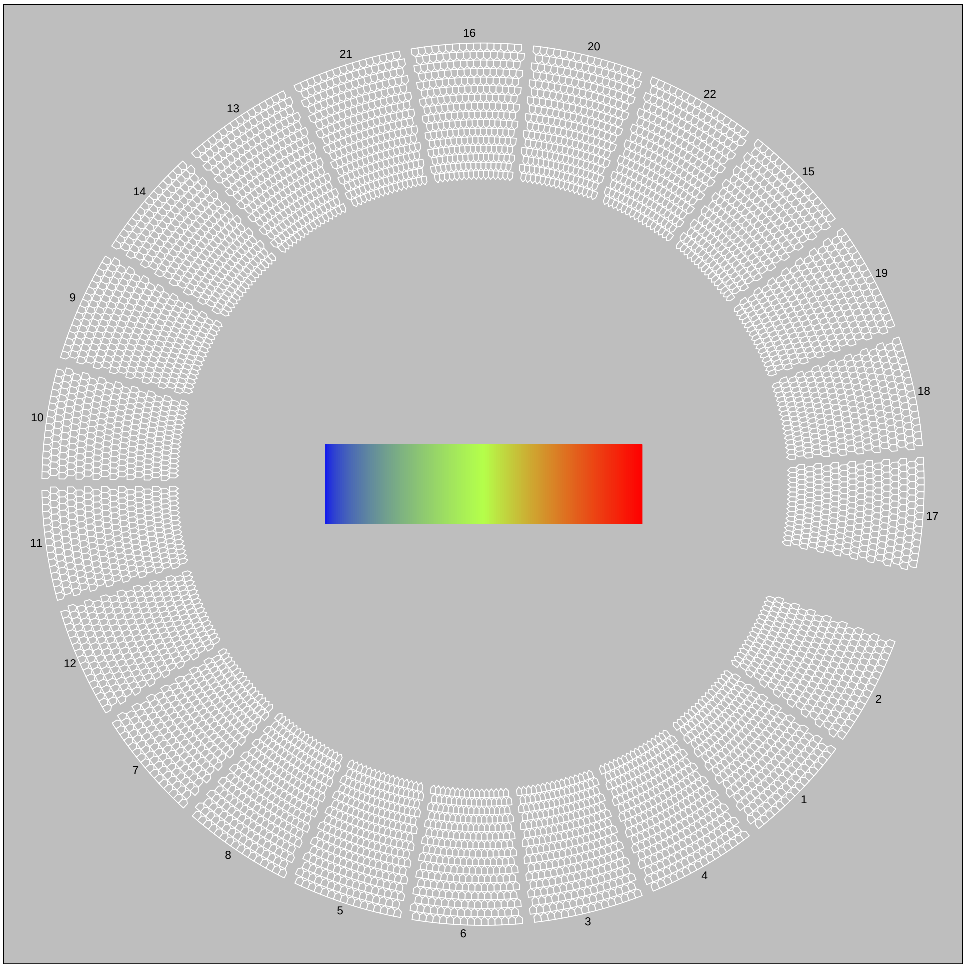

Figure 4.3. HiRes-I event display. Mirror numbers are indicated next to each mirror. The outer edge represents 3° above the horizon, while the center of the display is the zenith.

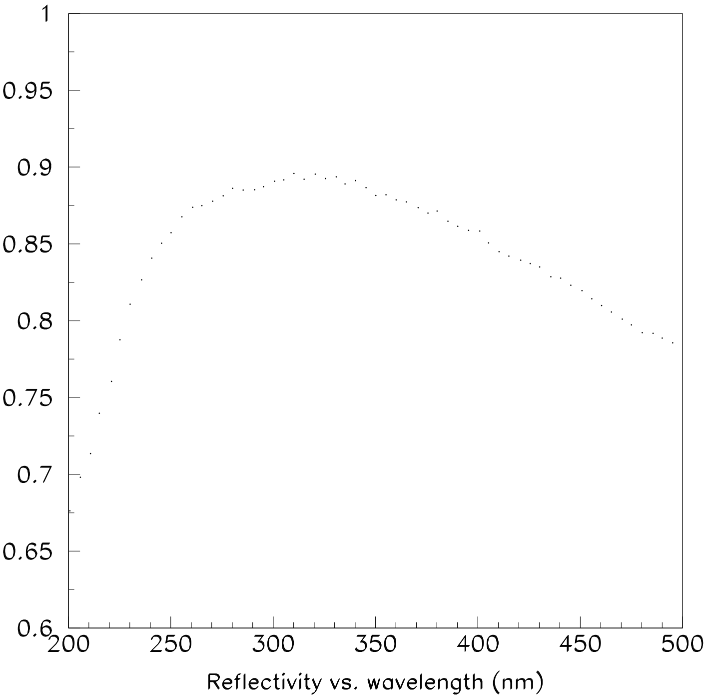

Figure 4.4. Measured wavelength dependence of mirror reflectivity.

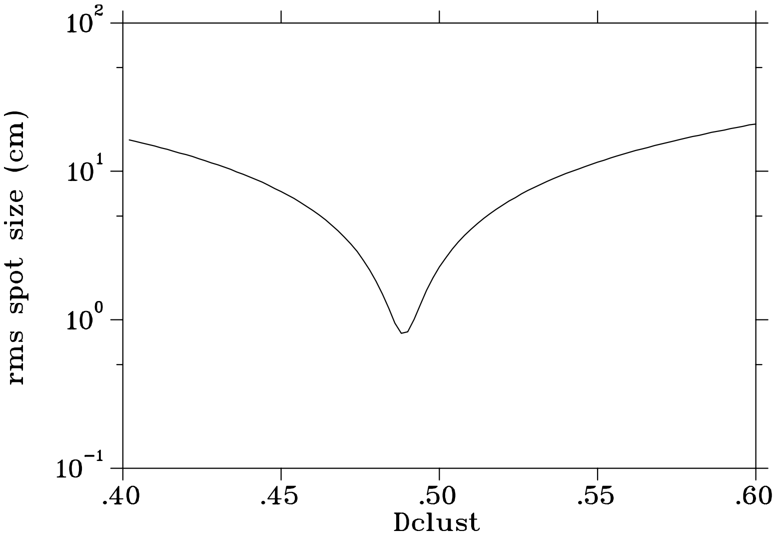

Figure 4.5. Mirror spot size (on-axis) vs. cluster distance. Distance is expressed as a fraction of the mirror radius of curvature.

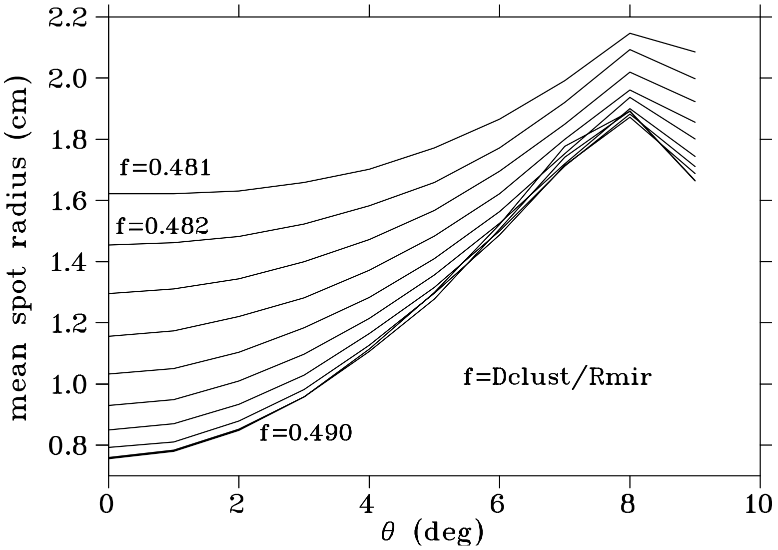

Figure 4.6. Mirror spot size vs. off-axis angle for a set of trial mirror-cluster separations.

4.3.2 PMT Cluster

The exact mirror-cluster separation was chosen to minimize the spot size with the constraint of achieving a uniform spot size across the face of the cluster. Figure

4.5 shows the optimal mirror-cluster separation (as a fraction of the mirror radius) for a source on the mirror axis. Figure 4.6 shows the variation of the spot size across the face of the cluster. An optimal mirror-cluster separation of 0.485 times the mirror radius was chosen.

The PMT cluster consists of 256 hexagonal PMTs assembled in a honeycomb geometry of 16 rows of 16 tubes. Two types of tubes are used, Phillips XP3062/FL and EMI 9974KAFL. Table 4.1 indicates the type of tubes used by each mirror. Both types have a diameter of 40mm and similar quantum efficiencies. Small differences in response do exist, however, and these are accounted for in the calibration. The size and position of the tubes in front of the mirror give an angular coverage for each tube of approximately $1° \times 1°$. For the whole cluster the angular coverage is $16° \times 14°$. High voltage dividers and preamplifiers are directly mounted onto the PMTs which then plug into a backplane. High and low voltage power are brought into the PMTs on the backplane. Signals are also routed out to ribbon cable connectors on the backplane. To improve the signal to noise ratio, light coming into the PMT cluster first passes through a UV filter glass [26]. The transmittance of the UV filter is shown in figure 4.7.

4.3.3 Mirror Electronics

The electronics rack houses the low-and-high-voltage power supplies for the detector unit. It also contains a double-height VME crate which houses the readout electronics. Each crate holds (a) a CPU board powered by a Motorola 68030 processor, (b) a Programmable Pulse Generator (PPG) card, (c) a trigger logic board, (d) a multi-function “garbage” board and, (e) sixteen readout boards. The readout boards serve a similar function to the ommatidial nerves in the eye of a fly, and we typically refer to them as ommatidial boards (OMBs). The ommatidial boards provide secondary amplification, integration, and digitization to the PMT signals. They also send trigger information to the mirror CPU board which handles communications with the DAQ and the CT crate. The garbage board handles miscellaneous functions such as remote control of the garage door, temperature

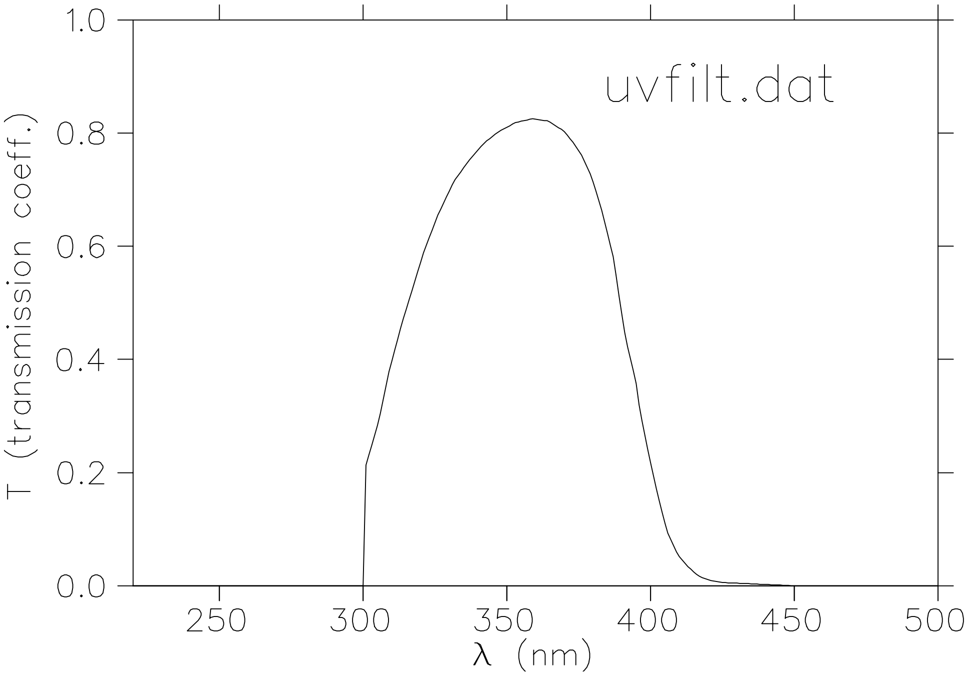

Figure 4.7. Transmission coefficient for the HiRes UV filter.

monitoring, and other diagnostics reporting tasks.

As stated previously, two variations on the basic S/H system are in use for BigH mirrors. Rev. 3 mirrors were employed by the HiRes-I prototype at Five Mile Hill. The four HiRes-II mirrors and the additional mirrors manufactured for BigH use a later revision of the electronics system (Rev. 4). Both revisions have the same basic structure, but there are some differences between the two. Figure 4.9 shows block diagrams for both the Rev. 3 (top) and Rev. 4 (bottom) ommatidial boards.

In both revisions, the PMT signal is split into two and driven through two readout channels denoted Channel A and Channel B. For each channel the signal is further split into two lines, one passing through a filter and into a comparator, and the other propagating through a delay line and into integration circuitry. The tube thresholds are adjusted automatically to maintain a pre-selected tube trigger rate.

The main differences between the two electronics revisions are:

- Rev 3: only one of Channel A or Channel B is allowed to trigger. The choice

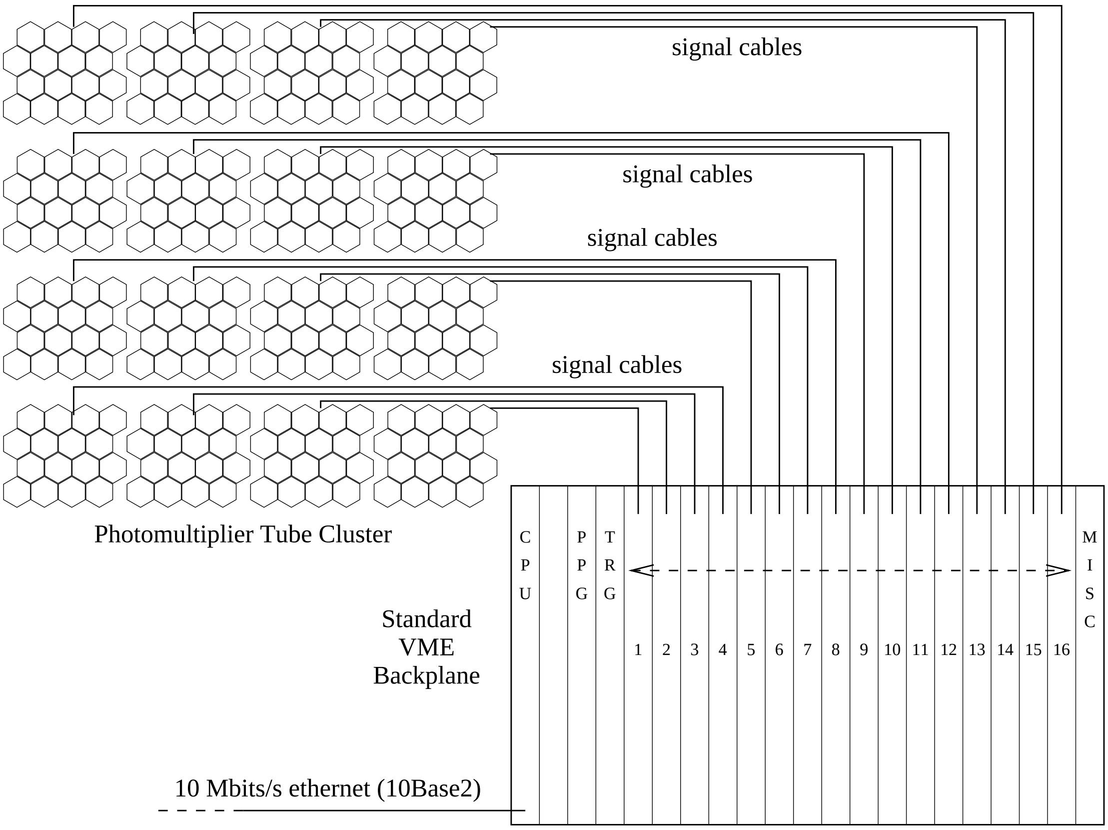

Figure 4.8. Mirror electronics crate components

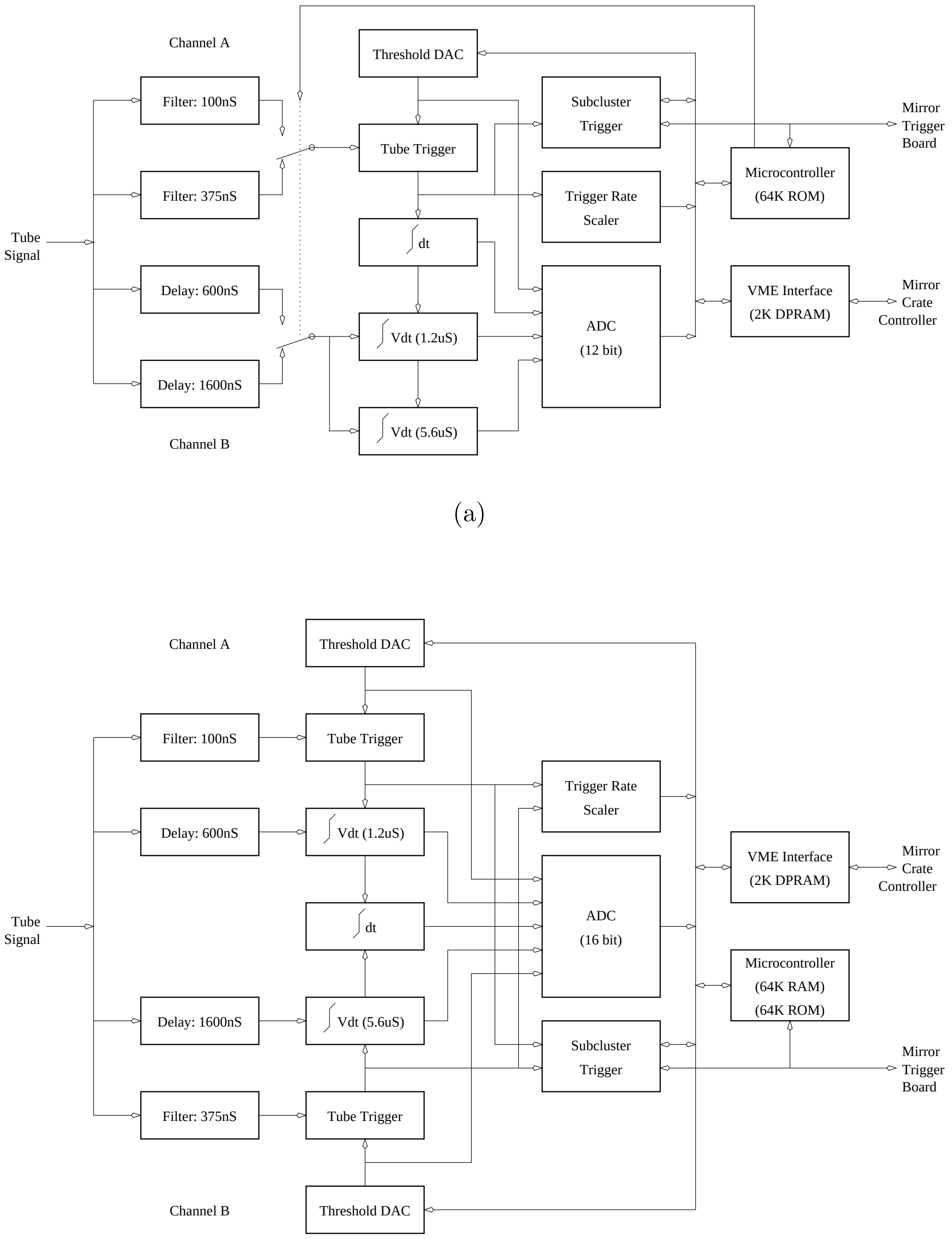

(a)

(b)

Figure 4.9. Ommatidial board block diagram for Rev. 3 (top) and Rev. 4 (bottom) mirrors.

of channel also sets the delay line to be used.

- Rev 4: either channel can trigger and each channel uses it's own delay line.
- Rev 4: thresholds are set independently for channels A and B.
- Rev 4 uses a 16 bit ADC, while Rev. 3 uses a 12 bit converter.

The following modifications were made to the prototype mirrors before they were moved to their BigH positions:

1. The HiRes-I prototype used Rev. 3 mirrors with channel A selected. For BigH, these mirrors were set to use channel B. This meant using the 1600 ns delay line which rendered the $1.2\,\mu$s integrate gate useless. The $5.6\,\mu$s integration gate is now used.
2. The mirror hold-off time was increased from $10\,\mu$s to $50\,\mu$s. This modification had to be done in hardware by replacing a resistor on the Ommatidial board.
3. Mirror-cluster distance set to 0.485 times the mirror radius of curvature, to achieve a more uniform spot size across the cluster surface.

4.4 Central Timing

The subject of central timing for the HiRes detector is covered in great detail by Wilkinson [25]. A GPS based central timing unit is used to record the absolute time of HiRes-I events. A mirror trigger initiates a save condition for all triggered tube QDCs and it also starts the TDC integrators for all triggered tubes. The charge and time information is saved and other tubes are allowed to trigger for a constant time interval (hold-off time) after the mirror trigger. At mirror hold-off, the tube TDCs are stopped and a signal is sent from the mirror to the CT crate to latch the 40 MHz scaler signal. The mirror then sends a packet with the triggered tubes signal and timing information to the central DAQ which in turn stores the event for off-line processing.

4.5 YAG Laser

The YAG laser is used for nightly calibration of the photo-multiplier tubes response. Optical fiber bundles drive the laser output to the mirror buildings and either illuminate the cluster face directly or illuminate the mirror which then reflects the light back onto the PMT cluster. The optical fibers were installed in 1998 and YAG calibration data taking started in 1999. Cosmic Rays data analyzed in this thesis did not have the YAG calibration applied to it.

CHAPTER 5

DETECTOR CALIBRATION

When a HiRes mirror is triggered, pulse area and time of trigger is recorded for each PMT participating in in the formation of the trigger. The pulse area is digitized from a charge integrator, a charge-to-digital convertor (QDC), and the time between the PMT signal and the delayed mirror trigger is recorded using a time-to-digital converter (TDC) running in common-stop mode. The number of photons collected by a PMT is obtained from the tube QDCs by applying a calibration procedure that accounts for the PMT and electronic gains. Corrections must also be made for the mirror reflectivity, the UV filter transmission, the tube quantum efficiency (QE), and the profile of the tube response across the face of each PMT.

Atmospheric calibration is considered to be part of the detector calibration, since the atmosphere is used as the shower medium. To derive the luminosity of the EAS from the measured light flux at the detector requires corrections for atmospheric attenuation of the light. The attenuation changes with time corresponding to the changing density and profile of aerosols in the atmosphere.

To calibrate the HiRes detector, the following systems are used: (a) PMT absolute gain and QE calibration facility, (b) "roving Xenon flasher" (RXF) devices and, (c) a YAG laser system. Atmospheric monitoring systems include the "inter-site flasher", a set of radio controlled vertical flashers, and a steerable Laser at HiRes-II. The PMT absolute gain calibration facility is located at the University of Utah, all the other systems are used in the field during data taking.

At the time of writing all calibration systems are in place and calibration data is collected regularly. However, some calibration data is not available for a significant fraction of the data set, as the calibration systems were in the process of being deployed after initial data taking had started. Moreover, analysis and application of the calibration data is still under development for some of those systems. In particular the atmospheric data from the steerable laser has not yet been integrated into the analysis yet.

This chapter describes the detector calibration. Emphasis will be placed on procedures employed for this analysis rather than on general HiRes calibration or procedures to be implemented in the future. Special attention is given to the RXF calibration, which was used for calibrating the BigH data used in the spectrum measurement.

5.1 PMT Calibration

5.1.1 PMT Testing Facility

A photo-tube calibration facility is used to measure the absolute gain, quantum efficiency, and spatial profile of all tubes used in the HiRes detector. The apparatus and calibration procedure are described elsewhere [27] and will not be discussed here. Instead a list of the measured tube properties is as follows.

1. Gain as a function of applied voltage: The PMT gain is related to the applied high-voltage by $G \propto e^{\alpha} V^{\beta}$. The constants α and β are measured at seven points across the PMT face.

2. Quantum efficiencies at 325 nm, 351 nm, and 364 nm can be measured by the test facility. In practice, however, the manufacturer supplied QE at 337 nm is used.

3. PMT profile: Tubes are scanned to measure the PMT active area, with a 1 mm diameter spot, as a function of the light point of incidence.

The results of the QE measurements were found to be consistent with the specifications supplied by the manufacturer [27]. Furthermore, there is very little variation in QE among tubes [24].

The measurement of the variation of the tubes gain with voltage in the tube testing facility is used to keep or reject tubes. PMTs with too small an active area or have a 20% or more non-uniformity across the active area are rejected. Tubes must also have a minimum sensitivity or gain at a set voltage. The measurement is also useful in identifying groups of tubes with similar gain-voltage curves. Once sorted, matching sets of tubes are placed together in the same PMT cluster. This practice makes it easier to equalize the tube gains within each mirror. It should be noted that, the information from the tube scans does not, however, provide the detector calibration. It merely provides initial information about the incoming PMTs.

5.1.2 Initial Gain Setting

Before the re-deployment of the prototype mirrors to form BigH, the tubes absolute sensitivities were measured using a well calibrated set of standard tubes [28][29]. In the prototype, the goal had been to set all mirrors to a sensitivity of 15000 A/W. When the mirrors were measured, the mean sensitivity was 12093 A/W with a sigma of 1478 A/W. The mirror #3 in the prototype was the last to be moved and it had a sensitivity of 12070 A/W. This mirror and the roving Xenon flasher were used to set the sensitivities of the mirrors in their BigH configuration to a sensitivity of 15000 A/W. The QDCs of mirror #3 were scaled by 15000 / 12070. It was determined that for a Rev. 3 mirror, the QDCs should be set to 1492 to achieve a sensitivity of 15000 A/W. For the Rev. 4 mirrors, added in the following months, a value for the 15 bit channel B QDCs equivalent to the Rev. 3 standard value was calculated. The mirror gains were then set to that standard. This procedure assumes that the roving flasher was stable over the period when the mirrors were added. Experience with the roving flasher shows that it is stable over long periods of time.

5.2 Roving Flasher Calibration

The Roving Xenon Flasher (RXF) is a versatile calibration and diagnostics tool. It is housed in a portable mount that fits in a holder at the center of the HiRes mirrors. Using diffusers, the flasher provides a uniform light pulse over the entire cluster. The Xenon flash bulbs have been observed to be extremely stable over long periods of time. The use of the RXF in combination with neutral density filters makes possible the measurement of the PMTs response to light pulses with different intensities: A set of RXF shots is made with each of the different neutral density filters in front of the RXF, and the response of the tubes (QDC counts) is recorded. The calibration data thus collected is fit to a straight line (QDC vs. number of photons). The "gain" is obtained as the slope of the fitted line, where we assume that the number of photons hitting the tube is known for each filter setting. Alternatively the gain can be obtained based on photo-electron statistics, where the RMS variation in the gain for a given set of shots can be used to measure the mean gain for the set.

For the analysis presented in this thesis, BigH data calibration is based on one set of RXF data that was taken in May of 1998. This is referred to below as "Calibration-0". Many more sets of RXF data were taken since then, and a development effort is underway to improve on the calibration-0. The new calibration procedure is still undergoing testing and verification studies, so it has not been applied to the data. Below is a description of both procedures.

5.2.1 Calibration-0

An initial, "quick" calibration effort was made to jump start the analysis of BigH data.

The RXF device was used extensively for a period of over two years during the operation of the HiRes prototype detectors. Based on this experience, it was assumed that the RXF light output provides 12000 photons/tube when placed in the standard holder at the center of the mirror, i.e. the configuration used for the calibration procedure. For BigH calibration (calibration-0), neutral density filters with attenuation factors of 21%, 41%, and 64% were used. Four sets of 200 RXF shots were taken for each mirror, one with no external filter, and three with the above filters. The QDCs were recorded for each shot for each PMT. The mean response was compared to the filter transmission and the assumed 12000 photons/tube at 100% transmission.

For each set, the average and standard deviation of each tube's QDCs were

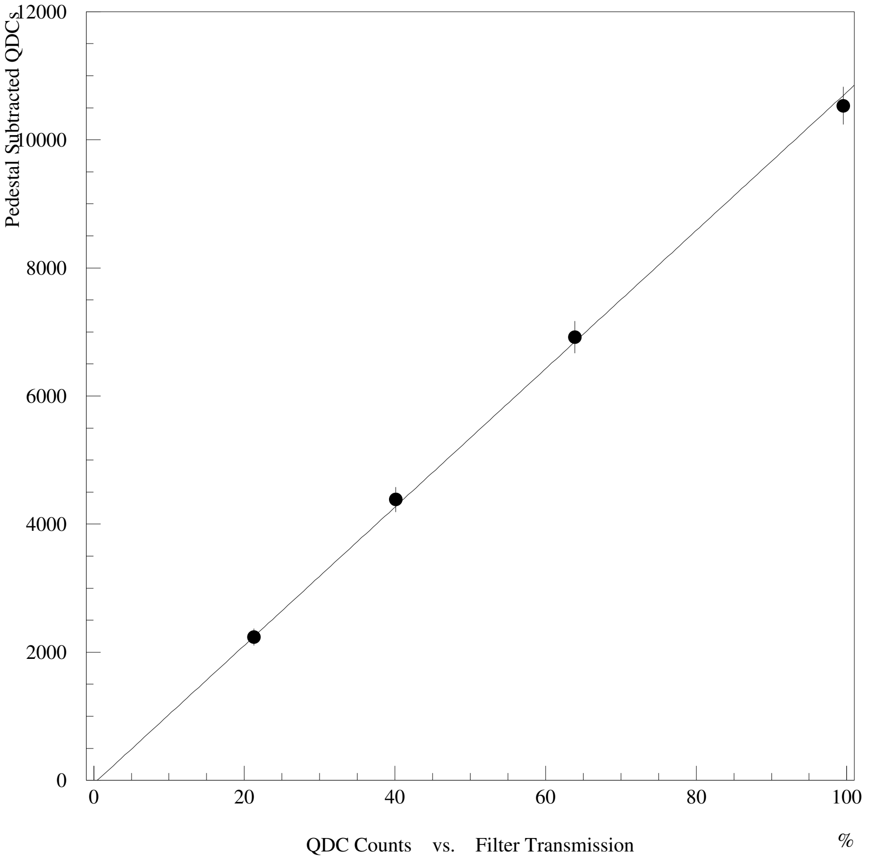

Figure 5.1. Tube QDC counts (Pedestal subtracted) vs. filter transmission. The slope of the line fit gives the tube gain.

recorded. The shots averaged measured response for each tube vs. the expected number of photos (12000 × 1.0, 0.64, 0.41, 0.21) forms one calibration data point. The data points were fit with a straight line to calculate the tube gain and pedastel. Figure 5.1 shows an example of such a plot for a Rev. 4 PMT..

The points are fitted to a line and the gain is obtained from the fit via $G = 1/slope \times 12,000\,[photons/QDCcount]$

This calibration suffers from several problems:

- Only one data set was taken and used to calibrate all data taken over a two year period. It is natural to expect that tube gains will change slightly over this period.

- Mirrors that were not installed at the time the calibration data was taken, were not calibrated. Data from these mirrors was not used in the analysis.

- The output of the RXF, here assumed to be 12000 photons/tube , is known to be correct to within ±30%.

- The response of the tubes is assumed to be linear. It is known that non-linearities exist at the low and high end of the QDC range, but these are assumed small (<10%).

5.2.2 Calibration-1

There is currently a concerted effort to implement a more thorough and accurate calibration procedure, referred to as calibration-1. This effort is "work in progress" and unfortunately the results are not yet ready to be applied to the EAS data analysis described in this thesis. The main advantage of the new procedure is that it uses Poisson statistics to relate the tube gain to the measured QDCs independently from an assumed RXF photon count. In addition, non-linearities are treated using data taken with the PPG at different pulse widths and heights. The difference in the tube QE between EMI and Phillips tubes is taken into account as are the variation in the UV filter transmission between mirrors. Finally, at least nine different sets of RXF data were taken over a period of a year to monitor gain variations with time. These data sets continue to be collected about once per month.

Photoelectron statistics can be used to relate the PMT signal variance to the mean signal from a number of exposures. It can be shown [27] that the following relation holds:

$$\mu_{pe} = 1.2 \times \mu^2_{QDC} / \sigma^2_{QDC} \tag{5.1}$$

Calibration-1 uses RXF data taken with the neutral density filters in the same was as the old calibration. For each set of RXF shots, the mean and variance of the tube QDCs are calculated. The mean number of photoelectrons follows from

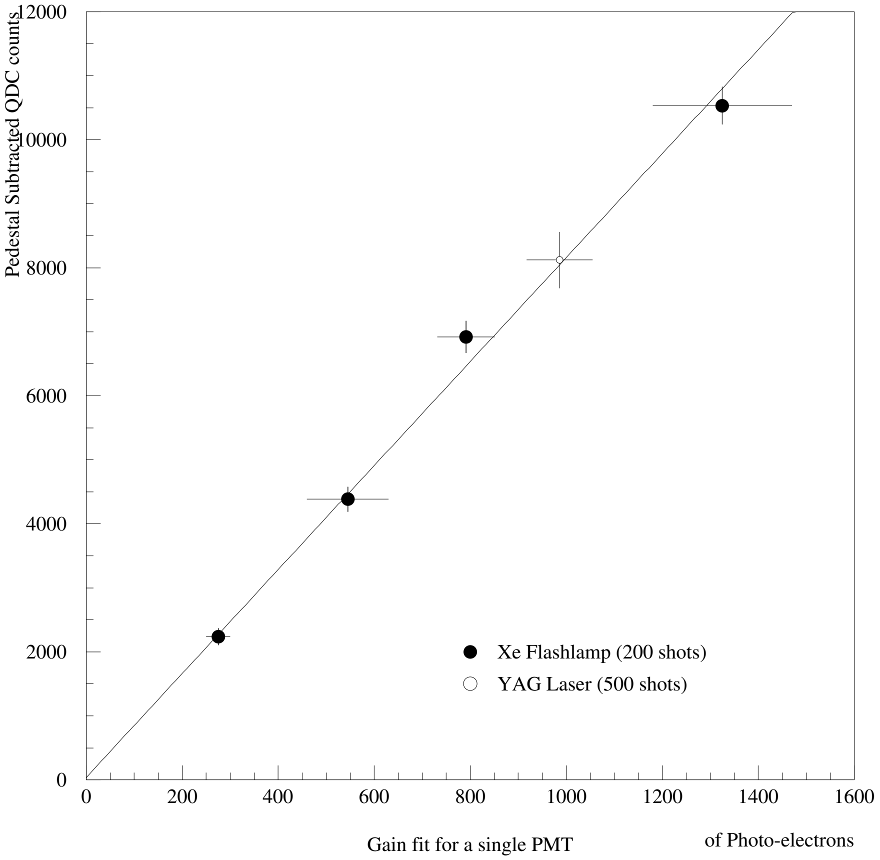

Figure 5.2. QDC vs. number of photoelectrons for one tube.

equation 5.1. A linear fit is then made for the number of QDC counts versus number of photoelectrons, and the tube gain is obtained from the slope of the line, as illustrated in figure 5.2. It should be noted that, in the figure, calibration data taken using the YAG laser is consistent with the RXF calibration, even though the YAG measurement was made using a different source at a different wavelength than the RXF measurements.

5.3 YAG Laser and Stability

A nightly calibration check of the BigH detector is done using a YAG laser. The laser delivers light to each mirror unit through optical fibers. Teflon diffusers are placed in front of the optical fibers to produce a uniform light distribution over the face of the PMT cluster. One set of fibers illuminates the cluster directly and another two sets illuminate the mirror which reflects the light back to the cluster. This way, the mirror reflectivity is also measured on a nightly basis.

The YAG system is in place and has been taking data since June 1998. The YAG data provides a means to track day to day variations in the PMT gains. Preliminary studies indicate that the nightly correction is on the order of 3%. Nightly calibration using the YAG laser data has not been incorporated in this analysis.

5.4 PPG and Electronics Calibration

The programmable pulse generator (PPG) is used both as a diagnostic tool, and for electronics calibration. As a diagnostic tool, pulses are sent from the PPG directly to the PMT pre-amplifiers, and dead channels are spotted by their lack of response in the event-display. As a calibration system, the PPG generates pulses of varying widths and amplitudes, under computer control. This information is collected nightly to provide an independent calibration of the amplification and integration circuitry. The non-linearities in the preamplifiers are calibrated by this procedure as well.

5.5 Atmospheric Calibration

The light attenuation due to Rayleigh scattering is essentially constant. Depending on atmospheric pressure and density profiles, variations from the mean are within ($\sim 3\%$) and can be ignored. The amount of aerosols, however, changes drastically with time and location, and is a major source of uncertainty in the energy assignment for distant showers. The Fly's Eye group and others have shown that, on average, the atmosphere at Dugway Utah is slightly better (less aerosols) than the 1976 US standard desert atmosphere. The aerosol model used for the analysis is based on the 1976 US standard atmosphere, and is described in section 6.3.2. Variations about this average can be quite significant as already mentioned, and continuous monitoring of the atmosphere during detector operation is necessary.

Currently, the HiRes detector relies on a set of vertical Xenon flashers [30][31], and a steerable YAG laser system [32] for atmospheric monitoring. The laser fires a set of shots every hour at different azimuthal and elevation angles, exploring the region around the two detectors. The light scatters back to the BigH detector from points along the beam that span a large fraction of the atmospheric volume observed by the detector. Unfortunately, data from this laser is not available for a large fraction of the EAS data set and an analysis procedure has not been developed to make use of the data that is available.

The inter-site flasher (ISF) provides an alternative atmospheric monitoring device, although on a more local level. The ISF is a Xenon flasher located at the old Fly's Eye-II site. The flasher was used by the HiRes-I prototype detector and the Fly's Eye detectors. At the time of commissioning of BigH, the pointing direction of the flasher was changed so that the flasher track now goes through as many as 11 BigH mirrors. The flasher is setup to fire automatically every night. Five flasher shots are taken in quick succession ($\sim 1\,\mathrm{sec}^{-1}$) every seven minutes. The exact location of the ISF is known, but, the exact pointing direction was not measured. Instead, the pointing direction was inferred from analysis and Monte Carlo simulation.

The main advantage of the ISF is that data from it is available for all nights that BigH was run. Another advantage is the fact that the analysis of that data is rather simple. The main disadvantage is the fact that the flasher track passes only a few kilometers from the detector, and because of its fixed geometry, only provides information about a very localized portion of the atmosphere.

The ISF data and the information obtained from the simple analysis described below do not provide sufficient information to apply atmospheric corrections to the CR data. A more detailed analysis based on the steerable laser system is required. As the latter is unavailable, no atmospheric corrections were applied to the CR data used in the spectrum measurement described in this thesis. The ISF data does allow us, however, to examine the atmospheric conditions on a particular night, and make a qualitative judgment about whether the atmospheric conditions were better or worse than the "average atmosphere". This is done for those nights were CR events with reconstructed energies in excess of 10^{20} eV were observed.

5.5.1 Atmospheric Calibration Using the ISF Data

The analysis procedure for the ISF data described here is essentially the same as the procedure used for the Fly's Eye detector. The original analysis is described in [33]. The aerosol phase function, shown in figure 6.2, is peaked in the forward direction and has a minimum at an angle $\sim 110°$. This implies that the amount of scattered light from a beam should be insensitive to aerosols, at large scattering angles, but sensitive to aerosols at small angles. For moderate aerosol concentrations, Rayleigh scattering dominates over aerosol scattering at large scattering angles. Since Rayleigh scattering does not change with time, then the ratio of light collected at small/large scattering angles can be used to estimate the amount of aerosols.

The ISF track crosses 11 BigH mirrors (figure 5.3). The first mirrors to see the track view it at small scattering angles and the later mirrors at large scattering angles. In the analysis, the track is divided into 4° azimuthal bins, i.e. four bins per mirror. The number of photoelectrons for all tubes in a bin is summed to give the total bin signal. The geometry of the track relative to the mirrors is used to calculate the scattering angle relative to the center of each bin (figure 5.4).

After examining the bins to determine the size of signal fluctuation with time (i.e. with different aerosol concentration) it was found that the two bins marked in the mirror ID plot, figure 5.4, show the most (second bin in mirror 16) and least (first bin in mirror 10) fluctuation respectively. These are the bins, predicted by scattering theory, to be of interest since they would be most/least sensitive to aerosol scattering. Below, "ratio" or R(23,18) refers to the ratio of the signal(second bin in mirror 16) / signal(first bin in mirror 10). R(23,18) should be read as the ratio of the signal in the second bin in the third mirror along the ISF track (cf. figure 5.3) to the signal in the first bin in the eighth mirror along the track.

Figure 5.5 shows a histogram of the ratio R(23,18) for all the ISF shots collected over a two year period. Note that it cuts off sharply at the lower end. This represents a molecular atmosphere; one with negligible aerosol concentration. The

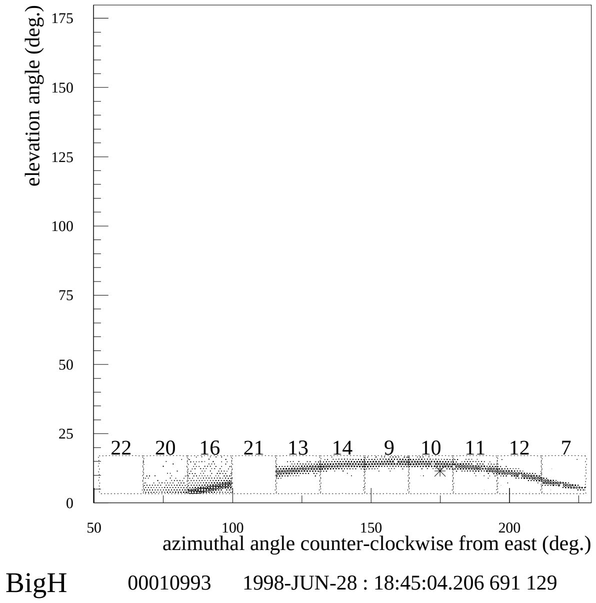

Figure 5.3. BigH event display showing the ISF track. Mirrors 20, 16 view the beginning of the track (small scattering angle,) mirrors 12, 7 view the track as it is moving away from the detector (large scattering angle).

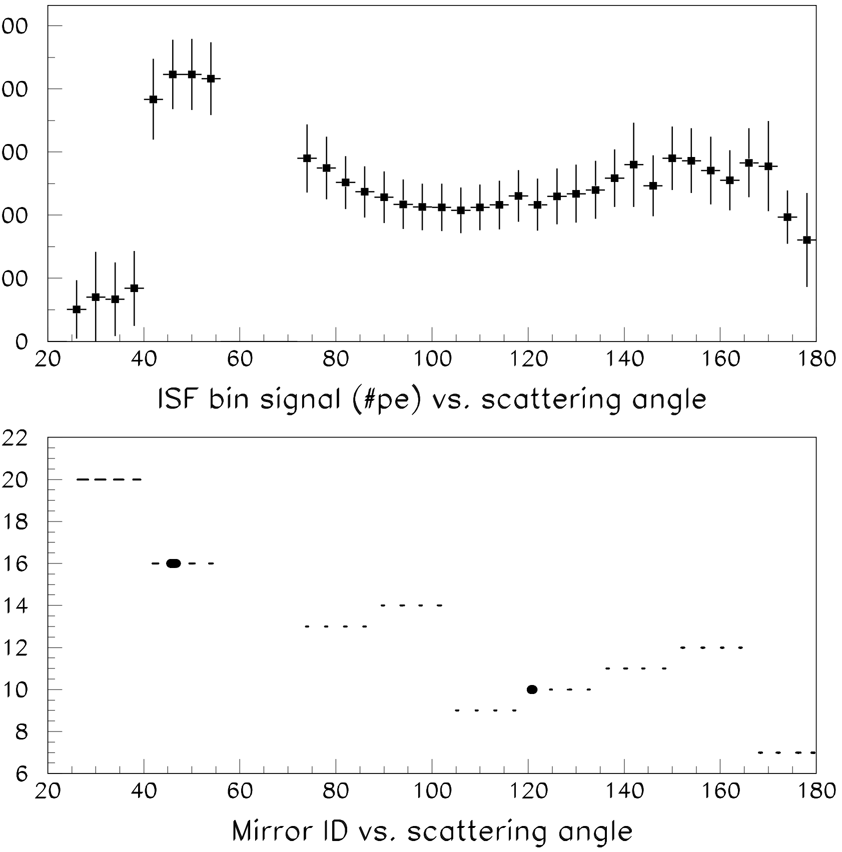

Figure 5.4. Profile histogram of binned tube signals. Four bins correspond to each mirror that sees the track. Mirror IDs are the numbers printed next to the mirrors in figure 5.3.

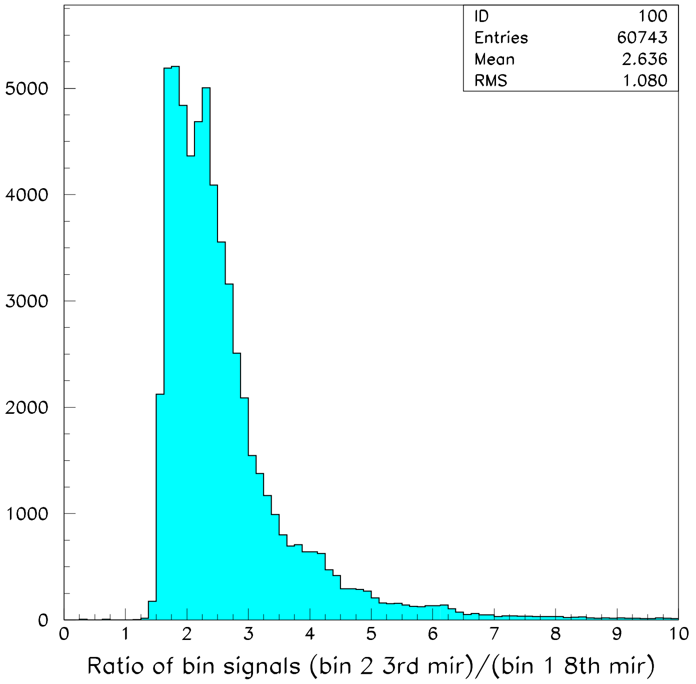

Figure 5.5. Ratio of ISF light scattering at small and large scattering angles. The lower edge represents a molecular atmosphere, the average corresponds to the 1976 standard desert aerosol model.

mean of the distribution shown in figure 5.5 corresponds to the standard desert aerosol model atmosphere.

Figure 5.6 shows the variation of the ratio with time for progressively smaller time intervals. Starting with the monthly average for the year 1998, then the daily average over the February-March run, the hourly average of one day in February, and finally the average of individual sets of shots within one hour on that day. Recall that a set of five shots is taken every seven minutes.

The detector response to the ISF can be simulated by the detector Monte Carlo. The ratio R(23,18) obtained from the simulated data can be calculated for different atmospheric (aerosols) conditions and compared with the real data. This allows us to compare the atmospheric model used in the MC and reconstruction with the actual atmospheric conditions at Dugway Utah, as inferred from the ISF data.This

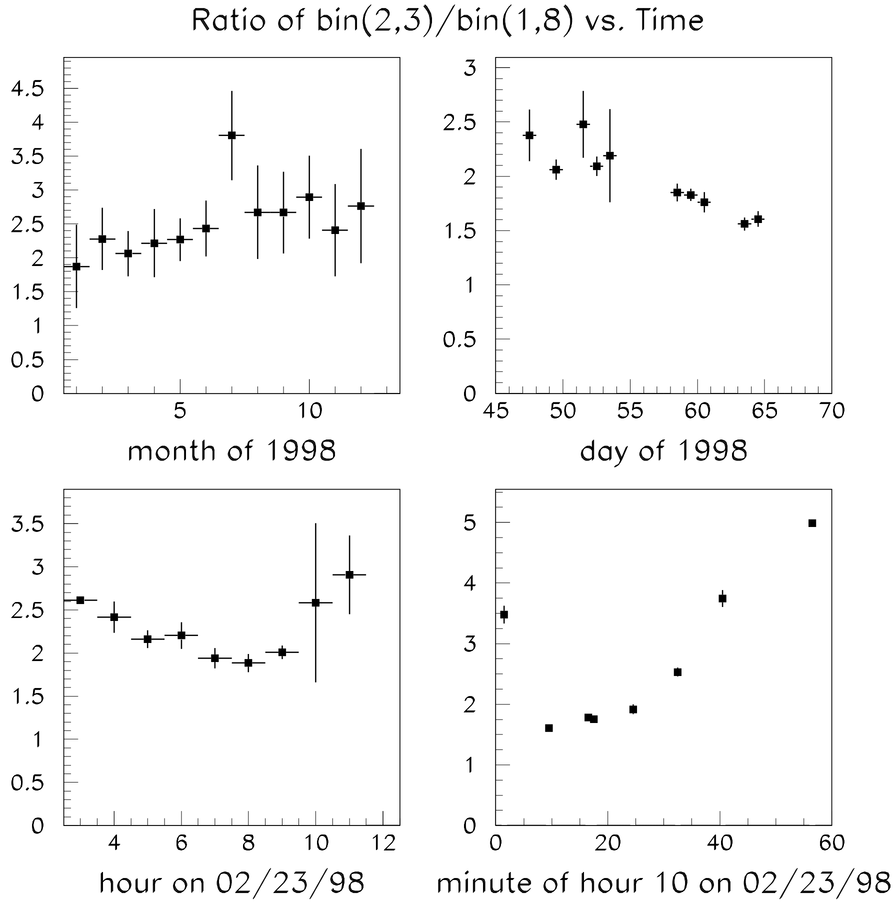

Figure 5.6. Ratio of ISF light scattering at small and large scattering angles as a function of time.

comparison was performed, and will be described after the a discussion of the atmospheric model is presented in chapter 6.

CHAPTER 6

DETECTOR MONTE CARLO

The detector Monte Carlo (MC) serves two important functions: the detector aperture calculation, and resolution studies of the reconstruction procedure, are both done using the detector Monte Carlo. For this purpose, the simulated detector has to mimic all of the important features of the real detector, and the simulated events have to be representative of real events. Moreover, the processes of light production, propagation, and detection by the detector optics must be modeled accurately.

The detector MC is used in the reconstruction process to estimate the response of the detector (tube signals and trigger times) to a given shower geometry and energy. In this capacity, a modification is made to the code to remove the fluctuations inherent in the real shower process, and the analytic form of the average behavior is used instead.

This chapter contains a detailed description of the physical models used in the MC and the reconstruction programs. The presentation will be made in the context of explaining shower simulation by the MC. Where differences between the Monte Carlo and the reconstruction program exist, e.g. in the implementation of the shower lateral width, the difference will be explained. For use with the BigH data, we developed a new simulation code, which is referred to as mc97. The description in this chapter will be restricted to this particular program.

The rest of the chapter is organized in five sections, each corresponding to one stage of the simulation. The sections are presented in the same order as the order that the simulation proceeds in, namely the simulation of:

- Shower development: Shower geometry and profile.

- Light production: Čerenkov and fluorescence light production.
- Light propagation: Rayleigh and aerosol scattering and ozone absorption.
- Detector optics: mirror geometry and PMT response.
- Detector electronics: signal filtering and trigger logic.

6.1 Monte Carlo EAS

Monte Carlo showers are generated with an energy E , selected either according to a power-law spectrum, or from a uniform energy distribution under program selection. drawn from an energy spectrum of power law form, or from a uniform energy distribution. The Gaisser-Hillas (G-H) parameterization of the shower profile given in equation 3.2, is used to generate the longitudinal development of the shower. The G-H parameters are chosen as follows. First the depth of first interaction, x_0, is chosen from a probability density of the form:

$$p(x_0) = e^{-x_0/\overline{x_0}} \tag{6.1}$$

with $\overline{x_0} = 70gm/cm^2$ for protons and $\overline{x_0} = 15gm/cm^2$ for iron. Second, the depth of shower maximum, x_{max}, is calculated based on the following "elongation" formulae:

$$\begin{aligned} x_{max} - x_0 &= 725.0 + 55.0 \times (\log(E) - 18) - \overline{x_0} \text{ (proton)} \quad (6.2) \\ x_{max} - x_0 &= 650.0 + 55.0 \times (\log(E) - 18) - \overline{x_0} \text{ (iron)} \quad (6.3) \end{aligned}$$

Finally, the shower size at shower maximum, N_{max}, is calculated according to:

$$N_{max} = E/1.3 \times 10^9 \tag{6.4}$$

with E measured in eV for proton and iron showers. This choice of N_{max} is approximately equivalent to Linsley's parameterization of missing energy [34]: The energy contained in the Electromagnetic component of the shower is related to the total energy by

$$E_{em}/E = 0.860 - 0.072E_{em}^{-0.149} \tag{6.5}$$

where E_{em} is proportional to the integral of the shower profile:

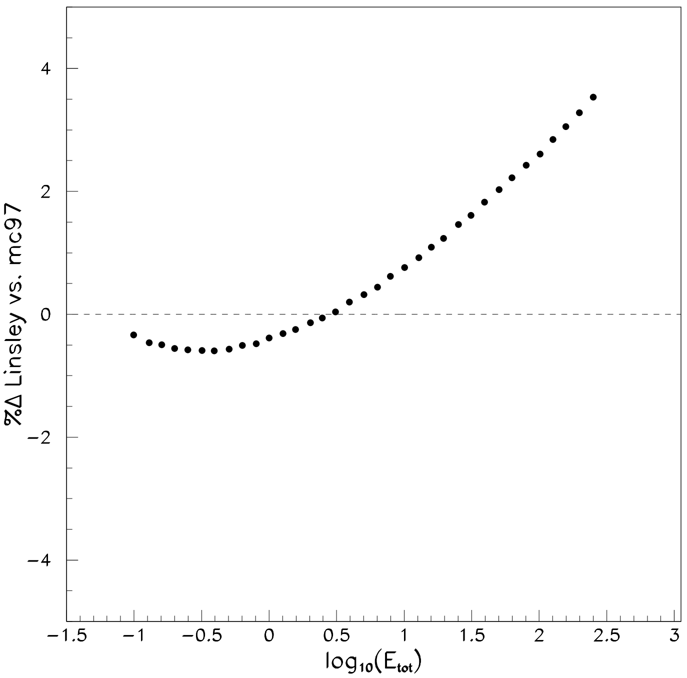

Figure 6.1. Percent difference between mc97 and Linsley's formula for the electromagnetic energy as a fraction of the total shower energy.

$$E_{em} = 2.18\,\text{MeV} \int N_e(x)\,dx \tag{6.6}$$

For the G-H parameterization, the integration gives:

$$E_{em} = 2.18\,\text{MeV}\ \times \lambda\ \exp(\alpha(1-\ln(\alpha)))\Gamma(\alpha+1) \tag{6.7}$$

where $\alpha = (x_{max} - x_0)/\lambda$. Figure 6.1 shows the percentage difference between E_{em} calculated from equation 6.7 (i.e. in mc97) and the Linsely's parameterization (equation 6.5).

The ratio E_{em}/E is theoretically composition dependent and may differ by $\sim$ 10% between proton and iron initiated showers. Linsley's parameterization represents an average over the two compositions. For event reconstruction the total energy is estimated by first integrating the shower profile with the reconstructed profile parameters given in equation 6.7, and then applying a correction according to equation 6.5.

Simulated showers are generated with an isotropically random flux. The arrival direction is generated from uniform distributions of $\cos(\theta_{sh})$ and ϕ_{sh}, and the shower impact parameter R_p chosen from a distribution weighted by R_p^2 between selected minimum and maximum values. One final parameter, ϕ_{R_p}, which represents the azimuthal angle of the detector about the shower axis is chosen from a uniform distribution from 0 to 2π. The resulting shower track is tested for intersection with the ground and the "top" of the atmosphere (set arbitrarily at 70 km in altitude) to decide whether or not a shower with this geometry would actually develop in the atmosphere. For those showers that do intersect the atmosphere, the calculation of the shower development then proceeds.

The shower track is then subdivided into up to 1000 segments, where each segment is required to span no more than $3\,\mathrm{g\,cm^{-2}}$ in depth, and subtend at most $0.23°$ as seen from the detector. The shower development is followed to a maximum depth of $2000\,\mathrm{g\,cm^{-2}}$ from the x_0 point. At each track point (endpoint of a track segment), the shower depth, size, age, and the Moliere multiple scattering radius are calculated and stored. The shower size is calculated from the G-H function, and the age parameter is defined by $s = 3/(1 + 2x_{max}/x)$. The Moliere radius, r_m, sets the scale for the shower lateral width, and is given by $r_m = X_0 \times E_s/E_c$ where $X_0 = 37.1\,\mathrm{g\,cm^{-2}}$ is the radiation length for electrons in air, $E_s = 21\,\mathrm{MeV}$ and the critical energy $E_c = 97\,\mathrm{MeV}$. The local atmospheric density is used to convert from r_m in $\mathrm{g/cm^{-2}}$ to meters.

6.2 Light Production

Charged particles (mostly electrons) in the EAS generate Čerenkov light as they travel through the atmosphere at above the local speed of light. The amount of light produced at a point along the shower depends on the number of electrons with energies above the threshold energy for Čerenkov production and, the local atmospheric index of refraction. The number of Čerenkov photons produced per unit length can be written as [35]:

$$\frac{dN_\gamma}{dl} = \frac{2\pi\alpha}{c} \int d\nu \int_{E_t}^{\infty} dE f(E) \left(2\delta - \frac{m^2c^4}{E^2}\right) \tag{6.8}$$

where α is the fine structure constant, the first integral is over the frequency of the emitted radiation ν, and the second integral is over the electron energy distribution given by $f(E)$. The lower limit of the integral is the threshold energy, given by $E_t = mc^2/\sqrt{2\delta}$, with m being the electron mass and $\delta = n - 1$, where n is the index of refraction of air. The electron energy distribution, $f(E)$, is defined by the integral relation[35]:

$$F(E) = \int_E^{\infty} f(\tilde{E}) d\tilde{E} \tag{6.9}$$

where $F(E)$ is the fraction of the electrons in the shower with energies greater than E, and is given by [35]:

$$F(E) = \frac{34.8}{(40.4 + E)(1 + 10^{-4}E)^2} \tag{6.10}$$

In our calculations we use the approximation $m^2c^4 \ll E^2$ for the relevant energies, and the number of Čerenkov photons produced per unit length simplifies to:

$$\frac{dN_\gamma}{dl} = 4\pi\alpha\delta F(E_t) \int \frac{d\nu}{c} \tag{6.11}$$

The angular distribution of the Cerenkov light is also relevant, we use the following formula, taken from [36]:

$$\frac{dN_\gamma}{dl d\Omega} = \frac{dN_\gamma}{dl} \frac{e^{-\theta/\theta_0}}{2\pi \sin\theta} \tag{6.12}$$

with $\theta_0 = 0.83\, E_t^{-0.67}$.

The amount of fluorescence light emitted at a point in the shower development is directly proportional to the number of electrons at that point. The fluorescent yield has a small dependence on altitude and that dependence is taken into account in the detector Monte Carlo and reconstruction programs. Fluorescence light is emitted isotropically. The number of photons produced per unit length per unit solid angle is given by:

$$\frac{d^2N_\gamma}{dld\Omega} = \frac{YN_e}{4\pi} \tag{6.13}$$

where Y is the fluorescent yield in photons/electron/m, and N_e is the number of electrons in the shower.

The formula for fluorescent yield used in the detector MC is based on a recent measurement reported in [37]. In their measurement, Kakimoto *et al.* passed electrons with energies 1.4 MeV, 300 MeV, 650 MeV, and 1000 MeV through air at various temperatures and pressures, and fit the measurements to the formula 6.14, to obtain values for the constants $A_1, A_2, B_1,$ and B_2.

$$Y = \frac{\left(\frac{dE}{dx}\right)}{\left(\frac{dE}{dx}\right)_{1.4MeV}}\rho\left\{\frac{A_1}{1+\rho B_{1\sqrt{t}}} + \frac{A_2}{1+\rho B_{2\sqrt{t}}}\right\} \tag{6.14}$$

where dE/dx is the electron energy loss, ρ, the air density in kg m^{-3} , and t is in kelvins. With this new measurement, the systematic uncertainty in the energy determination of an UHECR primary due to scintillation efficiency drops from $\sim$ 30% to $\sim$ 10%, a significant improvement.

6.3 Light Propagation

Fluorescence light propagating from the EAS to the detector suffers attenuation by scattering from the air molecules and aerosols, and from absorption by Ozone. The same processes also apply to Čerenkov light. However, in the case of Čerenkov light, scattering of the Čerenkov beam into the field of view of the detector adds a significant contamination to the light signal. Thus, there are two cases to consider: (1) scattering of light out of the Cerenkov beam along the shower direction, and (2) the attenuation of the scattered Čerenkov and the direct fluorescence light as the light propagates from the shower to the detector.

Because the amount of scattering depends on the density of scatterers, the two cases above are treated differently in the simulations. In case (1), the calculation is done for one track segment at a time. Since a track segment has a limited length, the density of the scatterers can be taken as constant, and an expression of the form dN_γ/dl can be used to give the number of photons scattered out of the beam per meter. In case (2) however, the path from the source (track segment) to the detector is not subdvided into small intervals and hence, an integration over the density is required, to do the calculation. In this case the attenuation is described by a transmission factor.

6.3.1 Rayleigh Scattering

Rayleigh scattering refers to the scattering of light by the air molecules. The theory of Rayleigh scattering is well established, and is covered in texts on electrodynamics such as Jackson. Here, I will just present a summary of the formulae used by the MC.

The number of scattered photons per unit length is given by [38]:

$$\frac{dN_\gamma}{dl} = -\rho \frac{N_\gamma}{x_R} \left(\frac{400}{\lambda} \right)^4 \tag{6.15}$$

where ρ is the atmospheric density, $x_R = 2970\,\mathrm{gm\,cm^{-2}}$ is the mean free path for scattering at 400 nm. The angular distribution is given by [38]:

$$\frac{d^2 N_\gamma}{dl d\Omega} = \frac{dN_\gamma}{dl} \frac{3}{16\pi} \left(1 + \cos^2 \theta \right) \tag{6.16}$$

And Lastly, the transmission factor for propagation through a path length of $\Delta x\,\mathrm{gm\,cm^{-2}}$ is given by:

$$T_R = \exp \left[-\frac{\Delta x}{x_R} \left(\frac{400}{\lambda} \right)^4 \right] \tag{6.17}$$

6.3.2 Aerosol Scattering

Aerosol scattering differs from Rayleigh scattering in two ways:

- The size of the scatterers is comparable to, or larger than the light wavelength, and has a variable distribution, making an analytic solution very difficult.
- The concentration of aerosols is not known and varies with location and with the time.

For our purposes a simple parametric model of aerosol scattering is used, where the number of aerosol scattered photons per unit length per steradian is given by:

$$\frac{d^2N_\gamma}{dld\Omega} = -\frac{N_\gamma}{L_M(\lambda)}\rho_a(h) \times \varphi(\theta) \tag{6.18}$$

Here $\rho_a(h)$ represents the reduced aerosols density at height h above the ground, $\varphi(\theta)$ the scattering phase function at scattering angle θ, and $L_M(\lambda)$ the wavelength dependent horizontal extinction length. The reduced density takes the form

$$\rho_a = \begin{cases} 1 & h < h_m \\ e^{-(h-h_m)/H_a} & h \geq h_m \end{cases} \tag{6.19}$$

where h_m is an adjustable parameter that represents the height of the mixing layer measured from the ground (not sea level), and H_a is the scale height of the aerosols. For this analysis of BigH data the values $h_m = 0\,\mathrm{km}$, and $H_a = 1.2\,\mathrm{km}$ were used. The aerosol model with this choice of parameters is equivalent to the U.S. Standard Desert Atmosphere.

The scattering phase function used is based on the Longtin desert aerosol model at a wind speed of 10m/s c for 550 nm [39]. The scattering cross section is very strongly peaked in the forward region, as shown in figure 6.2.

The extinction length is inversely proportional to the actual density of the aerosols. The wavelength dependence used is based on the Etterman extinction model, shown in figure 6.3. The plot shows the ratio of the extinction length at λ to that at 334 nm. The value $L_M(334\,\mathrm{nm}) = 12\,\mathrm{km}$ is used in this analysis.

The aerosols transmission factor through a reduced slant depth of $\Delta s\,\mathrm{m}$ (the integral of the reduced aerosol density from the source point to the detector point) is given by:

$$T_A = \exp(-\Delta s/L_M) \tag{6.20}$$

where L_M is calculated at the appropriate wavelength

6.3.3 Ozone Absorption

Light attenuation due to Ozone absorption is given by:

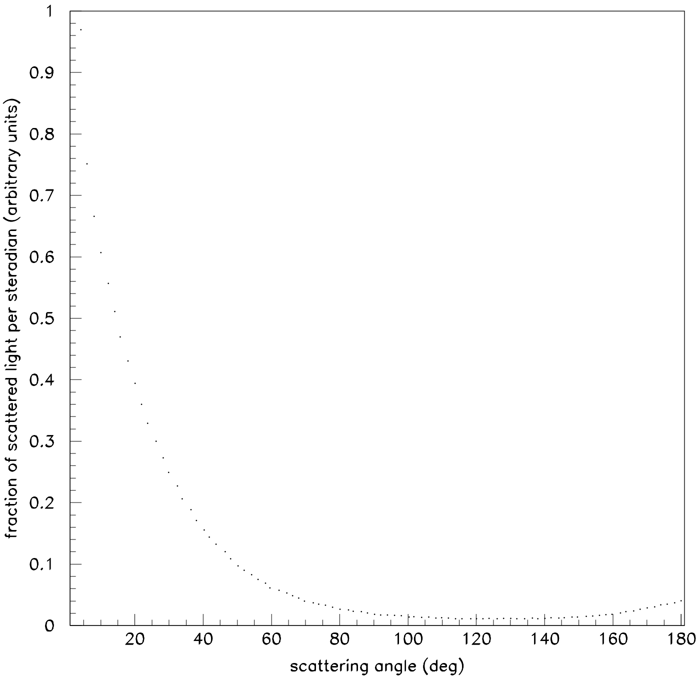

Figure 6.2. The Longtin phase function

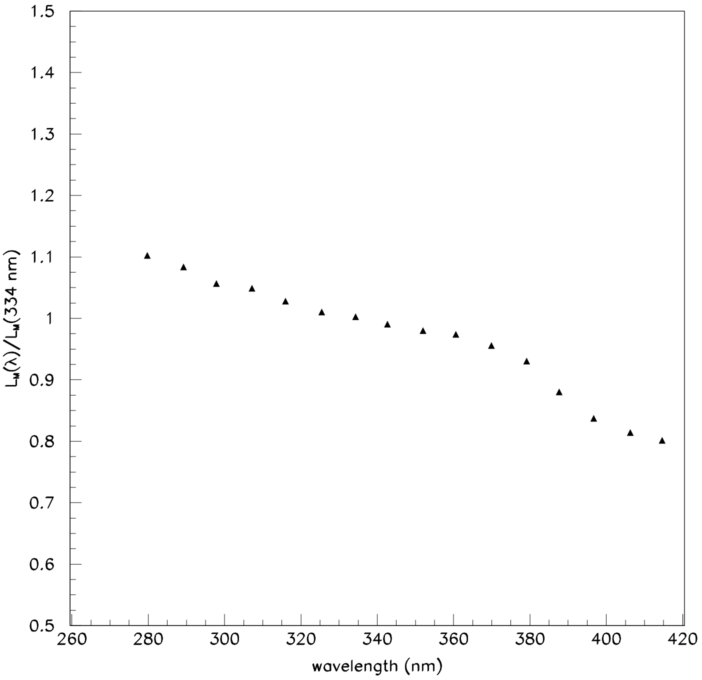

Figure 6.3. The Etterman model of the wavelength dependence of the aerosols extinction length.

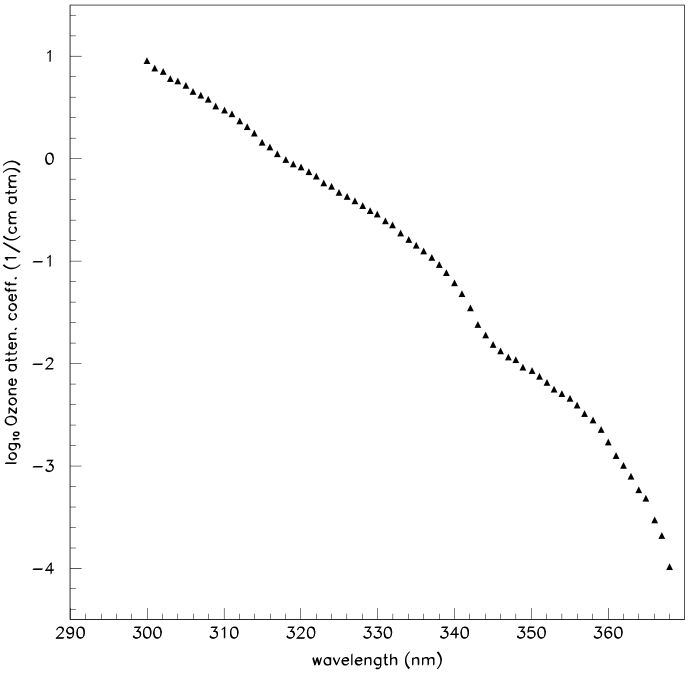

Figure 6.4. The Ozone attenuation coefficient as a function of wavelength.

$$\frac{dN_\gamma}{dl} = -N_\gamma \, \rho_{O3}(h) \, A_{O3} \tag{6.21}$$

where A_{O_3} is an attenuation coefficient, and ρ_{O_3} is the height-dependent Ozone density. The Ozone attenuation coefficient has a very strong wavelength dependence, as seen in figure 6.4. The variation of the Ozone density with altitude is shown in figure 6.5. The data contained in the figure is based on data from the USAF Handbook of Geophysics and Space Environment.

Transmission through Ozone is treated in a similar way to the cases of scattering:

$$T_{O_3} = \exp(-\Delta x_{O3} A_{O3}) \tag{6.22}$$

Here T_{O_3} is the transmission factor, Δx_{O_3} is the integrated ozone density (slant depth) between the source and detector point.

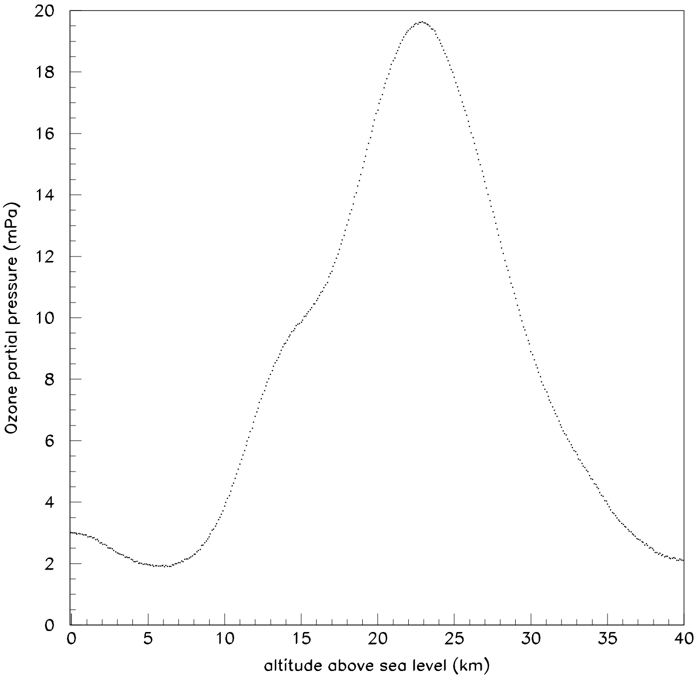

Figure 6.5. Ozone concentration as function of altitude.

6.4 Detector Optics

The response of the *real* HiRes detector to an EAS is recorded as a set of triggered tubes with their respective signals and trigger times. The tube signal represents (after calibration) the total number of photons seen by the tube over a time window of $5.6\,\mu$s around the tube's trigger time. The formulas for light production and propagation given above relate to the light *flux.* To get from flux to *number of photons collected* we need to account for the light collecting area of the detector, and the light collecting efficiency of the various components of the detector.

The calculation of the number of photoelectrons collected by the tubes observing the shower is done in two steps. First, an analytic calculation is used to estimate the number of photo-electrons from each track segment that would be collected by a disc shaped mirror at the same location as the actual mirror. Then, the photo-electrons are individually ray-traced to the PMTs, taking into account the actual mirror shape. What follows is a description of the these two steps. We start by examining the analytic part.

The analytic calculation proceeds as follows. First the number of *photons* produced or scattered out from a track segment is calculated, i.e. the expressions $d^2N_\gamma/dld\Omega$ (sections 6.2 and 6.3) are multiplied by the length of the segment (δl) to give $dN_\gamma/d\Omega$. Second, the number of *photoelectrons* produced at the track segment and collected by the disc shaped mirror is calculated according to:

$$\begin{aligned} N_{pe} &= \sum_{\lambda=300}^{420} \left(\frac{dN_\gamma}{d\Omega}(\lambda,\theta_e)\bigg|_{scin} + \frac{dN_\gamma}{d\Omega}(\lambda,\theta_e)\bigg|_{ascat} + \frac{dN_\gamma}{d\Omega}(\lambda,\theta_e)\bigg|_{rscat} \right) \\ &\times\; T_R(\lambda)\, T_A(\lambda)\, T_{O_3}(\lambda)\, T_{UV}(\lambda)\, R_m\, QE(\lambda)\, \delta\Omega \end{aligned} \tag{6.23}$$

where, the sum over the wavelength λ is performed in 1 nm steps, and θ_e is the light emission angle. The labels *scin*, *ascat*, and *rscat* stand for scintillation and, aerosol and Rayleigh scattered Čerenkov light respectively. The Rayleigh, aerosol, and Ozone transmission factors are denoted by T_R, T_A, and T_{O_3} respectively, T_{UV} is the UV filter transmission factor, R_m is the mirror reflectivity, and QE is the

PMT quantum efficiency. The term $\delta\Omega$ stands for the solid angle subtended at the source (center of track segment) by the mirror, and is given by:

$$\delta\Omega = \frac{A^0_{eff}\cos(\theta_m)}{d^2} \tag{6.24}$$

where θ_m is the off-axis angle of the source point and d is the distance to the source. $A^0_{eff}\cos(\theta_m)$ is the projection of the area of the disc shaped mirror, along the direction from the detector to the shower segment.

In equation 6.23, the wavelength dependence of the fluorescence light is extracted from the spectrum shown in figure 3.1, the Cerenkov frequency distribution is given by equation 6.11 and, the wavelength dependence of the scattering processes is calculated as given by the appropriate formulae from the previous sections. The mirror reflectivity is taken to be 0.8 independent of wavelength, see section 4.3.1. Figure 6.6 shows the wavelength dependence of the PMT quantum efficiency and the UV filter transmission. The combined efficiency due to mirror reflectivity, QE, and UV filter transmission is also shown.

The same analytical calculation (equation 6.23) is employed by both the Monte Carlo and the reconstruction program. Two differences exist in the reconstruction program, both introduced to minimize computation time. These differences are:

- For reconstruction, the shower track is divided into a fewer number of track segments, that is to say, the lengths of the track segments are roughly twice that described in section 6.1. The effect of the coarser division on the calculated tube signals was investigated and found to be negligible for track segment lengths of up to $10\,\mathrm{gm\,cm^{-2}}$.
- The reconstruction program uses 5 nm wavelength bins instead of 1 nm. Again, the effect of increasing the bin width was studied and found to be on the order of 1%.

The second part of the tube signal calculation is implemented differently by the Monte Carlo and reconstruction. For event simulation the ray tracing includes

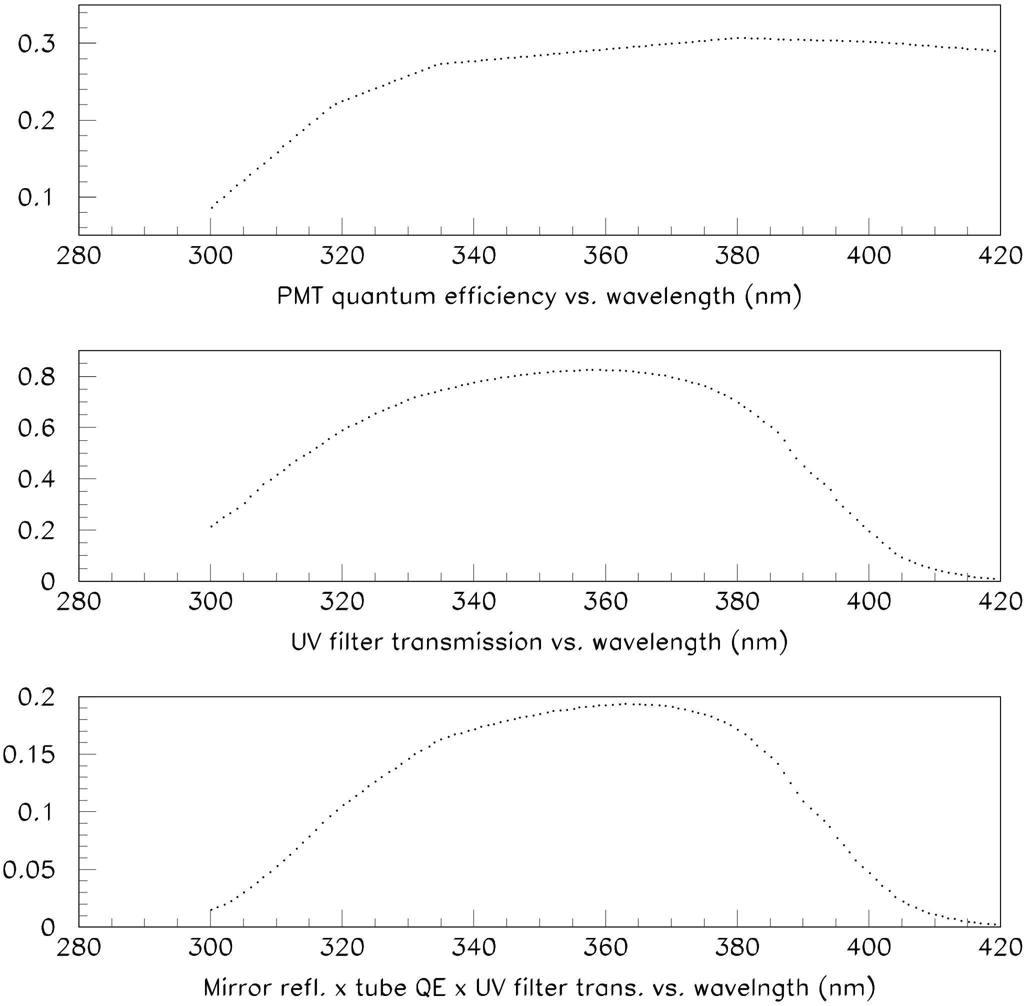

Figure 6.6. Wavelength dependence of the PMT quantum efficiency and the UV filter transmission curve. The mirror reflectivity is assumed constant (=0.8) and independent of wavelength.

fluctuations and other random effects, while in the reconstruction procedure the average behavior is calculated. Both implementations will now be discussed in turn.

6.4.1 Ray Tracing: Monte Carlo implementation

The ray tracing part of the calculation accounts for the following effects:

1. Fluctuations in the number of pe reaching the detector.
2. The lateral spread of the electrons in the shower (shower lateral width).
3. The composite shape (4-leaf clover) of the mirror, and the obscuration of the mirror by the PMT cluster.
4. The effect of spherical aberration and mirror imperfections.
5. The PMT response profile

Fluctuations in the number of photo-electrons (pe) is implemented by ray tracing a number of pe drawn from a Poisson distribution with a mean value given by equation 6.23. The initial longitudinal position of each pe is chosen randomly (uniform distribution assumed), with the lateral displacement from the shower axis drawn from the NKG formula, given in equation 3.4. The shape of the mirror and the cluster obscuration are included in the simulation by testing the impact point of each ray traced pe to see (a) whether or not it falls within the area defined by the actual extent of the mirror, (b) whether it hits the back of the cluster, and (c) whether on reflection by the mirror, it hits the front face of the cluster.

The landing position of a pe at the face of the PMT cluster is fluctuated by a gaussian of $\sigma = 0.25\,\mathrm{cm}$ to simulate the effect of the mirror spot size. The randomized position is then tested to see if it falls within the acceptance of a PMT. Those pe falling within a tube are added to the signal of that PMT, weighted by the PMT response profile, shown in figure 6.7.

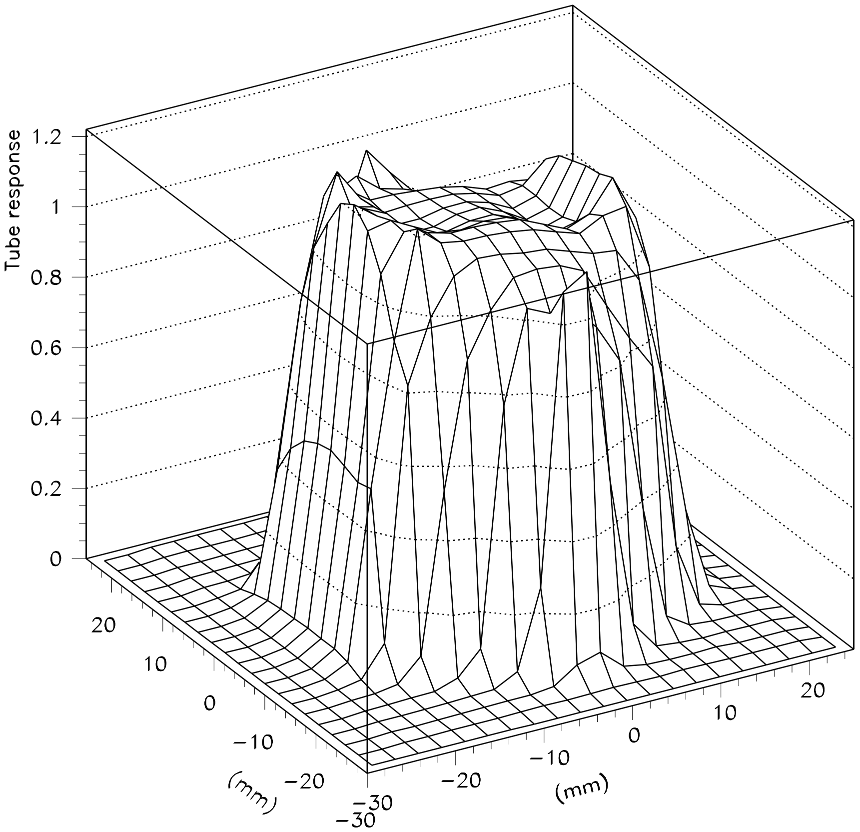

Figure 6.7. Tube profile used in simulation.

6.4.2 Ray Tracing: Reconstruction program implementation

The reconstruction program uses a look-up table instead of ray tracing individual pe's. For each of the 256 tubes in the cluster, the look-up table gives the "tube response" to a point source located at given angular distance from the center of the tube, as shown in figure 6.8. In this context, the "tube response" refers to: the fraction of the number of pe incident on the tube at a given angle that register as "hits". The table was constructed using the Monte Carlo and it includes the effects of the mirror shape and obscuration, spherical aberrations, and the tube response profile.

The fluctuations in the number of pe reaching the detector are random and are not included in the reconstruction procedure. Instead, the expected RMS fluctuation is used as the error in the fitting procedure. Furthermore, instead of randomly generating the initial point of each pe, a continuous smooth distribution is used as the source. The ray tracing table is then used to calculate the contribution of each source point to the tube's signal. Three parameters identify the initial position of a pe relative to the position of the shower segment center: Distance along the shower axis z, radial distance from the shower axis r, and azimuthal angle φ. The radial position calculation is the only nontrivial part of the calculation, and will be examined next.

The NKG function, given previously in equation 3.4, describes the electron density as a function of the shower age,s (see section 3.2) and the radial distance from the shower axis in units of the Moliere Multiple scattering radius r_M . Although the density falls to zero only asymptotically with r, most of the electrons are contained within a few r_M from the axis, as illustrated in figure 6.9. In particular, for the range $s = 0.8 - 1.3$ about 95% of the electrons are contained within a radius equal to $5r_M$. This feature implies that truncating the radial density function to a finite distance is an acceptable approximation. The electrons that would be missed can be recovered by re-normalizing the density such that 100% of the electrons fall within $5r_M$ but the shape of the function is preserved.

The actual implementation of the shower lateral width used in the reconstruction

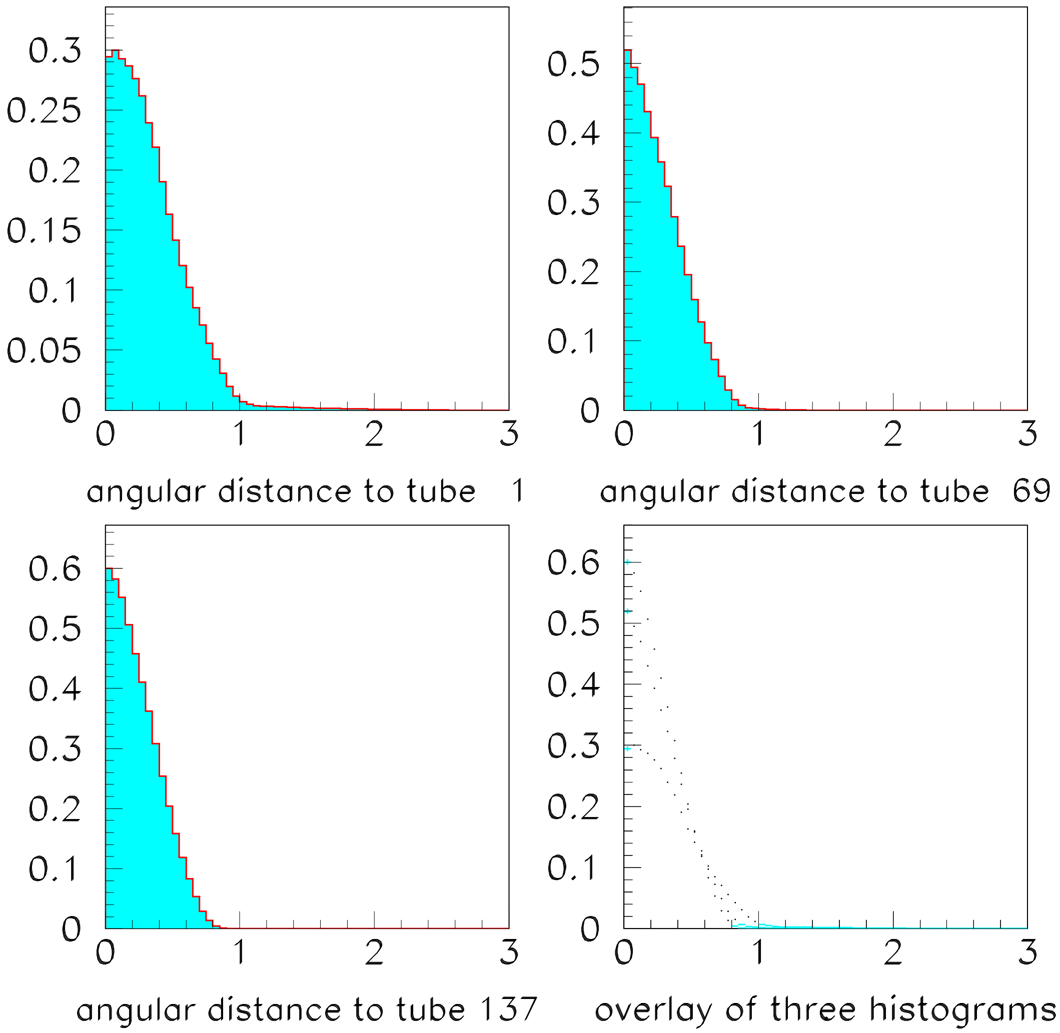

Figure 6.8. Ray tracing table entries for three tubes. Tube 1 is at the corner of the cluster, tube 137 is close to the center (i.e. to the mirror axis), and tube 69 is a few degrees away from the mirror axis.

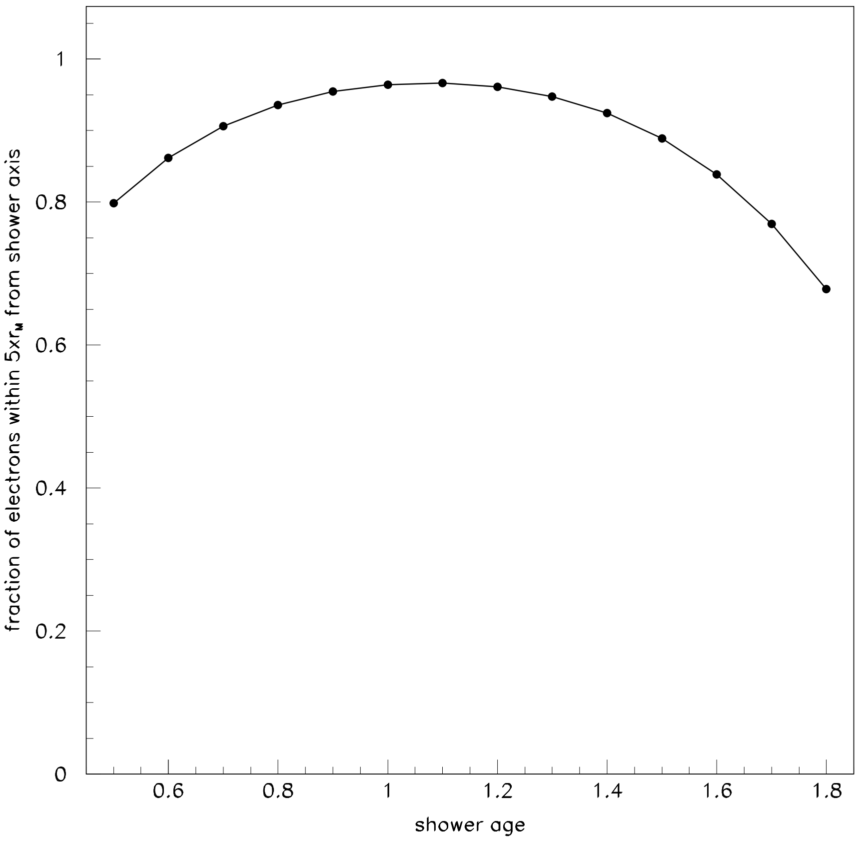

Figure 6.9. The total fraction of electrons contained within $5r_M$ from the shower axis based on the NKG electron lateral distribution.

parameterizes the continuous lateral spread of electrons by a discrete set of bins. The radial range $r = 0$ to $r = 5r_M$ is divided into five bands, or bins. The center of each band is the average radial distance of electrons in the bin, weighted by the NKG function. The azimuthal range $[0, 2\pi]$ is divided into six bins of equal angular range. The fraction of electrons in a radial bin is calculated by integrating the NKG function with the bin boundaries as the integration limits. The number thus obtained is divided by the number of angular bins to find the fraction that falls within each 2-dimensional bin, as summarized in equation 6.25.

$$N_{ij} = N_{pe} \times f_N(r_j) \times (1/n_\varphi) \tag{6.25}$$

where N_{pe} is the total number of pe from equation 6.23, N_{ij} is the number of pe in angular bin $i = 1, .., n_\varphi$ and radial bin $j = 1, .., 5$, $f_N(r_j)$ is the fraction of pe in a radius $(j-1)r_M < r \leq jr_M$ divided by the total fraction of electrons in the range $0 < r \leq 5r_M$. f_N also depends on the shower age and the appropriate value is used.

6.5 Detector electronics

Simulation of the electronics is implemented in the MC event generator but is not needed for the reconstruction program. The overall goal of the simulation is twofold: first, to simulate the action of the S/H electronics on the tube signals and second, to simulate the trigger requirements of the detector. In both instances, the real time behavior of the electronics has to be implemented. To achieve this, the simulation is done for one mirror at a time, and a time interval over which signal and noise are to be recorded for all the tubes in the mirror is defined. This is done in the following manner:

We first calculate the transit time, T_e, of the shower across the mirror, from its geometry. Second, an interval of $T_s = 25\,\mu$s corresponding to the time individual tube triggers are saved, must be pre-pended to T_e. This addition is needed to account for the possibility that a noise trigger had been formed prior to the transit of the shower, that would prevent subsequent trigger from the actual signal. Lastly, a further interval of $T_h = 50\,\mu$s is added to the end of the transit time, simulating the

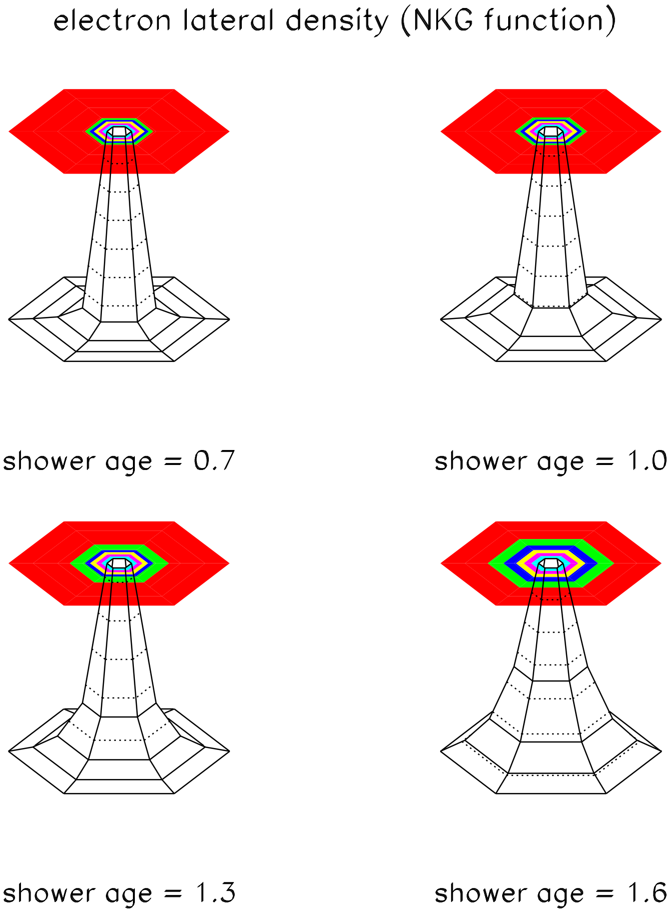

Figure 6.10. The electron lateral distribution used in shower reconstruction. Four distributions, at different values of the shower age, are shown.

actual gate of the mirror trigger which permits additional individual tube triggers to be included in an event. This "hold-off" is needed to allow the shower to finish crossing the FOV of the mirror before triggering is disabled. Thus a total time interval of $T_{tot} = T_e + T_e + T_h$ must be considered.

The simulation proceeds by dividing this interval into 20 ns time bins. Each tube in the mirror gets assigned a separate array of time bins. Sky noise is added to each bin for each tube from a Poisson distribution with a mean of 40 pe/μs. Shower pe which contribute to a tube signal (as determined by ray-tracing) are then added to that tube's array, in the appropriate time bin. When all shower pe had been added, the tube signals are "processed" to test for individual tube triggers.

Processing a tube's signal comprises the steps of: (a) adding PMT, pre-amplifier, and electronics gains, (b) sending the signal through a a low pass filter (see figure 4.9), (c) splitting the signal, and sending it to the trigger and integration circuitry, and (d) for each time bin, comparing the signal against a fixed threshold (500 mV) to test for tube trigger. In case of trigger, the trigger time is calculated and converted to an equivalent TDC, and the tube signal is integrated in the 5.6 μs time window and the integral is "digitized". Tube QDCs and TDCs are saved for all triggered tubes. A tube may trigger more than once. A noise trigger followed, after a time interval greater than 25 μs, by another trigger is possible and both triggers are saved.

After all the tubes in the mirror have been tested for trigger and saved, they are sorted in ascending order in trigger time. The ordered list thus formed, is now used to test for the formation of a mirror level trigger. A mirror level trigger requires that at least two subclusters trigger within a predefined time window. In turn, a subcluster trigger requires that at least three tubes (two adjacent) trigger within a predefined time interval.

To search for a mirror level trigger, the sorted list of tube trigger times is searched from the earliest tube trigger time, via a sliding time window of 25 μs. The first instance at which, the trigger conditions are met, is recorded as the mirror trigger time, and event information is written out accordingly. If the mirror trigger requirements are not met at any time during the total time interval T_{tot}, then the output of the MC will reflect this fact.

CHAPTER 7

DATA PROCESSING

An air shower can trigger one or more mirrors. Raw data from each mirror are recorded individually and transformed to the main DAQ computer where they are stored on disk. The raw data is then processed in order to extract physical parameters for the measured EAS. This processing is divided into several stages, referred to as "passes", each of which performs one or more specific tasks, divided into the following general categories:

Event building: Raw data packets from triggered mirrors and the central timing crate are merged into events. Mirror event packets contain digitized QDC and TDC values for triggered tubes. These are matched with timing packets from the CT to establish the absolute time of the mirror trigger as supplied by the GPS clock. Mirror events are then compared with one another to search for multi-mirror coincidences. This process is referred to as time matching.

Calibration: Raw data contains QDC and TDC values in native machine units. These are converted into photo-electrons and trigger times by applying PMT and electronics calibrations information.

Filtering: Random noise triggers are filtered out of the data stream. In addition to noise events, laser and flasher events are separated from EAS triggered events.

Event selection: EAS events are kept or dropped from the data set based on "quality": Events that are likely to suffer from poor reconstruction (based on Monte Carlo experience) are said to be of low quality and are removed. Close by events are also removed, as they are most likely to be low energy events.

Table 7.1. BigH data analysis stages and corresponding functions. The numbering of the passes reflects the order in which they are applied to the data.

Pass	Function
PASS0	Event building
PASS1	Calibration
PASS2	Filtering
PASS3	Reconstruction / Filtering
PASS3a	Filtering / Event selection
PASS3b	Event selection
PASS4	Reconstruction

Reconstruction: Shower geometry and profile are reconstructed in order to obtain an energy estimate for the primary CR.

Table 7.1 shows the division of the analysis tasks among the analysis stages. The numbering of the passes reflects the order in which they are applied to the data. The implementation of each of the data analysis passes will be described in this and the next chapter. This chapter includes a discussion of PASS0 and PASS1, the next chapter reviews the event selection, PASS2 and PASS3,3a,3b, and the main reconstruction procedure, implemented in PASS4.

Before we go into the details of the implementation, however, some definitions and naming conventions will be given. The data format and data analysis framework are presented next, followed by, a listing and a brief discussion of the various programs used for data processing. Finally, raw data and file naming conventions are described.

7.1 DST system

HiRes data is stored and manipulated in the form of DST (Data Storage Template) banks. A DST bank corresponds to a Fortran *common block* or a C *structure* with an associated collection of functions to read/write the structure and to dump the contents of the bank to the screen. A sketch of the system is shown in figure 7.1.

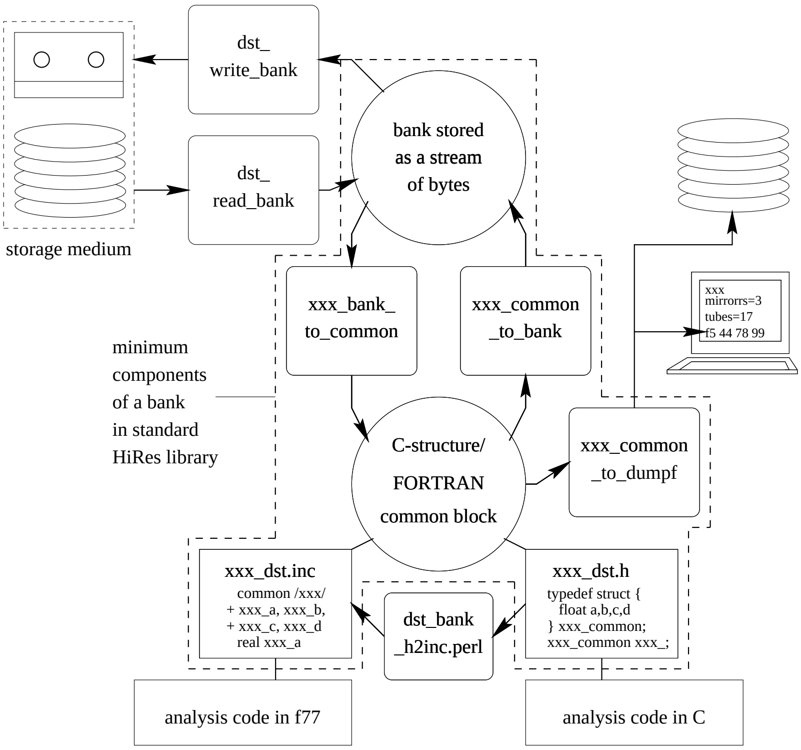

Figure 7.1. DST system

At each stage of processing, new information is calculated and stored for the event in a bank which is then added to the collection of banks which make up the event. In its data format, an event consists of a collection of banks bounded by a START and STOP banks. These are simple banks which contain only a string that reads “start” or “stop”. Several DST support routines are provided to handle *banklists,* to read/write an event as a single unit. These routines are used by most of the HiRes analysis programs.

The DST system has been in use since 1995. A large number of banks have been created for specifically different detectors (HiRes prototype, CASA/MIA, ...) and for different analysis chains. Banks used for BigH monocular analysis typically have names starting with the letter “H”. Below is a list of all the banks used for BigH data analysis:

HPKT1 the raw data packets generated and written by the DAQ computer.

HMC1 output of the mc97 Monte Carlo for each generated event. This includes the generated shower parameters and the detector response for triggered events.

HRAW1 the calibrated number of photons and trigger times for the triggered tubes in an event.

PASS2 statistical information from the Rayleigh filter for each event that successfully passes the filter.

HPLN1 shower-detector plane information from the amplitude-weighted plane fit for each successfully reconstructed event.

PRFC reconstructed shower profile parameters. This bank can contain the results of multiple fits for each event.

HCTIM geometrical parameters corresponding to PRFC_ profile parameters.

HCBIN binned light flux corresponding to PRFC_ and HCTIM parameters.

HSUM a summary of the detector operation for each raw data file. This includes mirror trigger statistics, tube thresholds, and other sundry information.

HRXF1 PMT gains and pedestals determined by RXF data and is used in the detector calibration procedure.

HCAL1 PMT gain conversion factors (QCD to photo-electrons, TDC to seconds) based on calibration data.

HPED1 tube QCD pedestals measured at the beginning and end of a night.

7.2 Programs

Data analysis tasks are divided among a number of programs. Each analysis *pass* is completed by executing one main program, except for calibration (PASS1) where several support programs are used alongside the main program. In general, a program reads an input file and writes out an output file. A convention is followed in naming the files. File names reflect the stage of the analysis and/or the bank names contained in the file. The date the data was taken is also coded into the name: data collected on year YYYY, month MM, day DD, is written to a file yYYYYmMMdDDpPP.*extension* where PP is a "part" number in the range 01-99. The names of the main programs used in each pass are shown in table 7.2 along with the input and output banks. Also shown are the input and output file names.

While examining the table, the following points should be noted:

- With the exception of *hma,* the output banks from each program are appended to the input banks comprising the event. HPKT1 is not written out along with HRAW1 in the output of *hma* due to its large size.
- As input to *hpass1,* HRAW1 contains the QDCs and TDCs for triggered tubes, but not the calibrated number of photons or trigger times. The latter are calculated by *hpass1.* As output of *hpass1,* the HRAW1 bank information is complete.

Table 7.2. Programs that implement the main analysis chain for BigH data. The first table shows the input/output banks. The second shows filename extensions. Data file names have the form yYYYYmMMdDDpPP.extension.

input bank	program	output bank
HPKT1	hma	HRAW1
HRAW1	hpass1	HRAW1
HRAW1	hpass2	PASS2
HRAW1	hpln	HPLN1
HRAW1	hpln -C	HPLN1
PASS2, HPLN1	ps3a_to_ps3b	-
HRAW1, HPLN1	htim_pfl	PRFC, HCTIM, HCBIN

input filename extension	program	output filename extension
.pkt.hal	hma	.ps0.dst
.ps0.dst	hpass1	.ps1.dst
.ps1.dst	hpass2	.ps2[d,h,u].dst
.ps2[d,h,u].dst	hpln	.ps3[d,h,u].dst
.ps2[d,h,u].dst	hpln -C	.ps3a[d,h,u].dst
.ps3a[d,h,u].dst	ps3a_to_ps3b	.ps3b[d,h,u].dst
.ps3[,a,b][d,h,u].dst	htim_pfl	.ps4[,a,b][d,h,u].dst

- PASS3 and PASS3a both use the same program. For PASS3a, the program is invoked with an additional command line argument.
- The program *htim_pfl* performs the profile and geometry reconstruction. Due to the nature of the problem, it is not possible to break it down into a set of simpler program. However, the output data is divided into separate banks.
- The output of hpass2 is written out to three separate files: down, horizontal, and up. This is indicated in the filename by appending one of the letters 'd', 'h',and 'u' to the string "ps2" in the extension. This tag is preserved through later passes.

The main function of the programs listed in table 7.2 are summarized below:

hma Perform time matching of event and time packets (raw data)

hpass1 Apply RXF calibration data to HRAW1 banks

hpass2 Filter out noise events with a "Rayleigh filter"

hpln Reconstruct the Shower-Detector plane, and filter out noise events

htim_pfl Reconstruct shower geometry and profile.

The output of *htim_pfl* contains the results from multiple fits for each event. The best fit is chosen from the set of multiple fits and statistical results are generated in the form of a PAW ntuple file by a program named *ps4_ntuple_main.* Yet another program, *hqd,* is used to display the reconstruction results. *hqd* is a modified version of another program, *qd,* used for the HiRes prototype analysis.

In addition to the main analysis programs, several support programs are used. Some of these are shown in table 7.3.

7.3 Raw Data

7.3.1 Raw data packets

The running of BigH is managed by a central computer that runs a control program called HAL. Commands are sent by HAL to the mirrors and data are received

Table 7.3. Calibration and support programs.

input bank	program	output bank
HPKT1_	hsum	HSUM_
HPKT1_	ontime	ascii file
ascii file	hrxf	HRXF1_
HPKT1_ (calib packets)	hca	HCAL1_
HPKT1_ (event packets)	hped	HPED1_

input filename extension	program	output bank
.pkt.hal	hsum	.hsum.dst
.pkt.hal	ontime	ascii file
ascii file	hrxf	.hrxf1.dst
.cal.hal	hca	.hcal1.dst
.noise-closed.hal	hped	.hped1.dst

from the mirrors them over ethernet. This communication uses the standard UDP protocol and information is organized into ethernet “packets”. To store the data in the standard DST format, these packets are “framed” individually into HPKT1 banks.

There are many types of packets allowed within a HPKT1 bank. Most of these, record the condition of various detector components such as voltages, temperature readings, ...etc. For our purposes the most important packet types (as defined in the header file hpkt1_dst.h) are:

1. HR_TYPE_TIME: generated by the central timing crate in response to a mirror trigger. It records the absolute time of mirror hold-off from the GPS clock.
2. HR_TYPE_EVENT: generated by a triggered mirror. It records the list of triggered tubes their QDCs and TDCs.
3. HR_TYPE_CALIB: electronics calibration packets. Records the response of the tubes to different hight/width combination of pulses from the PPG.

Other packet types used by our analysis include HR_TYPE_MINUTE and HR_TYPE_NOTICE. These contain dead-time and start/stop information for each mirror, and are used in the calculation of the integrated exposure of the detector.

7.3.2 Raw data files

Each time the detector is run, data are written to a set of files similar to the list below:

1. yYYYYmMMdDDpPP.pkt.hal: observational data
2. yYYYYmMMdDDpPP.cal.hal: electronic calibration
3. yYYYYmMMdDDpPP.diag.hal: detector diagnostics results
4. yYYYYmMMdDDpPP.noise-closed.hal: QDC and pedestal calibration
5. yYYYYmMMdDDpPP.noise-open.hal: sky-noise measurement
6. yYYYYmMMdDDpPP.yagclu-closed.hal: YAG laser PMT calibration (direct exposure)
7. yYYYYmMMdDDpPP.yagclu-open.hal: YAG laser PMT calibration including night-sky noise (direct exposure)
8. yYYYYmMMdDDpPP.yagmir-closed.hal: YAG laser PMT calibration (indirect exposure)
9. yYYYYmMMdDDpPP.yagmir-open.hal: YAG laser PMT calibration including night-sky noise (indirect exposure)

The *.pkt.hal* files contain runtime data, and the rest of the files contain calibration and diagnostics information. The number of *.pkt.hal* files generated on a given night depends on the duration of the run period for that night. For all the other files in the list, two of each are collected each night (if possible) one at the beginning and one at the end of the run. For the present analysis, the YAG laser data is not used. The *.diag.hal* files are used for diagnosing and monitoring the detector hardware.

The rest of the files above are used in the analysis as indicated in tables 7.2 and 7.3.

7.4 PASS0: Time Matching and Event Building

Event and time packets are received by the central data acquisition computer from the triggered mirrors and CT crate over the Ethernet. The order in which the packets are received and written to the raw data file depends on the condition of the traffic over the network. In general, the order packets are recorded, is not the same as the time order in which they were generated. The first stage of off-line processing is then to match and group the packets together to form *events.*

An event packet carries a time stamp that indicates the time from the beginning of the run (time of last global permit) of the mirror trigger. For the same trigger, a GPS time is recorded by the CT crate, and inserted into a time packet sent once per second to the DAQ computer. By comparing the times of the packets, each mirror event packet is matched with the corresponding timing packet. A multi-mirror event is formed if the matched event packets from each mirror occur within a time window of 100 μs of each other. Events thus formed are written out in a HRAW1 banks bounded by START and STOP banks. This function is performed by the *hma* program and a *.ps0.dst* file is generated.

7.5 PASS1: Event Calibration

During PASS1, *.ps0.dst* files are fed to the *hpass1* program. Raw TDC values are then converted to a time, in microseconds, corresponding to the tube trigger measured from the time of the mirror trigger (delayed by 50 μs). If more than one mirror are present in the event, the first mirror trigger time is used. This conversion uses gain and offset values obtained from the *.cal.hal* files by the *hca* program. Delays in the cables carrying the mirror triggers to the CT crate are also accounted for in this procedure.

Similarly, raw QDC values are converted to number of photo-electrons and stored in the HRAW1 bank. The gains used for this conversion are retrieved from the RXF calibration, and the offsets are obtained from the *.noise-closed.hal* files by the *hped* program.

CHAPTER 8

EVENT SELECTION AND RECONSTRUCTION

With the calibrated tube signals and trigger times in hand, the geometrical and profile reconstruction can proceed. Most of the events coming out of PASS1 are noise triggers. Therefore, a filter is applied first to select the candidate events.

In all, there are seven parameters that must be fit for in order to get an energy estimate for the shower: Four independent values are required to specify the geometry of the shower relative to the detector. Three other parameters enter into the G-H parameterization of the shower profile. A quick overview of the reconstruction procedure follows.

The shower geometry is reconstructed in two stages. First a Shower-Detector (SD) plane is formed between the shower axis and the detector origin. Within the SD plane the shower axis is uniquely determined by two parameters. The two additional parameters: the impact parameter, R_p, and the incline angle of the shower in the SD plane from the horizontal ψ. These parameters are illustrated in figure 8.1

Traditionally the monocular reconstruction procedure employed by the Fly's Eye group was carried out in three consecutive and independent steps:

1. Determination of the SD plane from the PMTs pointing directions.
2. Calculation of the track geometry in the SD plane using tube trigger times.
3. Determination of the shower energy and profile by fitting the tube signals, to a G-H form, assuming the geometry obtained from steps 1 and 2.

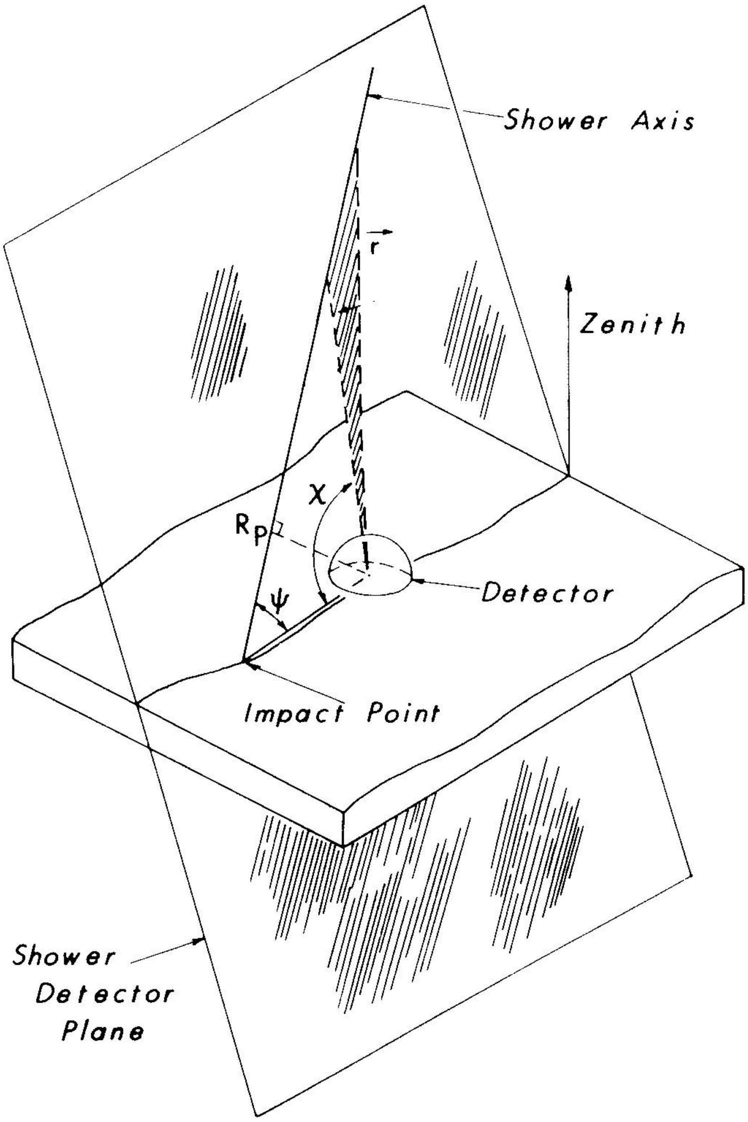

Figure 8.1. Shower geometry relative to detector.

The timing fit of the second step above suffers, in the case of BigH, from the limited angular coverage of the detector. The timing fit resolution is strongly dependent on the track-length of the observed track. In the HiRes-I prototype studies, reliable time fits are obtained only for showers spanning 40° or more. Most showers observed by BigH have track-lengths on the order of only 10°, too short to produce accurate results.

To get around the problem of short tracks, we investigated an alternative reconstruction technique. By imposing a constraint on the shape of the shower profile (i.e. restrictions on the values of the shower parameters) and performing a combined geometry/profile fit, we found that the track geometry, and the shower energy can be reconstructed with reasonably good resolutions. The restrictions on the profile parameters are based on our understanding of EAS development from previous measurements made by the Fly's Eye and the HiRes-I prototype.

In this chapter we discuss the event selection process and the reconstruction procedure used to determine shower geometries and energy. The geometry and energy resolution are described and later compared with stereo reconstruction results from the limited stereo data available since 1999.

8.1 PASS2: Rayleigh Filter

We start with a discussion of the Rayleigh filter used to reject most noise triggers. The mirror trigger condition implemented in hardware only requires coincidence between triggers in six tubes over two subclusters trigger. This condition is quite frequently met by fluctuations in the night sky and by other non-EAS sources such as flashers from airplanes. In general, the pattern of triggered tubes in such events is random or at least it is not "track-like". The Rayleigh filter is a fast and simple filter that looks at the temopral and spatial patterns of triggered tubes across the face of the cluster and compares them to a random walk.

8.1.1 Random Walk in 2d

A special case of the problem of a random walk in two dimensions can be stated as follows:

Let $\hat{r}_i$ be a random vector of unit length. Define $\vec{r}$ as the resultant vector of a sum of independent random unit vectors $\vec{r} = \sum_{i=0}^{N} \hat{r}_i$. It follows from statistics that the length of the vector $\vec{r}$ is distributed according to a *Rayleigh* probability density function:

$$p(r) = \frac{r}{\sigma^2} \exp\left\{-\frac{r^2}{2\sigma^2}\right\} \tag{8.1}$$

where $r = |\vec{r}|$. In our case $\sigma^2 = N/2$, where N is the number of steps. By definition, the probability of observing, after N step, a net displacement of magnitude $r > R$ is given by:

$$Prob\{r > R\} = \int_R^{\infty} p(r)dr = \exp\left\{-\frac{R^2}{2\sigma^2}\right\} \tag{8.2}$$

For a given vector of length R, this formula gives the probability that this vector is the result of a random walk process. A more convenient number to work with is the negative of the base-10 logarithm of this probability. Substituting for σ^2 we can write:

$$plog = \frac{R^2}{N ln 10} \tag{8.3}$$

A 1% probability that the vector is the result of a random walk corresponds to a *plog* value of 2. A 0.1% chance corresponds to $plog = 3$ and so on.

8.1.2 Application to HiRes

Triggered tubes in an event form a two dimensional spatial pattern across the face of the photo-multiplier tubes cluster. Events due to an EAS or other line sources will have a time progression that reflects the nature of the source. Random noise triggers, however, do not show any correlation between the tubes trigger times and the tubes positions in the cluster. The application of the Rayleigh filter to HiRes tubes is based on the above observation.

First, a time-ordered list of the triggered tubes is formed. A *step* of unit length is added from each triggered tube to all its *triggered* nearest neighbors that have a later time. Tubes without nearest neighbor triggers do not contribute. The steps are added up vectorialy and the resultant "vector" is calculated for all contributing pairs. The length of the resultant vector and the probability that the vector (event) is due to a random walk (noise trigger) is calculated. Events with $plog \geq 2.0$ are kept.

While the definition of nearest neighbor tubes is straightforward within a cluster, we must adopt a definition which also works between adjacent mirrors, in order to accomodate multi-mirror events. For this reason, we define nearest neighbors to be tubes whose viewing directions are within 1.5° (separation within a cluster is 1.0° between adjacent tubes).

The Rayleigh filter results in a significant reduction in the number of events in the data set. In the period from May 1997 to June 1999 some 52 million triggered events were collected. Only 2.3 million of these events passed the Rayleigh filter. Of these events that passed the filter the majority are tracks from the Xenon flashers and the YAG laser used for atmospheric monitoring. To separate EAS caused events from the flashers/laser events, the output of the Rayleigh filter program is written to three separate files designated as downward-going, horizontal, and upward-going according to the Rayleigh vector pointing direction.

The majority of EAS caused events find their way to the downward going files, but a few (less than 10%) end up in the horizontal files. In the following stages of the analysis we only look at the downward files and thus losing events in the horizontal files. This represents a small loss in aperture, however, this losss is included in the aperture calculation.

8.2 PASS3: Plane Fit

The first step in reconstructing the shower geometry is the identification of the SD plane. This is accomplished by noting that the triggered tubes pointing directions lie approximately in this plane. An event typically contains a few tubes triggered by noise in addition to those triggered by light from the EAS. The plane reconstruction uses an iterative procedure to identify and remove noise tubes from the event. Once the plane is identified, a track length can be calculated and used along with other parameters such as the inverse angular speed of the track to filter out noise events that passed through the Rayleigh filter.

8.2.1 Plane Fitting

Two simplifying assumptions are made for plane fitting: (a) The lateral extent of the shower is neglected, i.e. the shower is treated as a line source, and (b) the mirrors are assumed to lie at the origin, i.e. the physical spread of the mirror sheds around the detector origin is neglected.

Plane fitting is accomplished by minimizing a χ^2 function given by:

$$\chi^2 = \sum_i \frac{[(\hat{n} \cdot \hat{n}_i)]^2 \cdot w_i}{\sigma_i^2} \tag{8.4}$$

where the sum is over triggered tubes, $\hat{n}$ is the plane normal, $\hat{n}_i$ is the tube viewing direction vector and w_i is the number of photo-electrons seen by tube i, and an angular error of $\sigma = 1.0^o$ is assumed for all tubes. This error corresponds to the granularity of the detector optics. The tube signals are used in this fit as weighting terms and thus the name *amplitude weighted plane fit.* As an illustration, figure 8.2 shows the event display of an event, with the reconstructed plane shown as a line across the face of the cluster.

The resolution of the plane fit depends on several factors including the track-length and the signal to noise ratio for the tubes. Figure 8.3 shows the plane fit resolution for mono-energetic Monte Carlo events generated at several energies from $10^{18} - 10^{20}$ eV. Note that the resolution improves for the higher energy events, as the result of improving signal to noise ratio.

A typicall EAS event usually contains several noise-triggered tubes (referred to as bad tubes) in addition to those triggered by the EAS signal (refered to as good tubes). Figure 8.2 provides an illustrative example. An integral part of the plane fitting procedure is the identification and exclusion of bad tubes from the fit. As seen in the example, the noise tubes are easily identified because they are either spatially or temporally uncorrelated with the actual track, or both. The plane fitting routine takes advantage of this observation by implementing an iterative

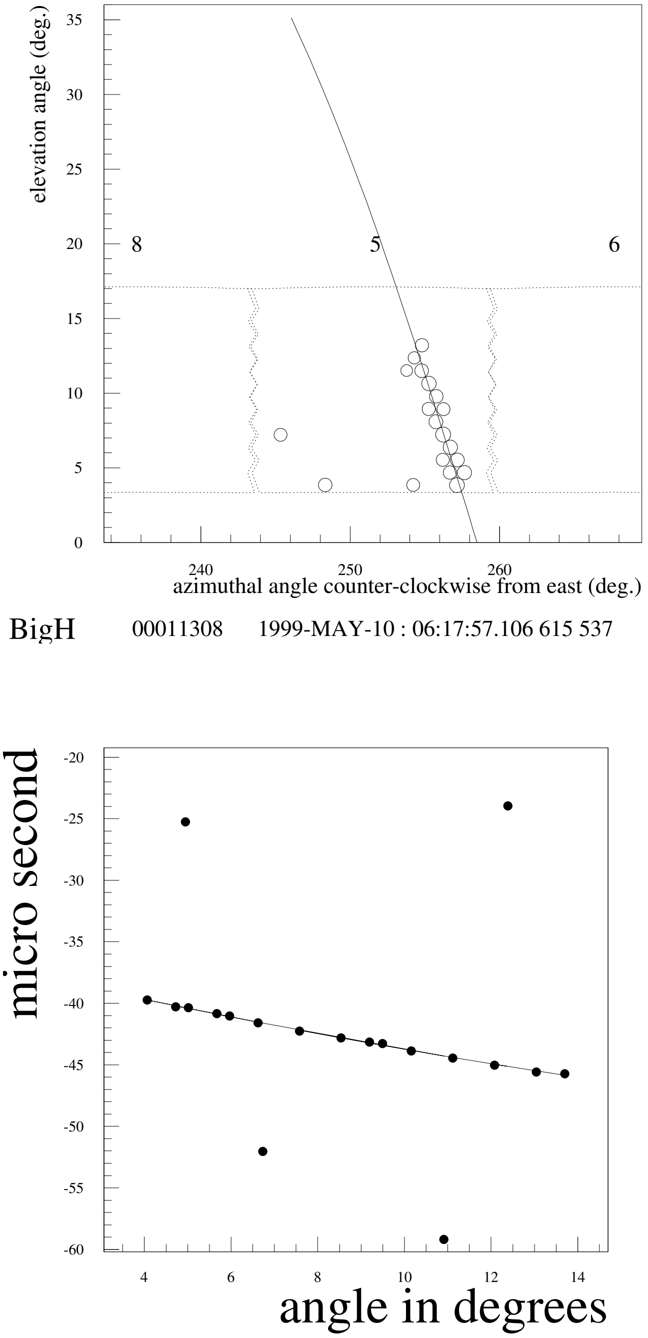

Figure 8.2. BigH Event Display showing an event with the reconstructed shower-detector plane. The angle in the lower plot is the tube “elevation angle” in the plane.

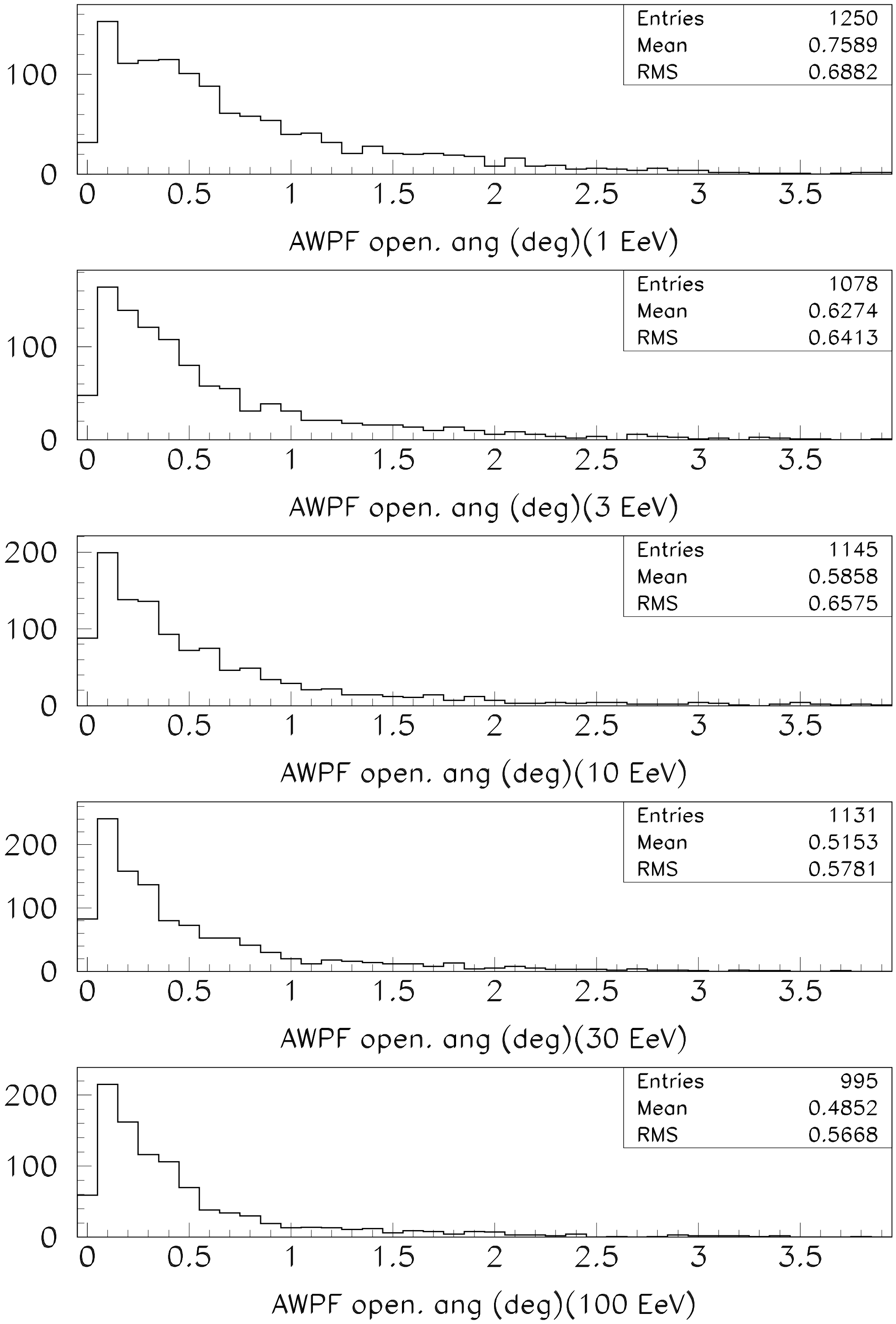

Figure 8.3. Results from amplitude weighted plane fit for five sets of mono-energetic Monte Carlo showers.

procedure where first, a subset of the triggered tubes is chosen by grouping tubes into clusters of “in-time” and nearest neighbors. An initial fit is performed using only tubes which belong to clusters of three or more. Assuming that the majority of the tubes in the event are good tubes and only a handful of bad tubes are present, the plane obtained from the initial subset can be expected to be a good approximation to the real plane, and can be used to reject tubes which lie too far from the plane. This process involves calculating a RMS deviation from the plane for those tubes included in the initial plane fit, and then rejecting tubes with an off-pane angle greater than five times the RMS deviation.

Timing is also used to reject bad tubes. A quadratic fit is made for the tube trigger times vs. χ_i, which is the angle the tube's projection in the plane subtends with the horizontal. The plane fit is then repeated for all the remaining tubes, and subsequently, more tubes are rejected if they have an off-plane angle or trigger times greater than three times the RMS values of the repeated plane and quadratic time fits. The procedure is iterrated until no further tubes are rejected or less than three remain. In the latter case, the fit is considered to have failed and the event is rejected.

8.2.2 Event Filtering

Most noise events which remain after PASS2 are rejected by the iterative plane/time fit. We also reject EAS events which are too close to the detector, or are too dim , or have a very short track-length. Together with the plane fit, these criteria constitute an additional filtering pass. These criteria are listed below:

plane fit failure: If the iteration procedure described above fails, that is, if tubes are flagged as bad until less than 3 tubes remain in the event then the event fails and is rejected.

track-length cut A minimum track-length of 6° is required for an event to pass. This cut is made because the quality of the trajectory reconstruction becomes seriously degraded with shorter track-lengths.

brightness cut After all noise tubes are identified and removed from the event, the average number of photons seen by good tubes in the event is calculated. This cut is meant to reject coherent electronic noise triggers and low energy events. The minimum accepted value is 75 photons. This value is too small to cause any loss of interesting events. As a matter of fact, in PASS3b (see below) a similar cut is made but with a minimum value of about 200.

track width cut broad tracks are rejected as noise, spurious sources (e.g. airplane flasher), Cerenkov "blasts", or near-by low energy events. An rms value of 1° is the maximum allowed value.

angular speed cut Close-by showers cross the mirror with higher angular speed than distant showers. A maximum angular speed of 5.73 deg/μs , corresponding to a track perpendicular to the mirror axis at a distance of 3 km, is accepted.

8.2.3 More Filtering: PASS3a and PASS3b

The Rayleigh filter and the cuts applied in PASS3 remove most noise events. An additional "correlation cut" is used to reject all remaining noise triggers. We use here the standard correlation coefficient between two sets of variables x and y defined by $\rho(x, y) = Cov(x, y)/(\sigma_x \sigma_y)$. We calculate the correlation coefficient between the tube trigger times and the χ_i angle in the plane, as shown in figure 8.2. Although it is not based on a statistically rigorous test, it is efficient in rejecting bad events and keeping good ones. When applied to MC events, fewer than #% of the events are rejected. The correlation cut is implemented as PASS3a within the data processing chain.

Two of the cuts implemented in PASS3 discussed above are "tightened" in a separate pass referred to as PASS3b. This pass is applied to the data to reject close-by low energy events. The BigH detector only covers 17° in elevation. This implies that, for nearby showers, only the falling edge of the shower development is observed. This "poor" measurement leads to poor reconstruction.

Event reconstruction also requires that the tube signals be large enough such that the EAS contribution to the light collected by a PMT is not dominated by noise. Values for the two cuts implemented in PASS3b are:

angular speed cut lowered to 3.33 deg/μs. This is equivalent to a track 5 km away and perpendicular to the mirror axis.

brightness cut increased to 200 photons (55 photo-electrons).

8.3 PASS4: Profile Const. Geom. Fit

An initial Monte Carlo study to investigate the reconstructability of EAS events collected by a one ring HiRes detector concluded that the time fit performed poorly in reconstructing the shower geometry. In many cases the impact parameter R_p is underestimated by a as much as 75 %, and the energy resolution suffers accordingly. After that study, the profile constrained geometry fit (PCGF) was proposed as an alternative to a separate time and profile fits. We have adopted a modified version of the PCGF for the analysis of BigH data. In the original proposal one shower shape (one set of profile parameters) was allowed, the values of these parameters were chosen so that the fit will work best at energies around 10^{20} eV. In the current implementation we perform a number of independent PCGFs with different profile parameters chosen to represent *average* proton showers with varying energies greater than 10^{18} eV. From these, the fit which minimizes a combined timing and profile χ^2 function is then chosen as the best fit. Our approach compared to the original amounts to relaxing the constraint on the shower profile shape used in the fit. This improves the reconstruction results at lower energies ($\sim 5\times10^{18}$ eV) and it performs just as well at 10^{20} eV.

In order to describe the PCGF procedure, it is neccesary and useful first to look at the separate time and profile fits. These will be described in the next two subsection, follwed by the presentaion of the PCGF implementaion.

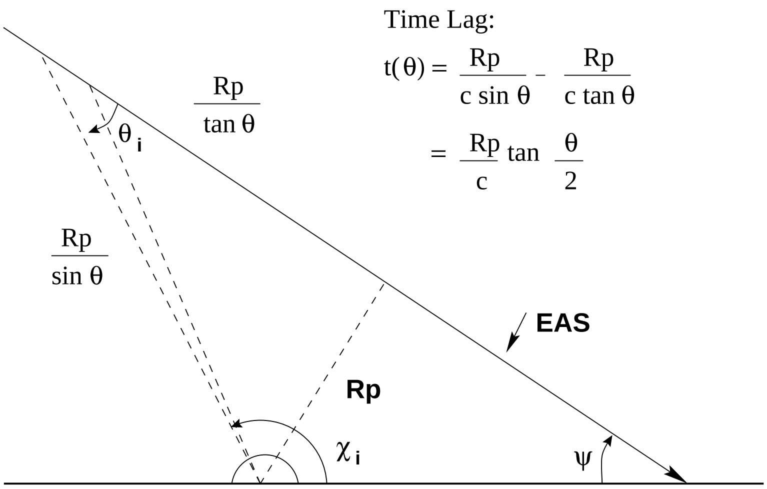

Figure 8.4. Track geometry in the Shower-Detector plane.

8.3.1 Stand-Alone Timing Fit

The original Fly's Eye detector relied on timing to reconstruct the shower geometry[35]. Figure 8.4 illustrates the track geometry within the S-D plane. If we assume that tube trigger times are a good meausre of the tube crossing times, then we obtain the following relation between the tube trigger times, t_i, to the tube viewing angles, χ_i:

$$t_i = t_0 + \frac{R_p}{c} \tan\left(\frac{\pi - \psi - \chi_i}{2}\right) \tag{8.5}$$

where t_0 is the time at which the shower passes the point of closest approach, ψ the incline angle of the track, and R_p the impact parameter as shown in figure 8.4. Note that the tube's viewing angle χ_i and the light emission angle θ_i are related by $\theta_i = \pi - \psi - \chi_i$.

The timing fit is obtained by minimizing a χ^2 function of the form:

$$\chi^2_{tim} = \sum_i \frac{1}{\sigma_i^2} \left\{ t_i - \left(t_0 + \frac{R_p}{c} \tan\left(\frac{\pi - \psi - \chi_i}{2}\right)\right)\right\}^2 \tag{8.6}$$

An error of $\sigma_i = (500/\sqrt{S_i})$ ns is used, where S_i is the tube signal in photoelectrons. It is difficult to obtain an accurate estimate of σ_i. The form used reflects the fact that the larger the signal amplitude the less the expected difference between crossing and trigger times. With this simplified treatment of errors, it is not possible to obtain a $\chi^2/dof \sim 1$ at minimum [7]. The errors are scaled such that, the χ^2 minimum over the parameter space assumes a value of $\chi^2/dof = 1$.

The problem with the time fit is that it requires tracks with sufficiently long tracklengths to resolve the tangent function. Over a small angular range, the $t(\chi_i)$ relation is almost linear (as can be seen from figure 8.2). It can be seen from equation 8.5, however, that there are three independent parameters in the fit. An estimate of the error in the reconstructed geometry parameters as a function of the observed shower tracklength was obtained by Kidd [24]. He showed that the $\sigma_{R_P} \sim 1/L^{5/2}$ with a similar relation for σ_ψ , where L is the tracklength in degrees. Kidd studied data observed by the HiRes-I prototype detector in coincidence with the CASA-MIA detectors. Even with the help of the MIA muon detector timing information, only tracks with $L \geq 15^\circ$ were considered. A separate analysis of the monocular prototype data was also carried out [40]. In that analysis the restriction $L \geq 40^\circ$ was made. In contrast, the vast majority of the BigH events have tracklengths of less than 15°.

8.3.2 Stand-Alone Profile Fit

For a given track geometry, the shower profile fit is done by comparing the observed tube signals with tube signals calculated based on a trial set of shower parameters. The χ^2 function is given by:

$$\chi^2_{pfl} = \sum_i \frac{1}{\sigma_i^2}(S_i^{(m)} - S_i^{(p)})^2 \tag{8.7}$$

where the sum is over triggered tubes, $S_i^{(m)}$ is the measured tube signal in photoelectrons, $S_i^{(p)}$ is the predicted tube signal, and $\sigma_i^2 = S_i^{(m)} + 200$. The σ_i^2 terms are obtained by adding in quadrature the Poisson fluctuation in the signal ($\sqrt{S^{(m)}}$) and the sky background fluctuations. The particular value 200, is the expected variance of the number of sky noise pe in the 5.6 μs integration window, which was measured in situ at Dugway Proving Grounds. The predicted tube signals calculation proceeds following the prescription of chapter **??**. All physical processes, shower and detector details simulated in the Monte Carlo are taken into account in the reconstruction.

In general, the profile χ^2 is minimized with respect to the G-H shower profile parameters (x_0, x_{max}, and N_{max}). In the context of the PCGF, the parameter x_0 is fixed to $x_0 = 40\,\mathrm{gm\,cm^{-2}}$. This is done to make the problem more manageable, since multi-parameter fits are difficult in general. The value used for x_0 is representative of an average over proton and iron showers. The effect of fixing x_0 is investigated by looking at reconstructed MC showers, section 8.3.4.

8.3.3 PCGF: Reconstruction Procedure

The shower energy reconstruction is accomplished in two steps: First, a set of six independent PCGFs are performed and the results from each fit stored. Second, in a separate step, the optimal fit is chosen from this set (see page 82). A number of quality cuts are then imposed on the reconstructed shower from the optimal fit, and only those that pass the quality cuts are considered successfully reconstructed. In this section, we discuss the implementaion of the independent PCGFs first, and then the procedure of choosing the optimal fit, and the quality cuts are presented.

The six PCGFs differ only in the value of x_{max} used in each fit. In each fit, x_{max} is fixed to one of: 685.0, 720.0, 755.0, 790.0, 825.0, or 860.0 $\mathrm{gm\,cm^{-2}}$, and not allowed to vary during the fit. A 10^{18} eV proton shower has an average x_{max} of 725.0 gm $\mathrm{cm^{-2}}$, and a 10^{20} eV proton shower has an average x_{max} of 835.0 $\mathrm{gm\,cm^{-2}}$ based on shower Monte Carlo results. The range of x_{max} values used in the reconstruction is chosen with these numbers in mind.

Each fit minimizes the profile χ^2 function (χ^2_{pfl}) over the parameter space. Seven parameters completely specify the shower geometry and profile. Of these, the profile parameters x_0 and x_{max} are fixed, and the geometry parameters R_p and ψ are related by the timing equation (8.5). In the χ^2_{pfl} minimization procedure, this relation is used to *calculate* R_p for a given ψ thus reducing the number of free parameters by one.

The search over ψ is initially carried out in the shower-detector plane calculated in PASS3 and used as input for the PCGF. The angle ψ is restricted to the range

$(0, 180^o)$. . This makes a search over ψ simple, since 1^o steps can be taken over the allowed range of values which ψ can assume ,and a rough map of the χ^2 space constructed. The point of minimum χ^2 found in the rough search can then be used as a starting point for a more refined search using a specialized minimization routine, as discussed below.

The profile χ^2 is linear in N_{max}, the shower size at maximum development, and so N_{max} is uniquely determined for any trial shower when all the other parameters have been specified. A trial shower of "unit size" is used during the search. This shower results in predicted tube signals which are then scaled up or down by a constant factor to minimize χ^2_{pfl}. This scaling factor determines N_{max}. Finally, the shower energy is obtained according to the formulae given in section 6.1.

The "rough" search over ψ supplies us with an inital guess for the actual minimum point. A refined search is now done in the neighborhood of this initial point. The refined search is performed by the *amoeba* minimization routine, which implements the downhill simplex method. In this search, the the SD plane normal is allowed to change and finer steps in ψ are taken.

The predicted tube signals are strongly dependent on the lateral displacement of the tubes from the SD plane. This can be seen in figure 6.8 which shows ray tracing results of point sources at various angles to the tube center. The search over the SD plane normal, $\hat{n}$, is done in terms of a parameterization using the input plane normal, $\hat{n}_0$ and two other parameters, α and β, defined by the relation: $\hat{n} = \text{normalized}\left(\hat{n}_0 + \alpha\hat{c}_0 + \beta(\hat{n}_0 \times \hat{c}_0)\right)$ where $\hat{c}_0$ is the tube centroid vector $\hat{c} = \sum_i w_i\hat{n}_i / \sum_i w_i$ projected into $\hat{n}_0$. w_i are the tube signals and n_i the tube pointing vectors. The parameters α and β represent deviations from the initial guess, they are allowed to vary in a constrained range only so that the minimization routine does not stray too far from the initial plane.

Results from the six independent fit are written to file. The choice of the optimal fit is now made from these fits according to which fit minimizes a combined $\chi^2_{com} = \chi^2_{pfl} + \chi^2_{tim}$ function. Two points should be mentioned with respect to combining the χ^2 functions: First, the individual PCGFs search the geometry and

N_{max} space (recall that x_{max} as well as x_0 are fixed in each PCGF) for a minimum of χ^2_{pfl}, i.e. no attempt is made to minimize the combined χ^2 function within the individual fits. Second, as mentioned in section 8.3.1, the absolute values of the timing χ^2 is not meaningful. The same applies, although to a lesser degree, to the profile χ^2. Because of this, the two χ^2 functions are each normalized to 1/d.o.f by scaling their respective σ^2, before they are combined. This procedure is not rigourus, however, it allows us to combine the two χ^2 functions with equal weight given to each function. From Monte Carlo studies, it is observed that this procedure gives slightly better results than simply relying on the profile χ^2 alone.

A set of quality cuts was identified through the examination of the reconstruction results for MC generated showers. These cuts are applied to the reconstructed events and only those events that pass the cuts are considered successful. Events (real and Monte Carlo) are rejected if they satisfy any of the following conditions:

1. Cerenkov light contribution to the observed flux is greater than 20% for more than two bins.
2. Tracklength less than 7.9 degrees.
3. Depth of first observed point along the track greater than $1200\,\mathrm{gm\,cm^{-2}}$.
4. The best profile χ^2 value is greater than 14.0 per d.o.f.

8.3.4 PCGF Monte Carlo Resolution Study

Monte Carlo showers were reconstructed to study the resolution and systematics of the PCGF reconstruction. These showers were generated using the detector Monte Carlo (section 6.1) and processed through all stages of the reconstruction procedure starting at PASS2. Where applicable, the processing of the MC data uses the same programs as were used on real data.

Two types of events were considered, mono-energetic proton showers and mixed proton-iron showers generated according to the Fly's Eye stereo (2-component) spectrum [1]. The same set of quality cuts was applied to the reconstructed events.

The resulting resolutions for the various shower parameters are shown in figures 8.5 through 8.8.

It can be seen from the plots, that the resolutions for R_p, ψ, and energy degrade at lower energies but are acceptable above 10^{19} eV. The improvement with energy is due mainly to the fact that higher energy events are observed at greater distances and so a larger fraction of the shower development is seen. The signal to noise ratio also improves with energy. The attempt to improve on the amplitude weighted plane fit yields good results at high energies but results in worse fits at lower energies as illustrated by figures 8.9 and 8.10.

The set of MC showers generated with a 2-component spectrum is representative of the actual flux seen by BigH. It also show the difference in resolution that can be expected between proton and iron showers. On average, iron showers develop with shallower x_{max} than proton showers. Fluctuations in x_{max} are also smaller for iron showers. The effect on the reconstructed energies, of the different x_{max} distributions can be seen in figures 8.11 through 8.13.

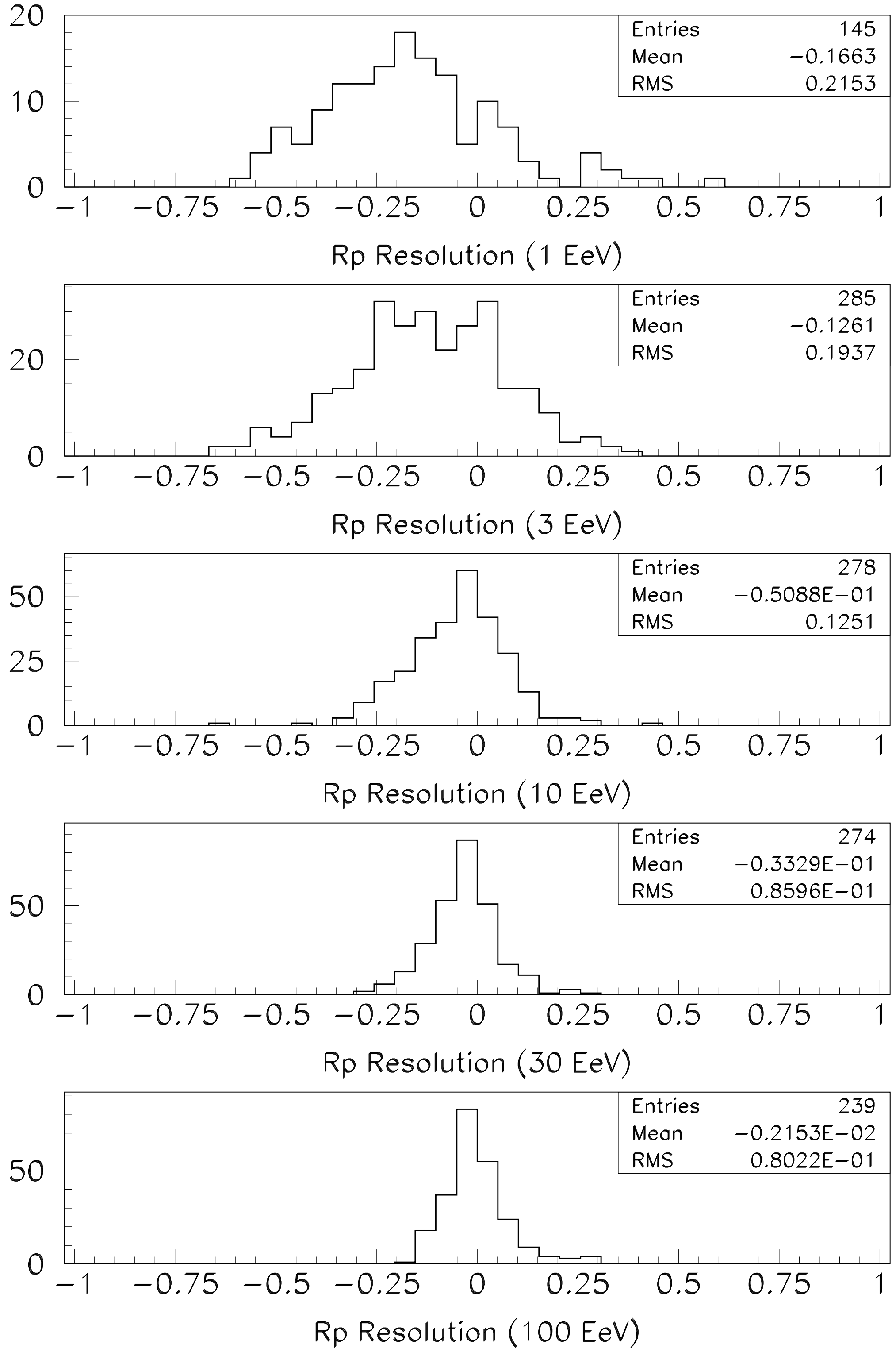

Figure 8.5. R_p resolution: $(R_{p_{out}} - R_{p_{in}})/R_{p_{in}}$

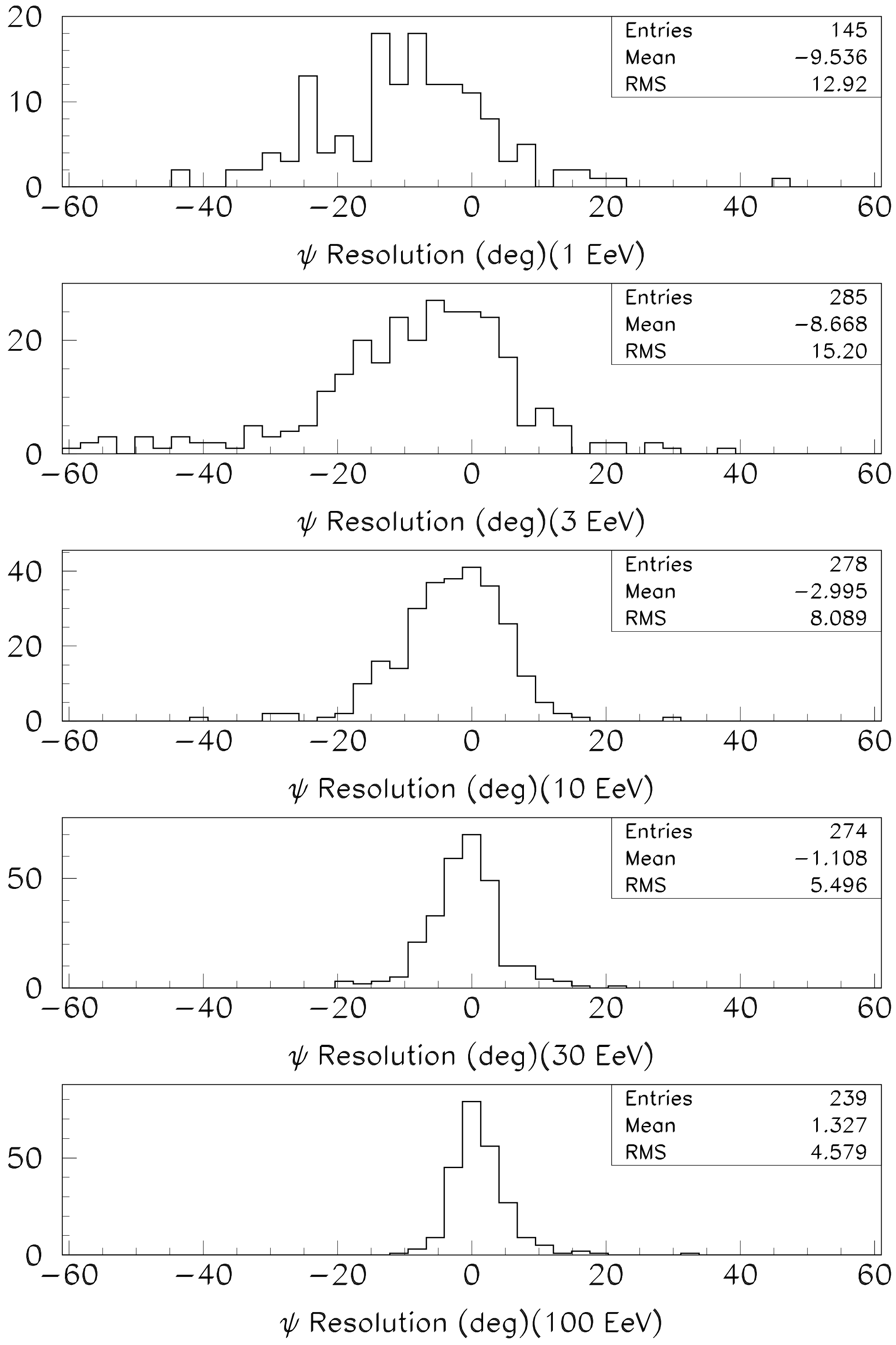

Figure 8.6. ψ resolution: $\psi_{out} - \psi_{in}$

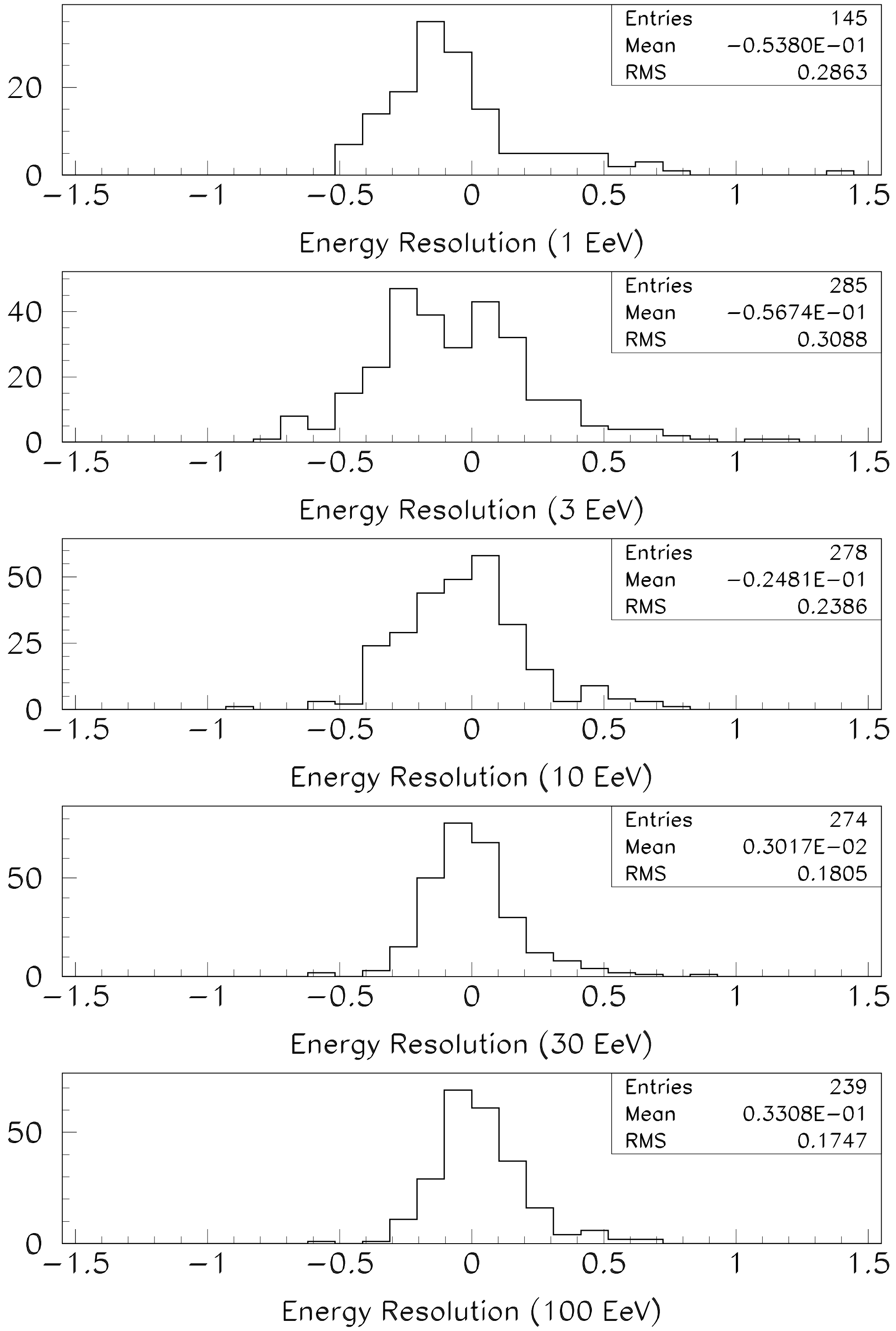

Figure 8.7. Energy resolution: $(E_{out} - E_{in})/E_{in}$

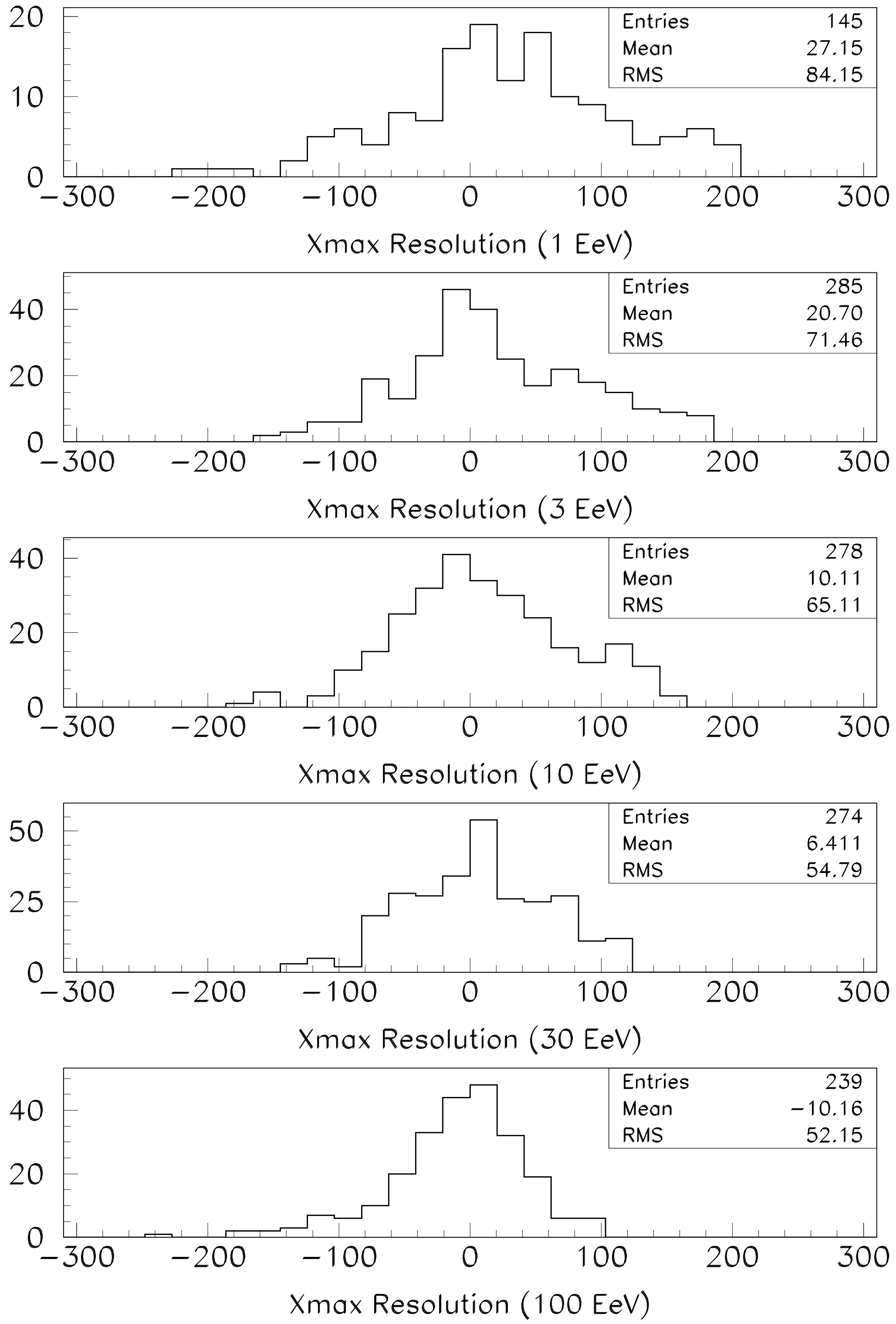

Figure 8.8. x_{max} resolution: $(x_{max_{out}} - x_{max_{in}})$

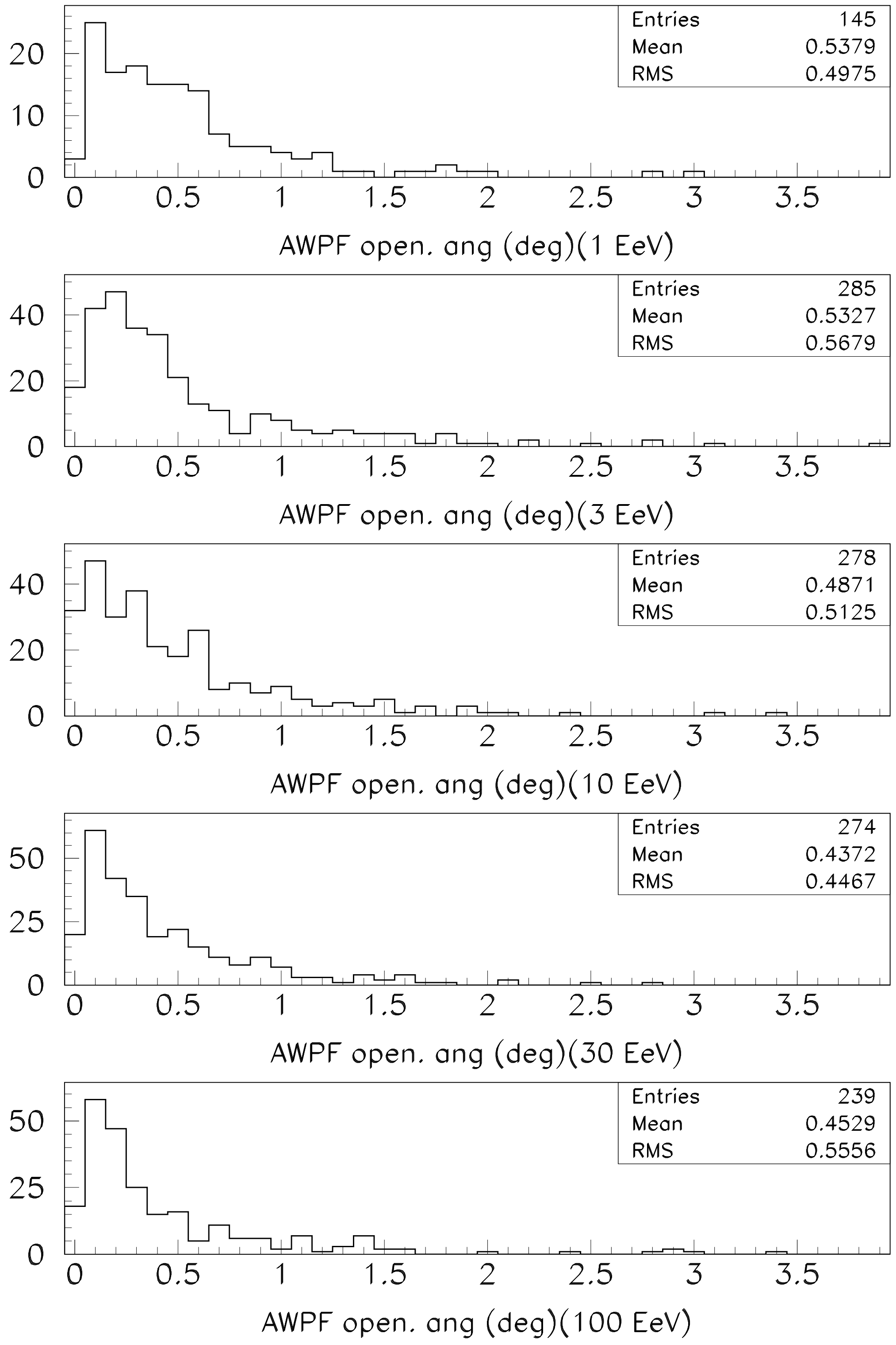

Figure 8.9. Amplitude weighted plane fit, used as input to the profile constrained geometry fit. The plot shows the opening angle between the MC and reconstructed planes.

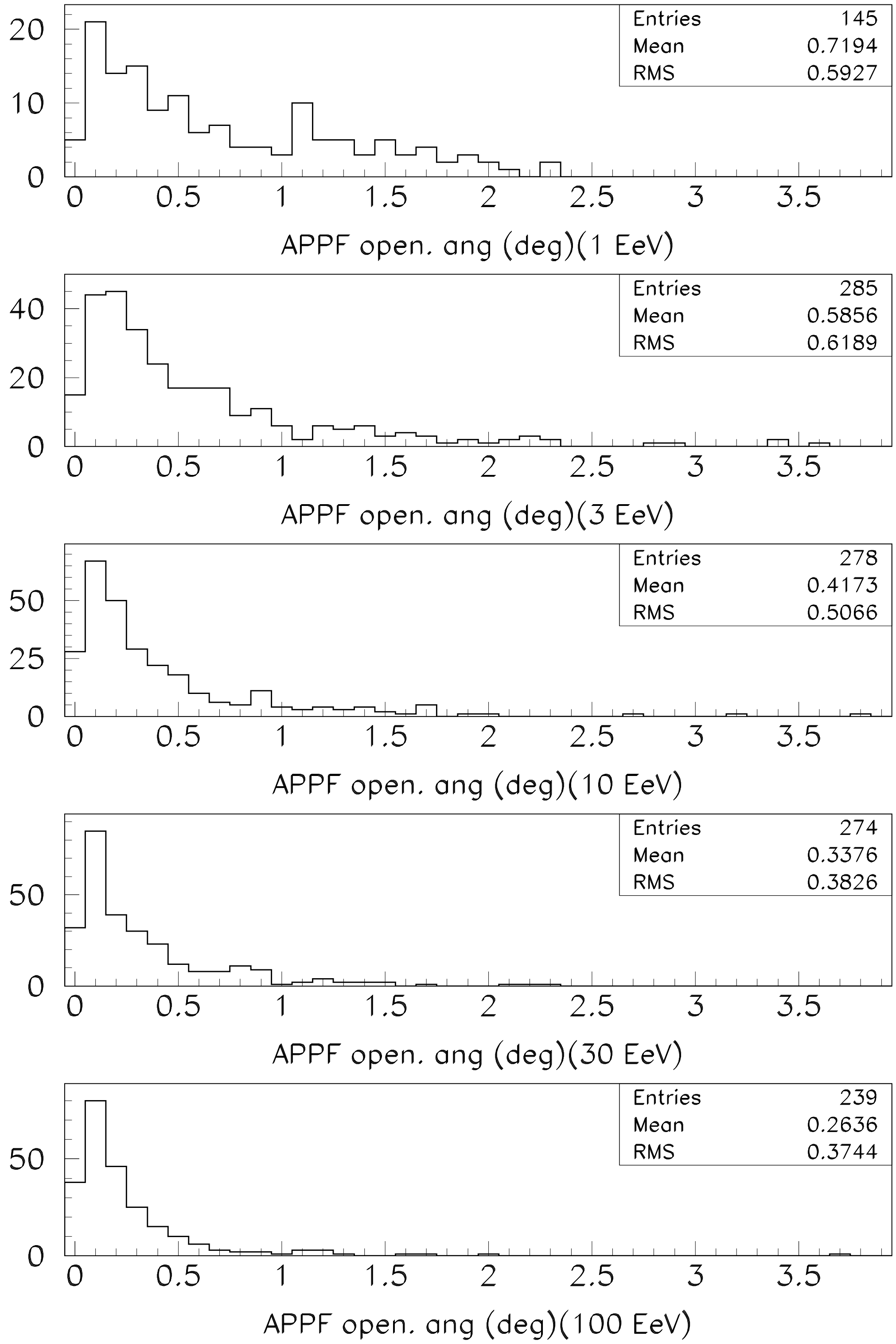

Figure 8.10. Amplitude predicted plane fit, calculated by the profile constrained geometry fit. The plot shows the opening angle between the MC and reconstructed planes.

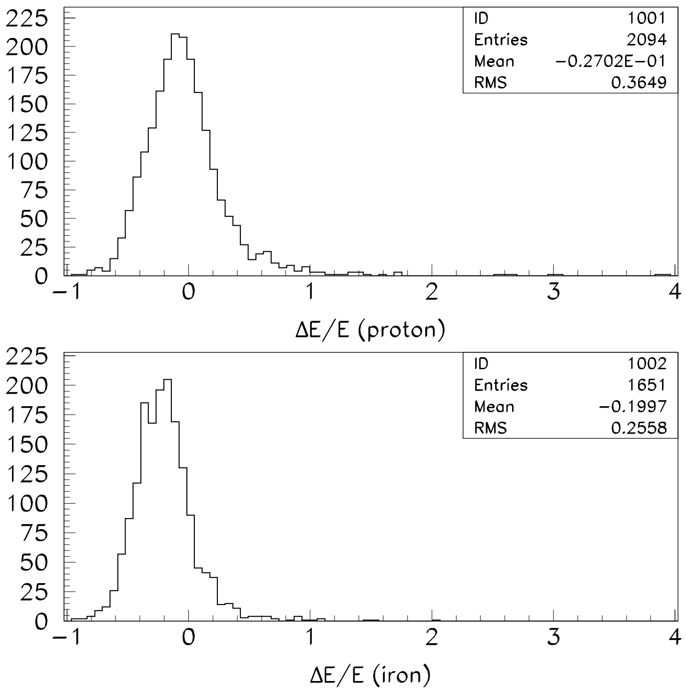

Figure 8.11. Energy resolution for a set MC showers generated according to the Fly's Eye 2-component spectrum. Proton and iron showers shown separately.

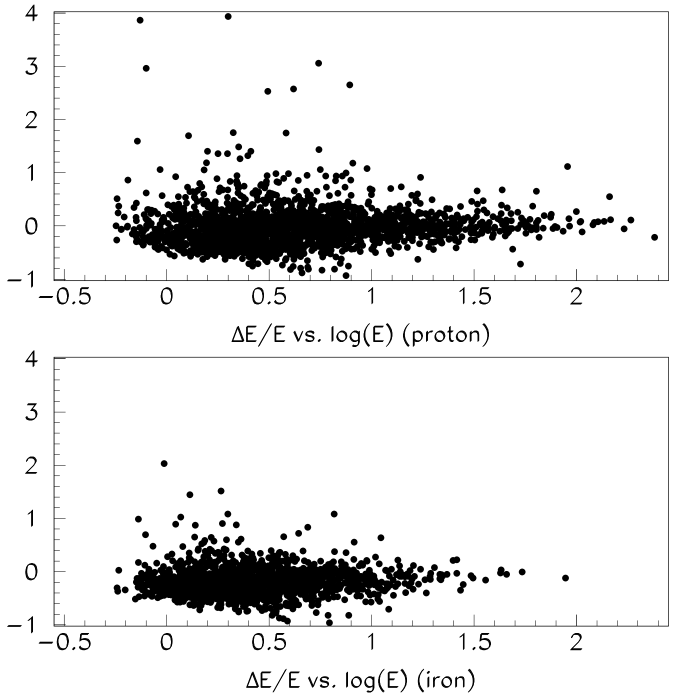

Figure 8.12. Scatter plot of energy resolution versus energy for proton and iron showers.

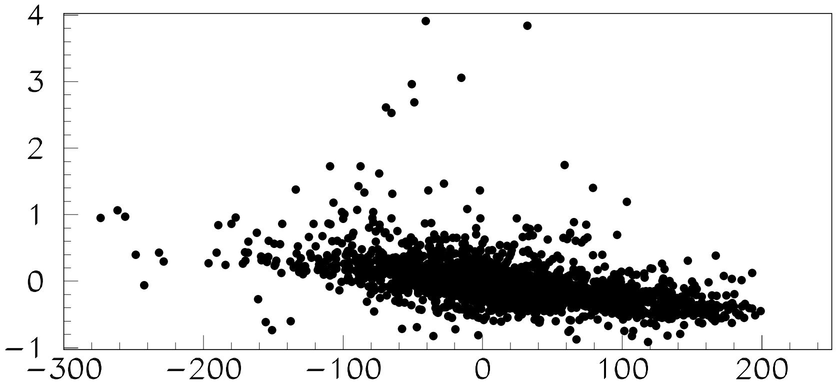

ΔE/E vs. ΔXmax (proton)

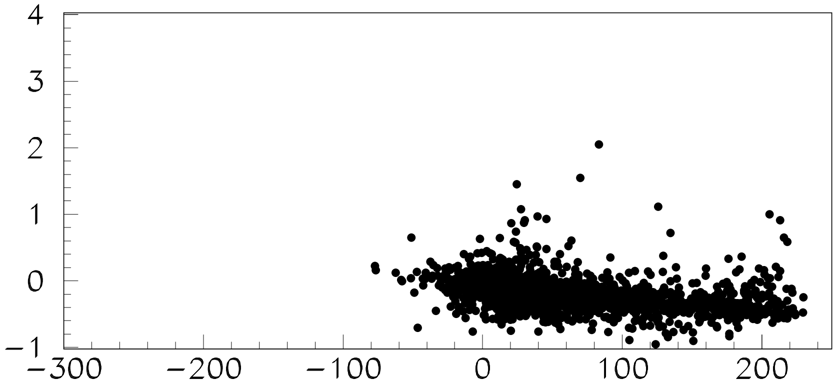

ΔE/E vs. ΔXmax (iron)

Figure 8.13. Scatter plot of energy resolution versus error in x_{max} for proton and iron showers.

CHAPTER 9

SPECTRUM MEASUREMENT

In this final chapter, I summarize the results of the UHE cosmic rays spectrum measurement. The chapter begins with a brief explanation of the calculation used to derive the energy spectrum and then proceeds to a discussion of the detector aperture and exposure calculations. The data set used is summarized, and, the measured flux is shown next followed by a discussion of the results. Events observed above the GZK cutoff are examined at the end of the chapter.

9.1 Energy Spectrum Measurement

The goal of the spectrum measurement is the determination of the differential flux, $j(E)$ $[\mathrm{m}^{-2}\,\mathrm{sr}^{-1}\,\mathrm{s}^{-1}\,\mathrm{eV}^{-1}]$, representing the number of particles observed per unit area, per unit time, and per unit energy. Consider a detector with an energy dependent aperture ($Area \times Solid\,angle$) of $A\Omega(E)$ $[\mathrm{m}^2\,\mathrm{sr}]$, and let the detector collect data for a total time T [s] . Observed events are reconstructed to obtain an estimate of the CR energy and then these events are divided among energy bins $(E_i - \Delta E/2, E_i + \Delta E/2)$ centered at energies E_i. If the energy reconstruction was without error then the number of events in a given energy bin, ΔN_i , would be given by:

$$\Delta N_i = T \times \int_{E_i - \Delta E/2}^{E_i + \Delta E/2} dE\, j(E) A\Omega(E) \tag{9.1}$$

For small bin sizes, this can be approximated by

$$\Delta N_i \approx T j(E_i) A\Omega(E_i) \Delta E \tag{9.2}$$

And the flux at energy E_i can be calculated using:

$$j(E_i) \approx \frac{\Delta N_i}{TA\Omega(E_i)\Delta E} \tag{9.3}$$

Equation 9.3 is the basic relation used to obtain the spectrum measurement.

9.2 Detector Exposure

Exposure is defined as the product of the aperture and the total run time. At the time of this writing, BigH has the largest accumulated exposure of any detector in the energy region of interest. The data was collected over a period of two years for a total on-time of $\sim 950\,hrs$. The estimated reconstructible aperture grows with energy to reach a value $\sim 6000 km^2 sr$ at $10^{20} eV$. With this exposure we expect to see several events above the GZK cutoff if the flux continues. The aperture and on-time calculations are given below.

9.2.1 Detector Aperture

The detector aperture is calculated using the detector Monte Carlo. A set of Monte Carlo events is generated in an artificial aperture of:

$$A_0\Omega_0 = 2\pi^2(R_{p_{max}}^2 - R_{p_{min}}^2)(1 - \cos\theta_{max}) \tag{9.4}$$

The choice of minimum and maximum values for the parameters in the equation is made such that the artificial aperture is large enough to contain all events that would be expected to trigger the detector. For this analysis we used $\theta_{max} = \pi/2$ is used throughout and different values for $R_{p_{min}}$, and $R_{p_{max}}$ depending on the energy of the simulated events (see table 9.1).

The trigger aperture at the energy of interest is given by an equation of the form:

$$A\Omega = A_0\Omega_0 \times \frac{\#\,triggered\,events}{\#\,generated\,events} \tag{9.5}$$

At each stage of the reconstruction a similar equation holds, i.e. the ratio of successfully reconstructed events to the input events gives the factor by which the aperture is modified at that stage of the reconstruction. The reconstructible aperture is then

Table 9.1. Volume at each Monte Carlo energy, mono-energetic proton showers. $\theta_{max} = \pi/2$ for all sets. Sets with $R_{p_{min}} = 2.0km$ were generated with less than optimal values for $R_{p_{max}}$. These sets were used nevertheless since they still contain the required information.

Energy (eV)	$R_{p_{min}}(km)$	$R_{p_{max}}(km)$	$A_0\Omega_0(km^2sr)$
1.6×10^{17}	2.0	20.0	7817.
3.0×10^{17}	1.0	10.0	1954.
5.0×10^{17}	2.0	30.0	17686.
1.0×10^{18}	1.0	15.0	4422.
1.6×10^{18}	2.0	40.0	31504.
3.0×10^{18}	1.0	20.0	7876.
5.0×10^{18}	2.0	50.0	49269.
1.0×10^{19}	1.0	30.0	17746.
3.0×10^{19}	1.0	40.0	31527.
1.0×10^{20}	1.0	50.0	49328.

Table 9.2. Number of Monte Carlo events (mono-energetic proton showers) at each stage of the reconstruction.

Energy (eV)	# gen.	# trig.	# ps2d	# ps3d	# ps3ad	# ps3b
1.6×10^{17}	8000	124	93	18	14	0
3.0×10^{17}	8000	1202	1027	292	236	0
5.0×10^{17}	8000	223	198	106	98	3
1.0×10^{18}	4000	1893	1771	1285	1250	167
1.6×10^{18}	4000	197	186	153	150	44
3.0×10^{18}	4000	1352	1258	1085	1078	645
5.0×10^{18}	4000	327	302	282	282	216
1.0×10^{19}	4000	1399	1284	1149	1145	1011
3.0×10^{19}	4000	1421	1305	1134	1131	1065
1.0×10^{20}	4000	1312	1180	999	995	960

obtained by looking at the results from the last step in the reconstruction (in our case PASS4) and its associated quality cuts.

From the numbers in table 9.2 we calculate the aperture at each stage of data processing according to equation 9.5. The calculated apertures through PASS3b are shown in figure 9.1.

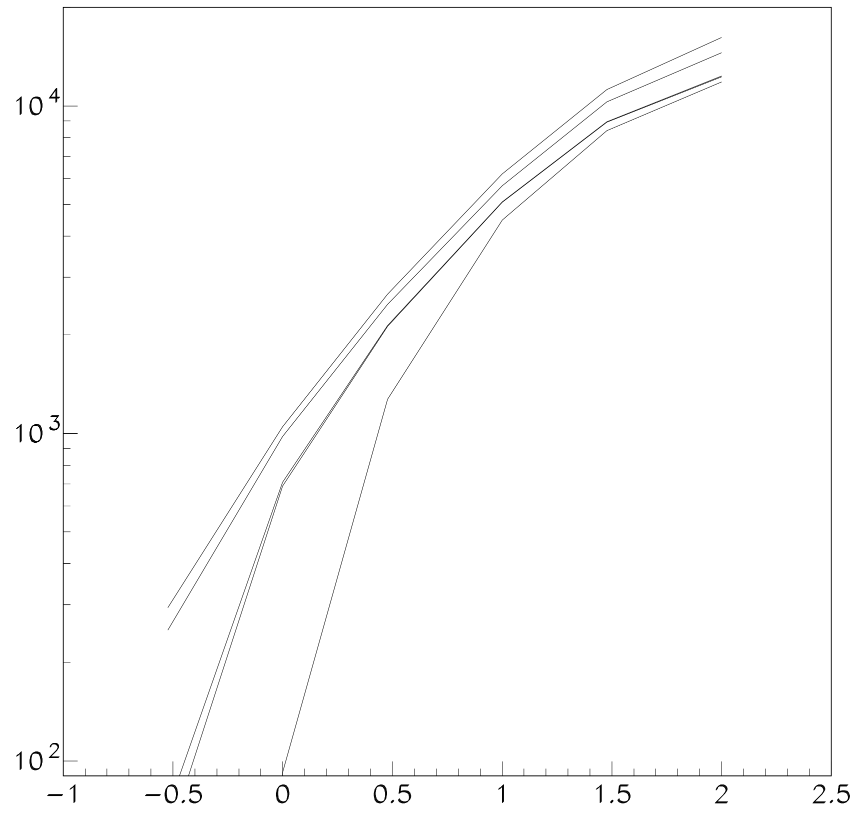

Figure 9.1. Detector Aperture at each stage of processing through PASS3b. From the top curve, these are: trigger aperture, aperture @ PASS2, 3, 3a, and 3b.

Table 9.3. Reconstructible aperture for each energy bin, based on Monte Carlo sets of mono-energetic proton showers.

$\log_{10}(E\,\text{EeV})$	aperture (km^2sr)	$\log_{10}(E\,\text{EeV})$	aperture (km^2sr)
0.05	139.2	1.35	6080.9
0.15	257.5	1.45	6615.2
0.25	465.5	1.55	7123.1
0.35	758.6	1.65	7605.1
0.45	1051.7	1.75	8061.5
0.55	1516.6	1.85	8492.4
0.65	2045.5	1.95	8898.3
0.75	2574.4	2.05	9279.3
0.85	3103.2	2.15	9635.7
0.95	3632.1	2.25	9967.9
1.05	4318.1	2.35	10276.2
1.15	4932.7	2.45	10560.7
1.25	5520.2	2.55	10821.7

At each energy greater than or equal to $10^{18}eV$, 300 events which were successfully reconstructed through PASS3b were then processed through PASS4 (htim_pfl and its associated cuts). A reconstructible aperture is thus obtained at each of these energies. Interpolation was then used to get the aperture at each energy bin.

Energy bins are logarithmic in energy with a width of 0.1, also energy is measured in EeV, so that $\log_{10}(E) = 0.0$ corresponds to an energy of $E = 10^{18}\,\text{eV}$. Table 9.3 gives the aperture at each energy bin.

9.2.2 Detector Aperture: Composition dependence

The detector aperture calculation presented in the previous section is based on sets of Monte Carlo proton showers. The reconstructible aperture may not be the same for proton and iron showers though because of the their different x_{max} distributions. On average, iron showers develop higher in the atmosphere than proton showers with the same energy. For close-by showers, this may have an effect on the detector trigger efficiency because of the small elevation angle coverage of the one-ring configuration of the detector mirrors. Even iron showers which do trigger are more likely to fail the reconstruction because only the falling edge of the shower

Table 9.4. Reconstructible aperture for each energy bin, corrected for composition dependence.

$\log_{10}(E\,\mathrm{EeV})$	aperture (km^2sr)	$\log_{10}(E\,\mathrm{EeV})$	aperture (km^2sr)
0.05	94.6	1.35	6080.9
0.15	213.6	1.45	6615.2
0.25	395.9	1.55	7123.1
0.35	621.4	1.65	7605.1
0.45	951.4	1.75	8061.5
0.55	1317.6	1.85	8492.4
0.65	1826.4	1.95	8898.3
0.75	2556.4	2.05	9279.3
0.85	3103.2	2.15	9635.7
0.95	3632.1	2.25	9967.9
1.05	4318.1	2.35	10276.2
1.15	4932.7	2.45	10560.7
1.25	5520.2	2.55	10821.7

profile is seen by the detector.

To calculate an aperture for a combined proton-iron flux, a composition must be assumed. As discussed in section 8.3.4, a Monte Carlo set based on the Fly's Eye 2-component spectrum was generated and reconstructed. The detector aperture can be calculated based on this set instead of the mono-energetic sets. A complication arises though because of the low statistics at higher energies. Events were generated following falling energy spectra and thus fewer events were produced at higher energies.

According to the Fly's Eye 2-component model, cosmic rays above 10^{19} eV are predominantly protons. Assuming this to be correct, the aperture calculated based on the mono-energetic proton showers still holds at above 10^{19} eV, and the calculation needs modification at lower energies only. The aperture was calculated at each energy bin using the 2-component set and compared with the numbers presented in the previous section. The two calculations were combined to get a corrected value. The final values of the aperture at each energy bin is shown in table 9.4. Note that only bins with $\log_{10}(E) < 0.8$ are changed.

9.2.3 Detector On-time

Detector On-time was calculated based on the time the mirror triggers were permitted. For each month, the number of minutes the mirror triggers were permitted are tallied up by the *ontime* program for each active mirror. The total minutes for each active mirror are then summed up to get a number of mirror-hours for that run period. The Monte Carlo aperture calculation assumes a 22-mirror detector, so the total On-time for the detector is obtained by summing all the mirror-hours from each run period and then dividing by 22 to get an equivalent run time to use in the spectrum calculation.

A *weather-cut* is imposed on the event data used in the spectrum calculation. During data taking, the detector operator enters a notice in the log file regarding the weather conditions. The weather code entered reflects the presence/absence of clouds overhead and on the horizon. The code also indicates how good the visibility is. In analyzing the data the log files from each night were examined. All nights where the weather code indicated overhead clouds were excluded from the analysis. The loss in the amount of data due to this cut is very small ($\sim 10\%$), however the advantage is that the Monte Carlo calculated aperture reflects more accurately the actual detector aperture; The Monte Carlo simulation does not include clouds. Tables 9.5 and 9.6 show the results of the On-time calculation. Averaged over 22 mirrors the *Detector On-time* for the two year period is calculated from the values in table 9.6 (excluding the marked mirrors) to be $T = 943.7\,\text{hrs}$.

9.3 Energy Spectrum

The only element still missing from equation 9.3 is the event count in each energy bin. These are shown in table 9.8 and figure 9.2. To summarize, these events were collected from May 1997 to June 1999. Only, data taken on cloudless skies from mirrors 1-16, and mirror 20 are included in the final data set. The exclusion of mirrors 17-19 is due to the absence of reliable calibration information

Table 9.5. Detector On-time for each run period. Only run-nights which passed the good weather cut are included.

month	mir-hours	month	mir-hours
97/05	154.3	98/06	668.6
97/06	662.0	98/07	592.7
97/07	436.0	98/08	982.4
97/08	813.8	98/09	1119.9
97/09	430.2	98/10	1301.7
97/10	1295.2	98/11	1126.4
97/11	1282.0	98/12	1845.0
97/12	1397.4	99/01	1608.6
98/01	944.4	99/02	940.7
98/02	394.8	99/03	1158.2
98/03	585.0	99/04	1168.6
98/04	1061.9	99/05	628.7
98/05	533.0	99/06	535.5

Table 9.6. Detector On-time for each mirror, with good weather cut. Data from mirrors marked with an asterisk is not used in the analysis.

mirror	hours	mirror	hours
1	1182.9	12	1246.1
2	1094.8	13	1235.9
3	1238.6	14	1230.7
4	1229.5	15	1225.2
5	1226.3	16	1218.8
6	1204.9	17	670.2*
7	1235.7	18	0.0
8	1231.9	19	730.6*
9	1242.3	20	1231.0
10	1244.3	21	771.4*
11	1242.6	22	732.6*

Table 9.7. Number of Bigh events at each stage of data processing, starting with calibrated time matched events (PASS1) and ending with PASS3b.

pass number	event count
1	55.2×10^6
2	2.5×10^6
3	71,559
3a	11037
3b	3336

Table 9.8. Number of BigH events in each energy bin. bin centers are the base 10 logarithm of the energy in EeV.

$\log_{10}(E\,\mathrm{EeV})$	#events	$\log_{10}(E\,\mathrm{EeV})$	#events
0.05	253	1.35	36
0.15	288	1.45	32
0.25	265	1.55	15
0.35	255	1.65	20
0.45	220	1.75	9
0.55	216	1.85	4
0.65	163	1.95	2
0.75	144	2.05	4
0.85	132	2.15	1
0.95	102	2.25	1
1.05	60	2.35	0
1.15	56	2.45	1
1.25	46	2.55	0

for these mirrors at the time of this analysis. The total number of time matched events collected by the detector and the number of events remaining after each data processing stage are shown in table 9.7. As can be seen from the table, a total of 3336 events survived all the selection cuts up to PASS3b and had their energies reconstructed. Of these, some failed the quality cuts applied in PASS4 while others reconstructed with energies below 10^{18} eV. The rest, which add up to 2325 events, are distrinuted in energy as shown in table 9.8, as already mentioned.

The CR flux is known to follow a $j(E) \sim E^{-3}$ shape. To more easily resolve

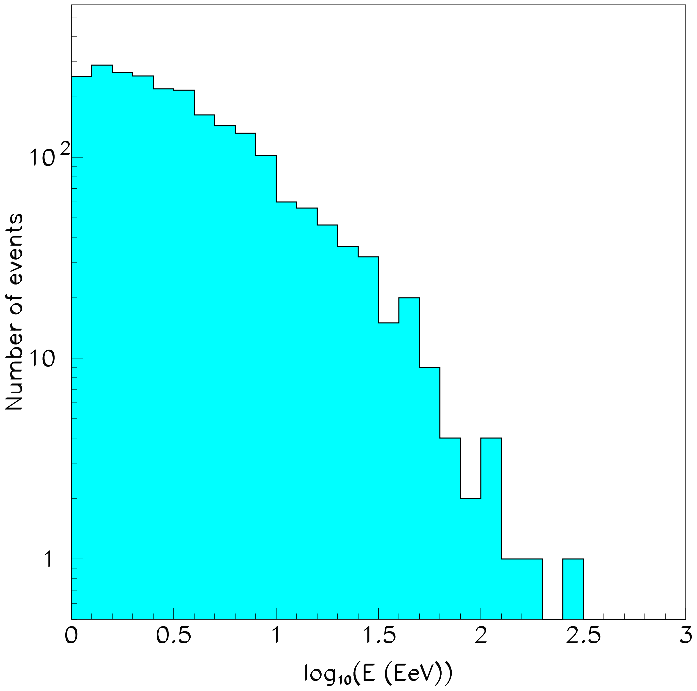

Figure 9.2. Number of BigH events in each energy bin.

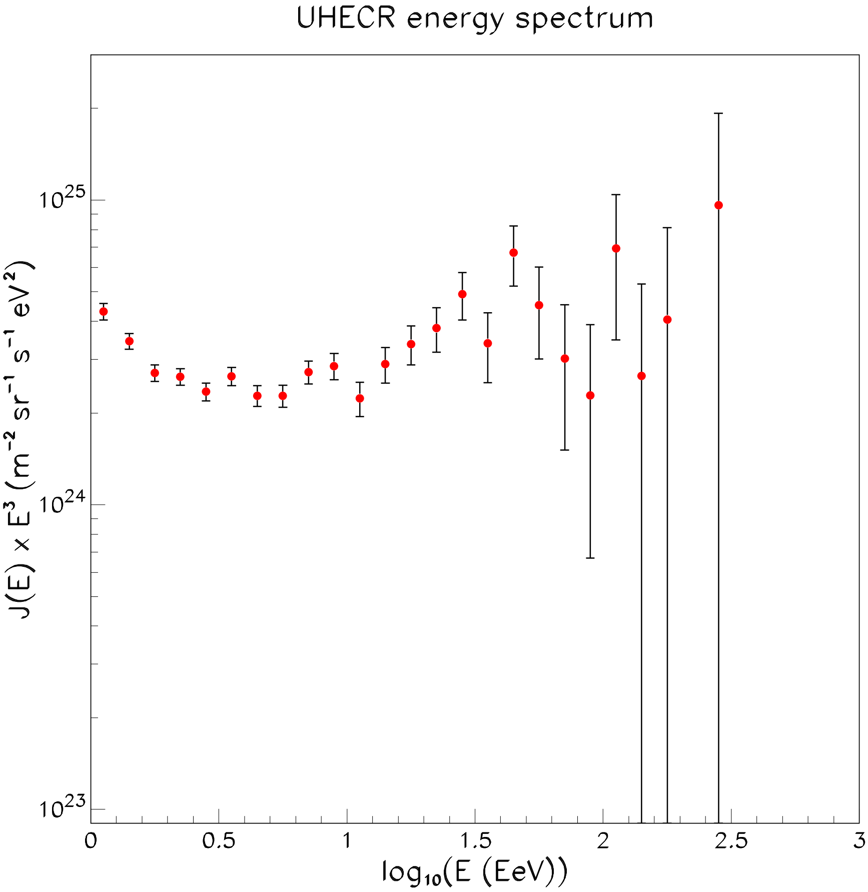

Figure 9.3. The UHECR spectrum as measured by the BigH detector.

features in the spectrum, it is customary to plot the flux multiplied by energy to the third power, i.e. $E^3 \times j(E)$. Figure 9.3 shows the CR energy spectrum measured by the BigH detector. This Spectrum is the end result of the analysis described in this thesis.

There are three key points to note about the measured spectrum: (a) The absolute normalization, (b) the “dip” around 5×10^{18} eV, and (c) the existence of events above the GZK cutoff. In the following, these points will discussed in turn.

The MC set generated according to the Fly’s Eye 2-component stereo spectrum was used to examine the measured spectrum. The number of MC events generated is equivalent to 2000 hrs of detector operation, i.e. just over twice the actual run time. The MC events were reconstructed and the results compared with real data, as shown in figure 9.4. The four parts of the figure in turn compare the measured spectrum to the following:

1. The 2-component "best fit" to the Fly's Eye stereo spectrum, extended beyond the cutoff. This spectrum is used as the input spectrum in the MC.
2. The reconstructed MC spectrum assuming no cutoff in the spectrum.
3. The reconstructed MC spectrum assuming a cutoff at 100 EeV.
4. The reconstructed MC spectrum assuming a cutoff at 60 EeV.

It can be seen from the figure that the absolute normalization of the flux is higher than that of the FE result. The four previous experiments (Haverah Park [41], AGASA [12], Yakutsk[10]) which produced results in this energy regime all came up with slightly different normalizations. Assuming the FE normalization is correct, then a 10% systematic overestimation of the energy on our part can result in the observed normalization. A slight underestimation of the detector aperture could also be responsible for the difference. These issues can not be resolved until a refined calibration and detailed atmospheric studies become available.

The expected "dip" in the spectrum at 3×10^{18} eV is observed in our measurement. However, comparing the MC input spectrum to the MC reconstructed spectrum shows that the spectrum index changes around 3×10^{18} eV are exaggerated in the reconstruction. This may be due to a systematic effect which is not well understood at this time. The reconstruction and the spectrum measurement are not expected to be accurate for this energy region for the following reasons:

1. From the resolution plots in section 8.3.4, it can be seen that the energy resolution is $\sim$ 30% for proton showers of a few EeV energies, and there is a $\sim$ 20% systematic error for iron showers.
2. The FE results [1] show evidence for a changing composition in this region. The profile constrained geometry fit, used in estimating the shower energies, is

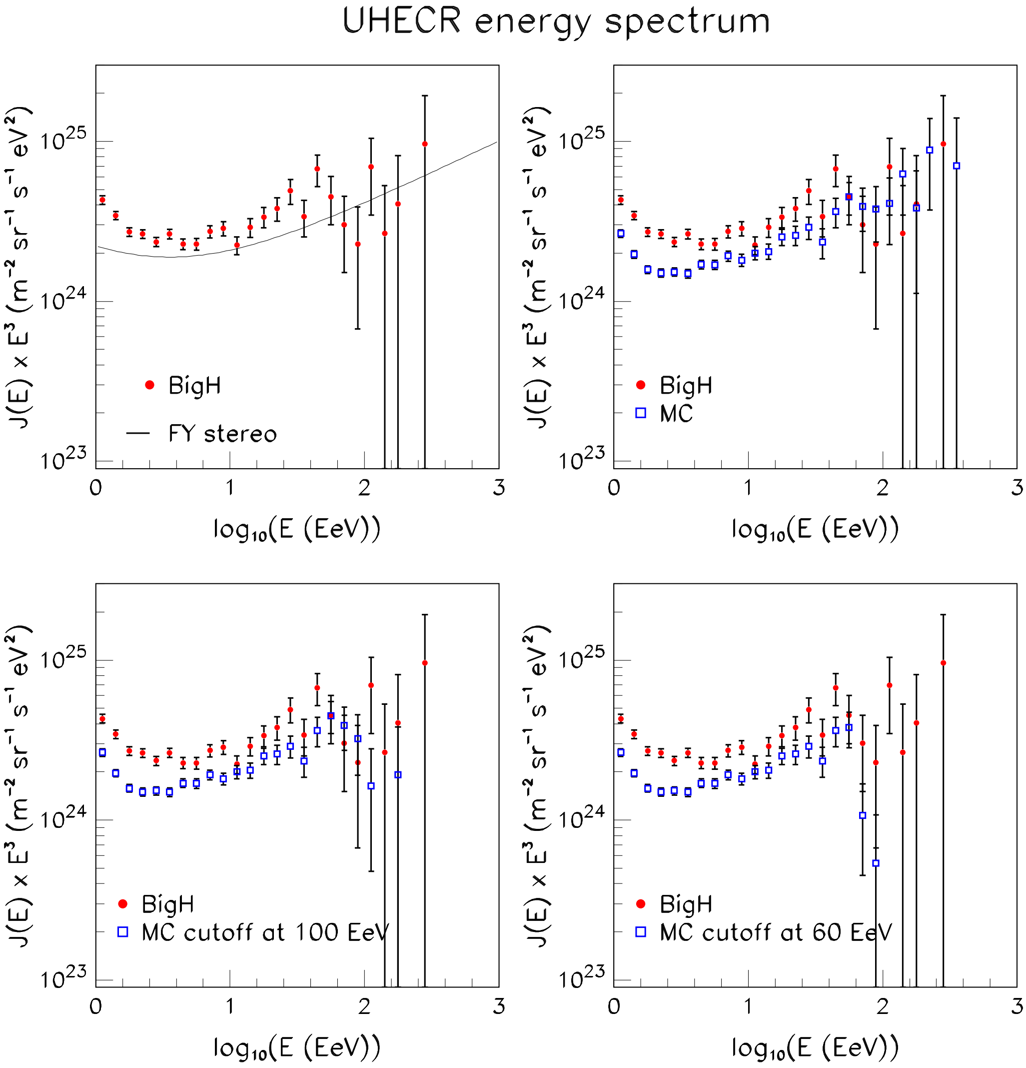

Figure 9.4. The UHECR spectrum as measured by the BigH detector. The spectrum is superimposed on a fit to the Fly's Eye stereo spectrum [1], and with spectra obtained from reconstructed MC sets (generated according to FE stereo spectrum) with different cutoff points as indicated.

Table 9.9. Number of BigH events observed above 60 EeV and 100 EeV compared with Monte Carlo predictions assuming no GZK cutoff and a sharp cutoff either at 60 EeV or 100 EeV. The Fly's Eye stereo spectrum is used for the Monte Carlo.

	BigH	MC: cutoff at 60 EeV	MC: cutoff at 100 EeV	MC: no cutoff
# events E > 60 EeV	13	2.5 ± 1.1	12.8 ± 2.5	21.7 ± 3.3
# events E > 100 EeV	7	< 1	1.9 ± 1.0	10.2 ± 2.3

sensitive to the actual x_{max} distribution of the showers, which in turn depends on the composition.

3. This energy range represents the energy threshold for the detector, an area where the MC may not reproduce the actual detector very well.

Finally, we come to the issue of the GZK cutoff. Figure 9.4 indicates that the flux continues beyond the predicted GZK cutoff at 60 EeV. In comparison with the MC results, the measured spectrum is inconsistent with a sharp cutoff at 60 EeV, however, it is consistent with a cutoff at 100 EeV or no cutoff. The results are summarized in table 9.9. Note that in this comparison, atmospheric corrections to individual events have not been applied. Atmospheric corrections may be quite significant for distant events. In the next section, events above 10^{20} eV are examined in some detail.

9.4 Events Above The GZK Cutoff

The data set contains 13 events with reconstructed energies greater than 63 EeV ($10^{19.8}$ eV,) of these, seven events have energies greater than 100 EeV. For each of these seven events, the following set of plots shows displays of the events and reconstruction results. For each event, the figures consist of four parts, these are:

1. Top left: Event display, showing pattern of triggered tubes and shower-detector plane. The event time shown is in UT.

2. Top right: Light flux into 1^o angular bins along the track. In this analysis, each bin corresponds to one tube. Points marked “C” correspond to bins that are flagged as over-corrected. These are tubes which lie from the SD plane which trigger due to multiply scattered light. These tubes have low photo-electron counts and have a very small effect on the χ^2_{pfl} calculation.

3. Bottom left: Track geometry fit, shows tube trigger times vs. tube viewing angles.

4. Bottom right: Light flux (from 2) vs. slant depth along the track. The upper window shows the different light contributions from scintillation and scattered Cerenkov light. The lower window shows the total light flux from the fit, with the measured points superimposed.

Although atmospheric corrections were not applied to the data, we can get a rough idea about the atmospheric conditions at the times these events were observed, from the ISF data (section 5.5.1.) Recall that the ratio of the total ISF signal in two bins, one at small scattering angle and the other at large scattering angle, is used to get an estimate of the amount of aerosols. More accurately, the observed ratio allows a comparison of the current conditions with the standard atmospheric model. The analysis does not allow, or has not been developed to the point of, drawing quantitative predictions about the aerosol model or the model parameters. From figure 5.5, it is seen that the average ratio, over the two years of observation, for the two bins is 2.64. The lower bound in the distribution, corresponding to molecular atmosphere, is close to a value of 1.5.

Figures 9.12 and 9.13 show the bin ratio for each set of ISF shots taken one hour before to one hour after each of the above events were observed. Since these events were reconstructed assuming an average atmosphere, the energy of the events is probably overestimated for those events observed on nights with better than average visibility. The figures below indicate that this might have been the case for some of these events.

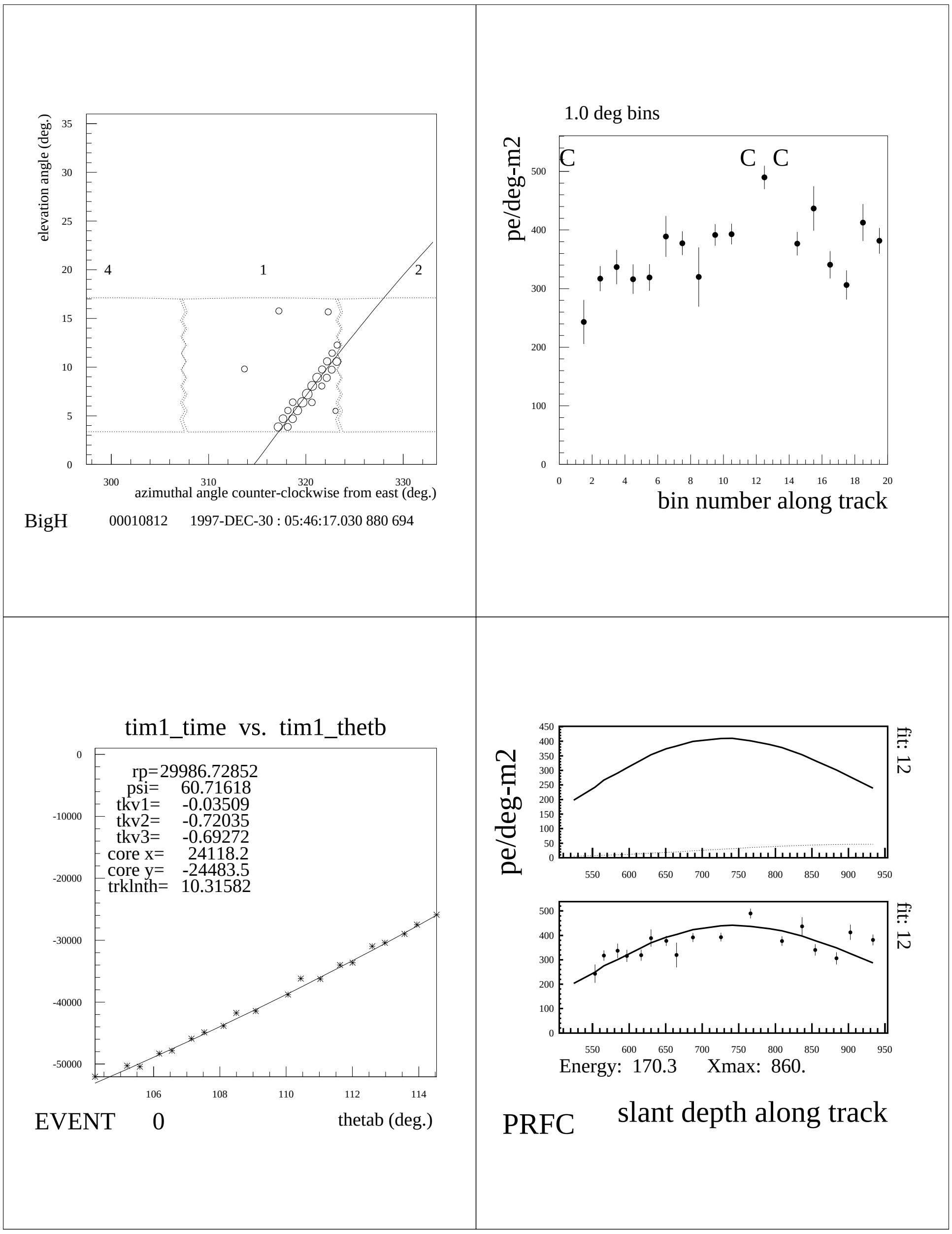

Figure 9.5. BigH event recorded on 12/30/1997.

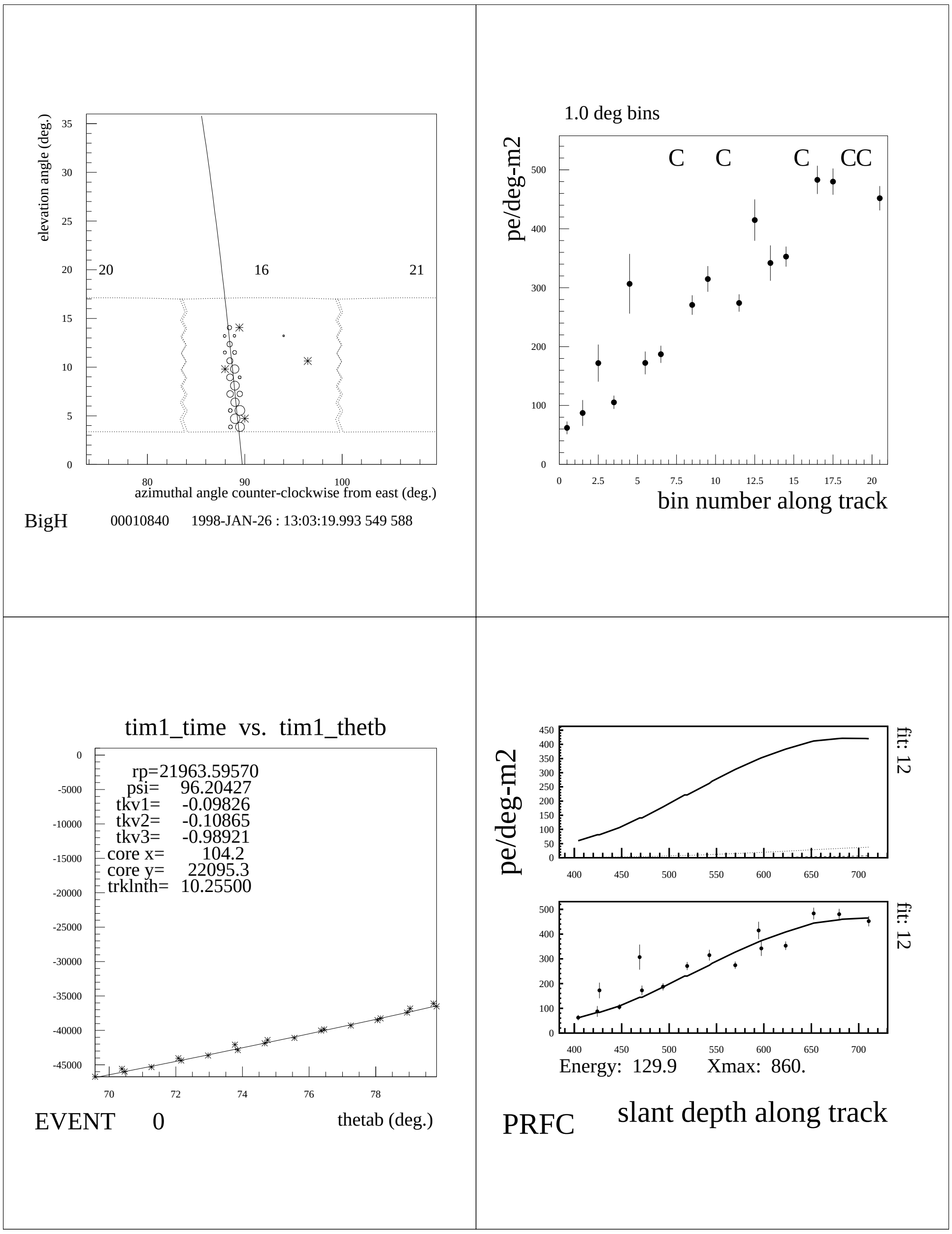

Figure 9.6. BigH event recorded on 01/26/1998.

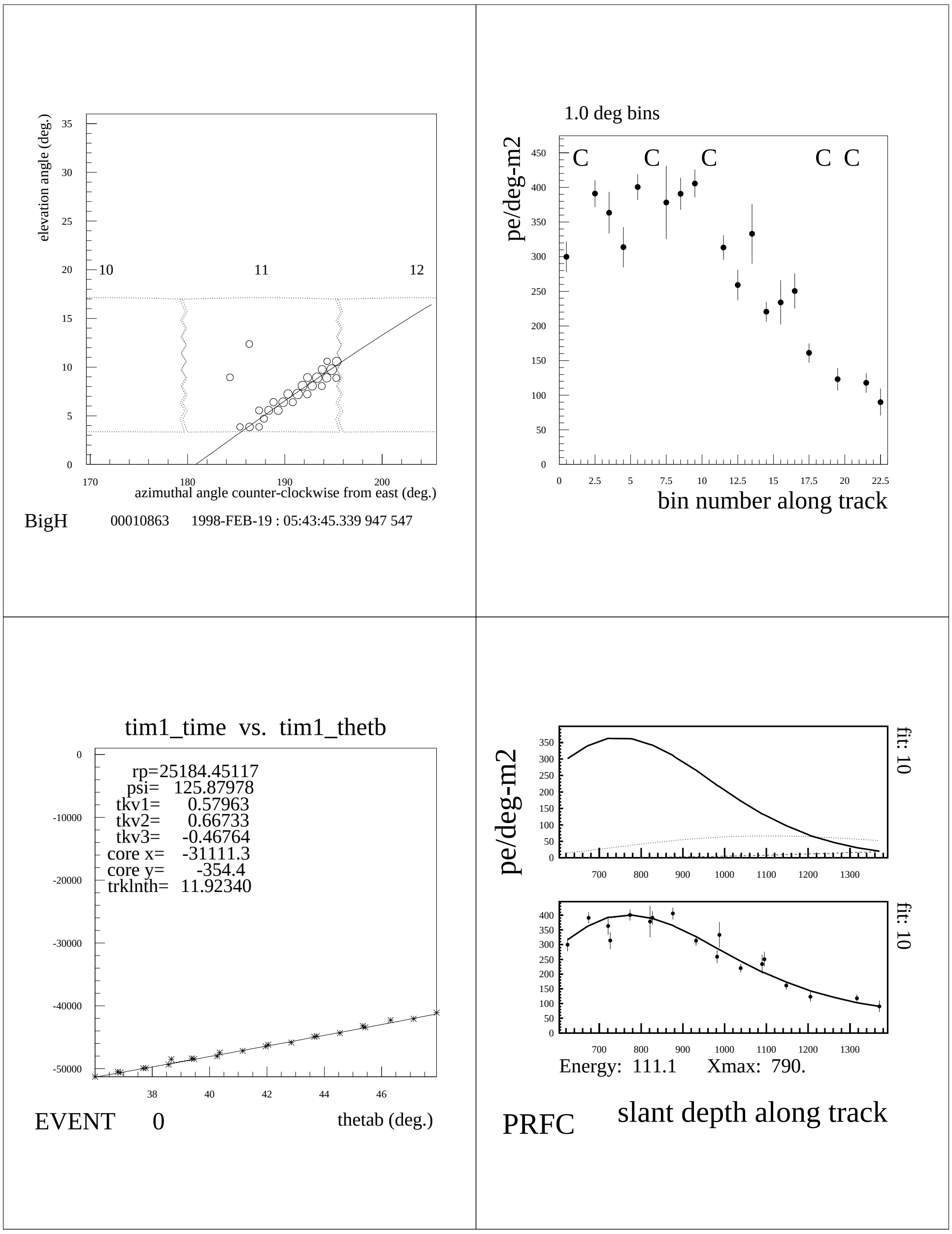

Figure 9.7. BigH event recorded on 02/19/1998.

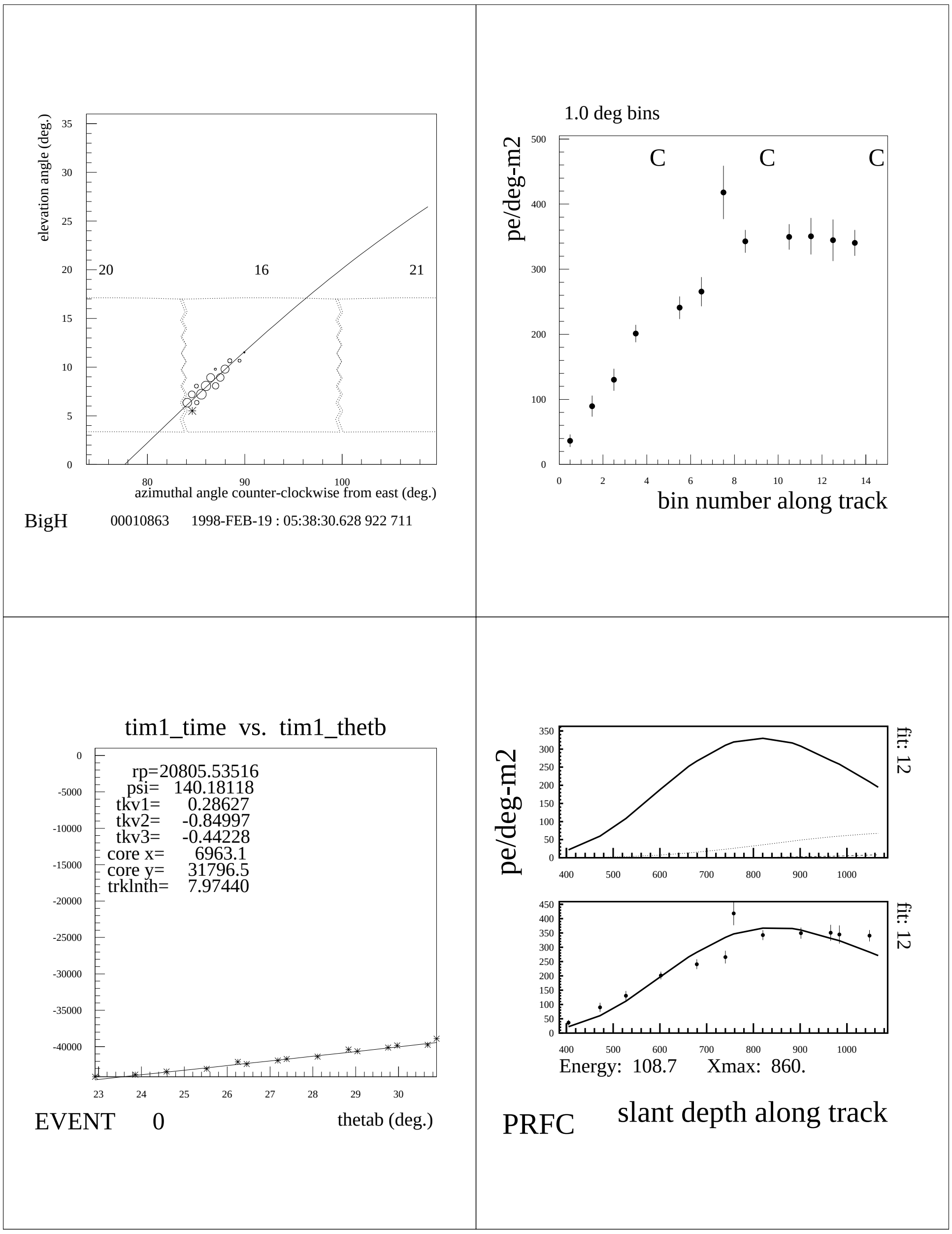

Figure 9.8. BigH event recorded on 02/19/1998. Second event on the same night.

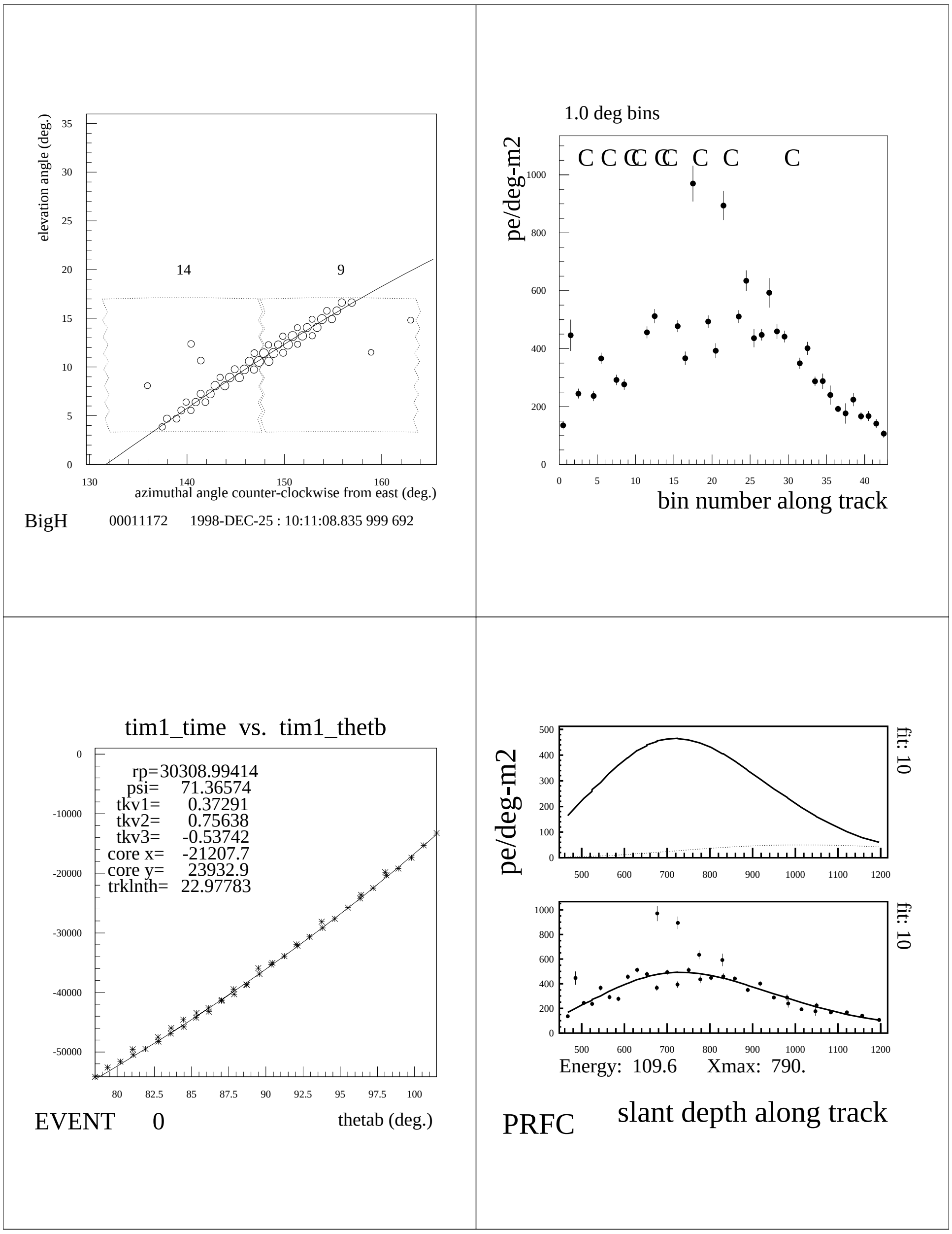

Figure 9.9. BigH event recorded on 12/25/1998.

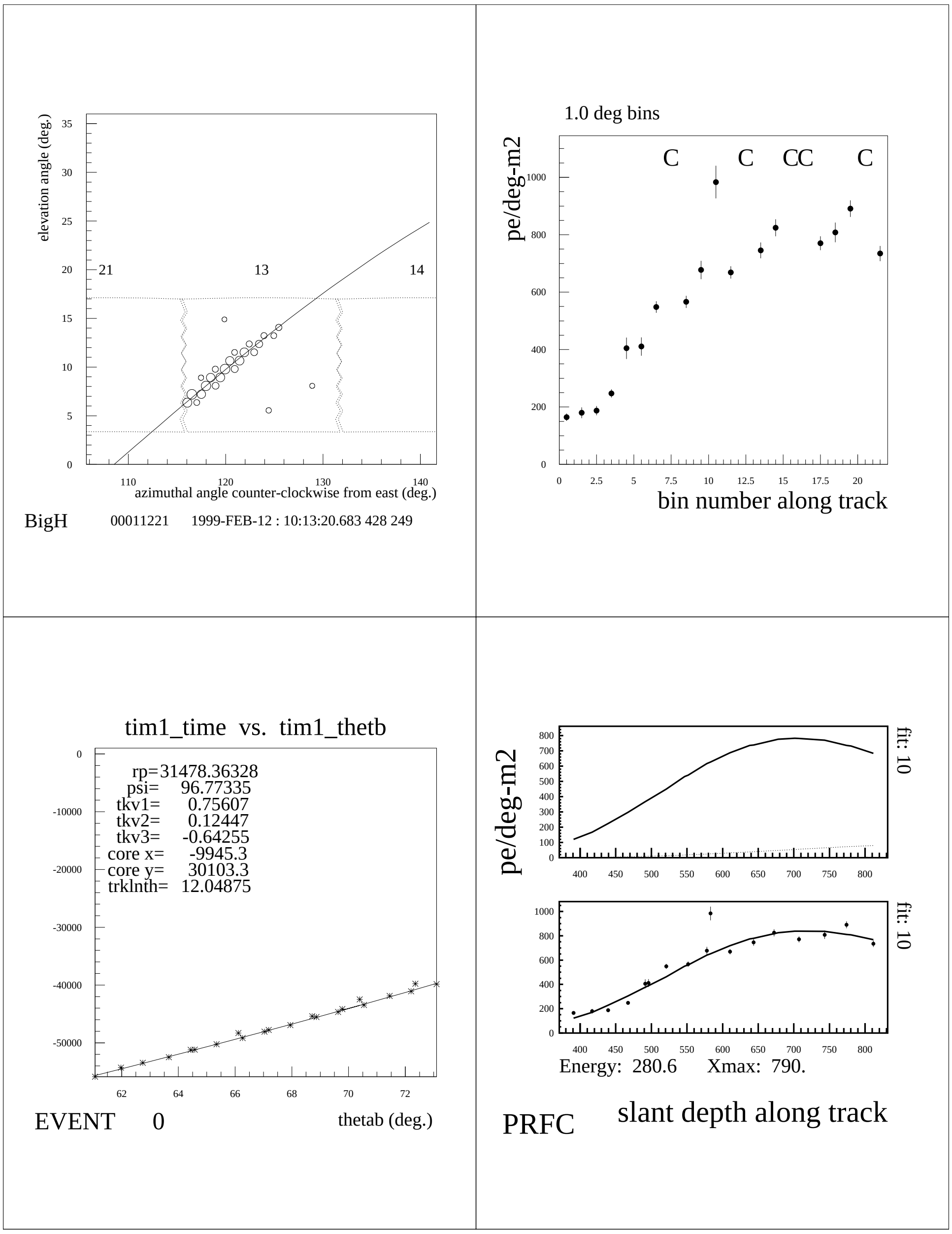

Figure 9.10. BigH event recorded on 02/12/1999. Highest energy event seen by BigH.

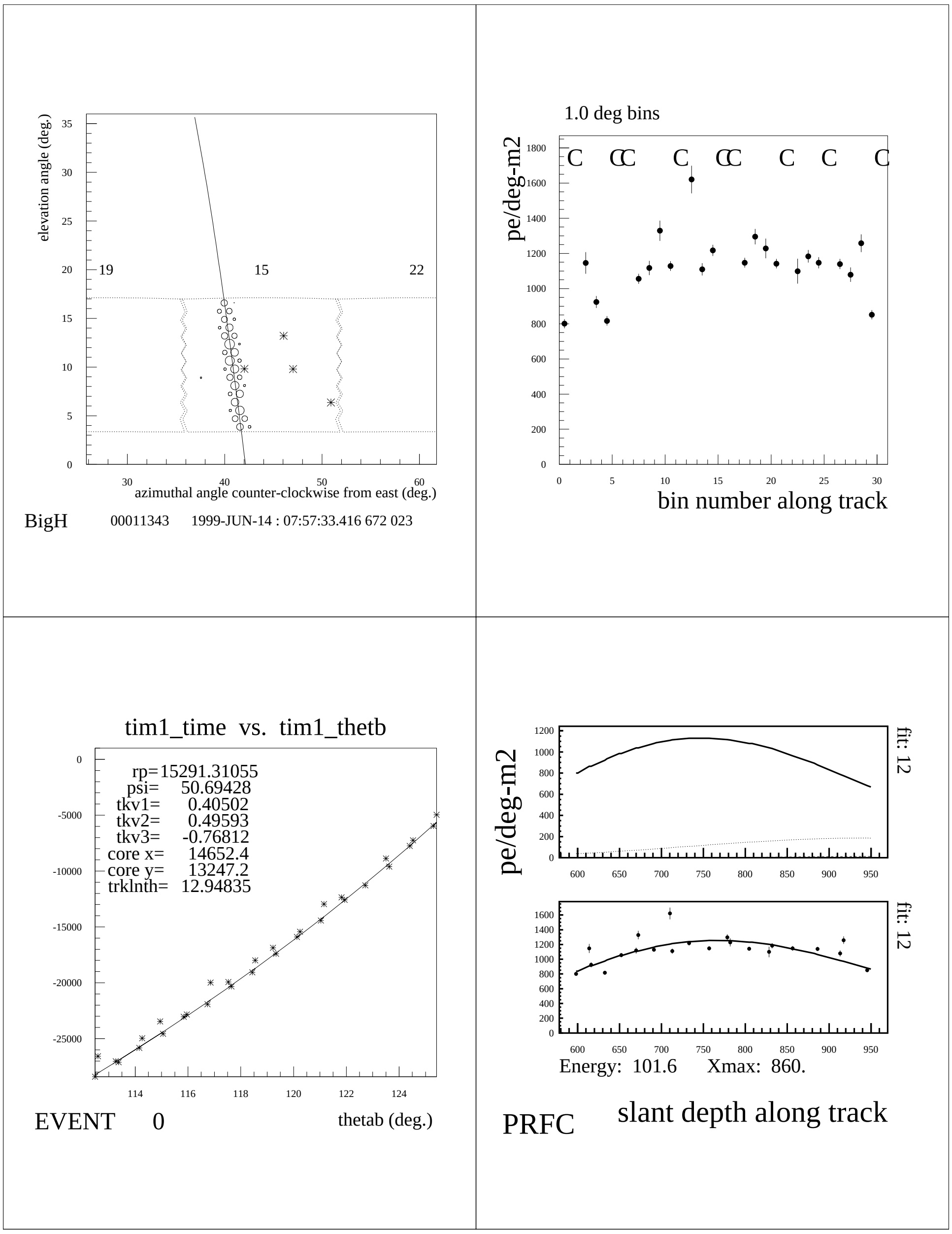

Figure 9.11. BigH event recorded on 06/14/1999. Event was also seen by HiRes-II detector. One of the first, and the highest energy, stereo events seen.

Table 9.10. Reconstructed energies for seven highest energy events assuming three different aerosol concentrations specified by the value of the aerosol horizontal extinction length.

event	E[EeV]: $L_M = 12\,\text{km}$	E[EeV]: $L_M = 15\,\text{km}$	E[EeV]: $L_M = \infty$
1	170.2	137.0	59.3
2	129.8	100.7	43.4
3	111.1	111.5	72.8
4	108.6	95.2	55.4
5	109.5	105.7	68.6
6	280.6	261.1	163.4
7	101.5	88.2	47.0

A lower bound on the energy is obtained if we assume a molecular atmosphere in the reconstruction. The standard atmosphere used in the analysis assumes an aerosol horizontal extinction length $L_M = 12\,\text{km}$ at 334 nm (see section 6.3.2). To obtain a lower bound on the energy and to study the systematic effects of the atmospheric model assumption, the data was reconstructed with different atmospheric parameters, namely $L_M = 15\,\text{km}$ and $L_M = \infty$ (molecular atmosphere). The reconstructed energies of the seven high energy events, for the different L_M values are shown in table 9.10. As can be seen from the table, changing the atmospheric parameters can significantly affect the energy assignment. This is especially true six of these events had impact parameters in excess of 20 km (15 km for the seventh event).

The uncertainty introduced by not knowing the actual atmospheric conditions at the time of measurement makes it very difficult to draw conclusions concerning the shape of the energy spectrum near the GZK cutoff. Only one event is reconstructed with energy above 100 km with an assumption of a molecular atmosphere.

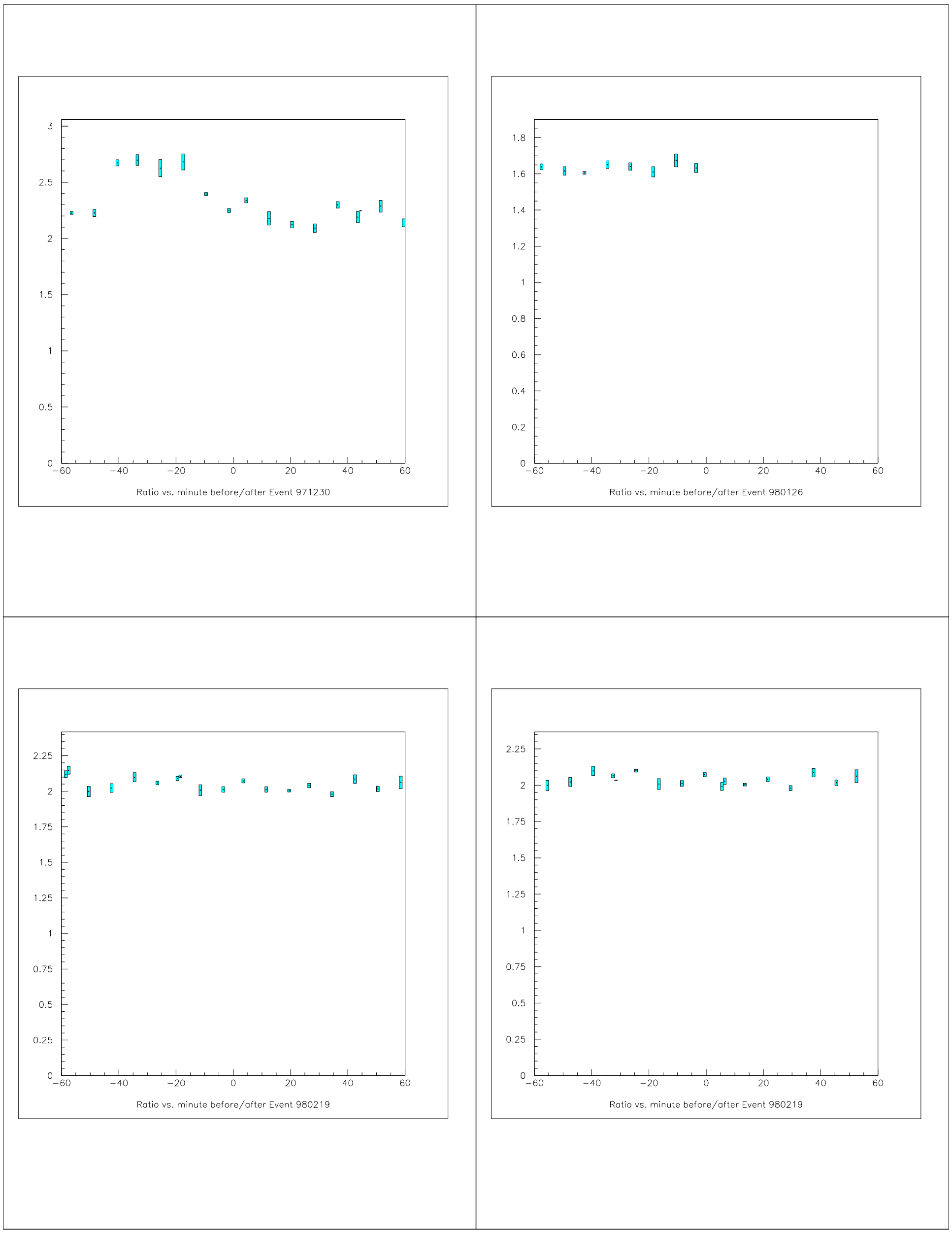

Figure 9.12. Ratio vs. minute for a time window of one hour around events 1 through 4.

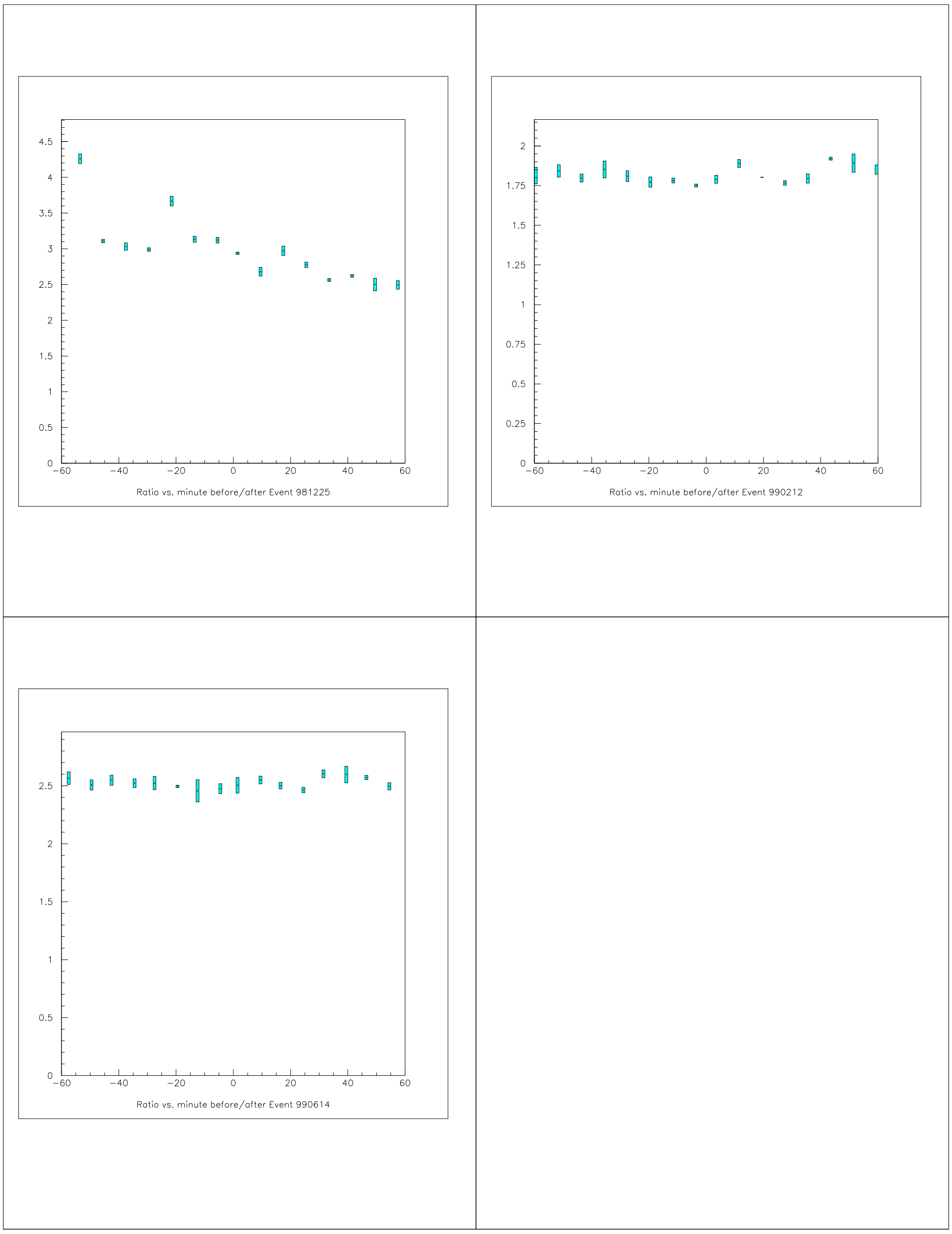

Figure 9.13. Ratio vs. minute for a time window of one hour around events 5 through 7

CHAPTER 10

SUMMARY

The HiRes-I (BigH) detector was used to measure the cosmic rays energy spectrum at energies greater than 10^{18} eV. A main focus of the measurement was the observation of the predicted GZK cutoff at 6×10^{19} eV. Chapter 2 provided a quick review of the physics and recent results concerning the energy spectrum and the GZK cutoff.

The detector construction (re-deployment) began in early 1997 and data taking began in May of the same year. Two years worth of data were taken and included in this study. The detector hardware and the detector optimization were described in chapter 4, while chapter 5 described the detector calibration.

HiRes-I events were observed in monocular mode. This, combined with the fact that the observed angular tracklengths of these events are too short for a reliable track reconstruction (section 8.3.1), meant that a new event reconstruction method had to be developed. This method is referred to as the *profile constrained geometry fit,* and was discussed in section 8.3. In short, the method allowed for a reasonably good energy reconstruction by assuming, a priori, the shower profile parameters.

The energy spectrum calculation involved:

- The energy reconstruction and binning of all observed events over the two year period the detector was run.
- The detector On-time calculation.
- The detector aperture calculation.

The details of these calculations were given in chapter 9. Also presented were the measurement results.

The main results of this study can be summarized as follows:

- The measured spectrum (figure 9.3) is consistent with previous measurements done by the Fly's Eye and other groups.
- The spectrum appears to continue beyond the predicted GZK cutoff, i.e. a number of events with reconstructed energies in excess of the nominal cutoff value of 6×10^{19} eV were observed.

No clear cut conclusions can be drawn about the presence/absence of a cutoff however. See section 9.3 and, in particular, table 9.9 for details. The reasons for this are: (a) the lack of sufficient statistics, (b) uncertainities in the detector calibration, (c) the use of an average atmospheric model and not applying nightly atmospheric corrections to the data, and (d) possible energy reconstruction bias which, in the case of a steeply falling spectrum, can have a significant effect. Below is a discussion of some of these issues.

The results presented are based on an analysis that assumed average atmospheric conditions (aerosol concentration and profile). The actual conditions which can vary on a time scale of an hour or less (unstable atmosphere) or more typically from night to night, can *significantly* affect the estimated energy of distant showers. A detailed atmospheric calibration program is being implemented by other members of the HiRes group and, where possible, will be incorporated in the data analysis. Also, a more accurate detector calibration (PMT and electronics) procedure is near completion. The HiRes-I data will be reanalyzed using this new calibration method. These calibration procedures and the reanalysis of the HiRes-I data using them are beyond the scope of this thesis.

Moreover, the monocular data analysis will need to be cross checked against the stereo analysis. HiRes-II has been taking data along with HiRes-I since the middle of 1999. The stereo geometry reconstruction is simple and accurate. Events observed in stereo will be analyzed using both monocular and stereo methods, and the results from each reconstruction procedure will be compared. The comparison may guide us in making modifications to the monocular reconstruction algorithms to improve the reconstruction procedure. However, even if no improvements were made, the stereo results can present us with a better understanding and a more quantitative estimate of the errors inherent in the monocular analysis. A handfull of stereo events have been used for an anecdotal comparison and the results were satisfactory.

APPENDIX

ERROR ESTIMATES AND POISSON STATISTICS

This appendix discusses some issues relating to error estimates and the error bars shown in the energy spectrum plots in chapter 9. The calculation and definition of the error bars are discussed with special attention given to the special case of "small signals".

The error bars shown in figures 9.3 and 9.4 represent the *statistical errors* of the measurement. That is, we have ignored any systematic errors introduced by the detector and atmospheric calibrations, energy reconstruction, or the aperture calculation, and included only the effects of the fluctuation of the number of observed events. Using the law of propagation of errors and equation 9.3 we can write:

$$\delta j(E_i) = \frac{1}{TA\Omega(E_i)\Delta E} \times \delta(\Delta N_i) \tag{A.1}$$

where $\delta(\Delta N)$ is the error in the number of events, and δj is the corresponding error in the flux. For notational convenience we rename ΔN as n in what follows.

More specifically, the error bars used in the spectrum plots correspond to the *standard error* of the measurement, i.e. $j \pm \sigma_j$ $(n \pm \sigma_n)$, with σ_j, σ_n being the standard deviations of j, n respectively. The fact that the measured quantities in these plots are the number of events in each energy bin implies that the relevant underlying probability distribution is the Poisson distribution. The Poisson distribution has the property that its variance is equal to its mean, $\sigma^2 = \mu$, this follows from the definition of the Poisson probability density function. This fact results in the observation that, for a bin with n events, the standard error is given by $\sigma_n = \sqrt{n}$, i.e. the error bars correspond to $n \pm \sqrt{n}$. The use of the "sample" standard deviation $\sqrt{n}$ in place of the standard deviation of the underlying distribution $\sqrt{\mu}$ is a good approximation for large n.

The simple picture presented above fails in the case where the number of observed events is small, $n \leq 5$. To deal with this situation we need to restate the problem of setting error bars in terms of setting confidence intervals around a measured value, as described in the following paragraphs.

Consider a parameter μ whose true value is μ_t and measured value is n. A confidence interval (μ_1, μ_2) can be constructed around n such that the probability that μ_t lies in the interval is given by a pre-specified value $1-\epsilon$. i.e. $1-\epsilon = P(\mu_1 < \mu < \mu_2)$. The Confidence Level (CL) is defined by $CL\% = 100(1-\epsilon)\%$.

For a normally distributed variable μ with a known standard deviation σ, the confidence intervals are centered on the measured value n and are given by $n \pm z_{\epsilon/2} \cdot \sigma$ where $z_{\epsilon/2}$ is defined by $P(Z > z_\alpha) = \alpha$ for the standard normal distribution (mean = 0, standard deviation = 1). In the case that the distribution of the measured values (from repeated experiments) satisfies the central limit theorem, the same relation can be used even if the variable belongs to a non-Gaussian distribution

Certain confidence levels usually quoted in the literature are 68.27%, 95.45%, and 99.73%. For a Gaussian distribution these correspond to intervals $n \pm \delta$ with $\delta = 1\sigma$, 2σ, and 3σ respectively. In cases where the central limit theorem can be applied, the same conventional values are used for variables drawn from non-Gaussian distributions as well, although the correspondence is understood to be only approximate. Compared with the discussion at the beginning of this appendix it can be seen that the 68.27% confidence level is equivalent to the standard error.

For our particular problem of estimating the confidence intervals on the measured flux, or number of observed events, we use the relation $n \pm \delta$ with $\delta = 1\sigma$. When a large number of events is observed the central limit theorem applies and our usage is correct. If the observed number of events is small then the central limit theorem can not be used and the approximation fails. In this case we can appeal to tabulated values for the lower and upper limits of the confidence interval.

Table A.1. A comparison of the 68.27% confidence levels for Poisson data from [42] and the simple calculation used for the spectrum plots. Here, n is the total number of observed events, μ_1, μ_2 are the lower, upper limits of the confidence intervals given by [42], and $n \pm \sqrt{n}$ are the corresponding values used in our calculation. A mean background $b = 0$ is assumed in the quoted figures for μ_1 and μ_2.

n	μ_1	μ_2	$n - \sqrt{n}$	$n + \sqrt{n}$
0	0.00	1.29	0.00	0.00
1	0.37	2.75	0.00	2.00
2	0.74	4.25	0.59	3.41
4	2.34	6.78	2.00	6.00
9	6.33	12.79	6.00	12.00
15	11.32	19.32	11.13	18.87
20	15.83	25.30	15.53	24.47

The paper by Feldman and Cousins [42] discusses the construction of confidence intervals in the case of small Poisson signals (e.g. small event count). The paper also contains a number of tables that can be consulted for particular numbers. Table A.1 compares the confidence intervals from [42] with the simple calculation used in plotting the error bars in the spectrum plots of chapter 9. As can be seen from the table, for the case $n = 1$ which in the spectrum plots has an error bar that extends to the bottom of the page, the use of the more accurate confidence interval estimate would result in a “better behaved” representation.

REFERENCES

[1] D. J. Bird et al. Evidence for correlated changes in the spectrum and composition of cosmic rays at extremely high energies. *Physical Review Letters*, 71(21):3401–3404, 1993.

[2] D. J. Bird et al. Study of broad-scale anisotropy of cosmic-ray arrival directions from 2×10^{17} to 10^{20} electron volts from fly's eye data. *The Astrophysical Journal*, 511:739–749, feb 1999.

[3] Peter L. Biermann. The origin of the highest energy cosmic rays. *J. Phys. G: Nucl. Part. Phys.*, 23:1–27, 1997.

[4] Shigeru Yoshida and Hongyue Dai. The extremely high energy cosmic rays. *J. Phys. G: Nucl. Part. Phys.*, 24(5):905–938, May 1998.

[5] K. Greisen. Hello there. *Physical Review Letters*, 16:748, 1966.

[6] G. T. Zatsepin and V. A. Kuzmin. How do you do. *Sov. Phys. JETP Lett.*, 4:78, 1966.

[7] D. J. Bird et al. Detection of a cosmic ray with measured energy well beyond the expected spectral cutoff due to cosmic microwave radiation. *Astrophysical Journal*, 441(1):144–150, 1995.

[8] N. N. Kalmykov and G. B. Khristiansen. Cosmic rays of superhigh and ultrahigh energies. *J. Phys. G: Nucl. Part. Phys.*, 21:1279–1301, 1995.

[9] M. A. K. Glasmacher et al. The cosmic ray composition between 10^{14} and 10^{16} ev. *Astroparticle Physics*, 12:1–17, 1999.

[10] B. N. Afanasiev et al. The primary spectrum of cosmic rays of energy above 10^{18} ev by the yakutsk eas array data. In *24th ICRC*, volume 2, page 756, Rome, 1995.

[11] M. Nagano et al. Energy spectrum of primary cosmic rays above $10^{17.0}$ ev determined from extensive air shower experiments at akeno. *Journal of Physics G.*, 18:423–442, 1992.

[12] S. Yoshida et al. Empty. *Astropart. Phys.*, 3:105, 1995.

[13] M. Takeda et al. Extension of the cosmic-ray energy spectrum beyond the predicted greisen-zatsepin-kuz'min cutoff. *PRL*, 81(6):1163–1166, aug 1998.

[14] B. R. Dawson, R. Meyhandan, and K. M. Simpson. A comparison of cosmic ray composition measurements at the highest energies. *Astroparticle Physics*, 9:331–338, 1998.

[15] A. M. Hillas. The origin of ultra-high-energy cosmic rays. *Annual Reviews of Astronomy and Astrophysics*, 22:425–444, 1984.

[16] S. Yoshida, H. Dai, C. C. H. Jui, and P. Sommers. Extremely high energy neutrinos and their detection. *The Astrophysical Journal*, 479:547–559, apr 1997.

[17] P. Bhattacharjee, C. T. Hill, and D. N. Schramm. Grand unified theories, topological defects, and ultrahigh-energy cosmic rays. *Physical Review Letters*, 69:567–570, jul 1992.

[18] S. J. Sciutto. *AIRES A system for air shower simulations*, 1998.

[19] D. Heck et al. *CORSIKA: A Monte Carlo Code to Simulate Extensive Air Showers*, 1998.

[20] *Extensive Air Showers*, chapter 2, page 22. World Scientific Publishing Co. Pte. Ltd., 1998.

[21] John Linsley. Structure of large air showers at depth 834 g cm^{-2} applications. In *15th ICRC*, volume 12, pages 89–96, Plovdiv, 1977.

[22] Thomas K. Gaisser. *Cosmic Rays and Particle Physics*, chapter 15, page 226. Cambridge University Press, 1990.

[23] Alan Newton Bunner. *Cosmic Ray Detection by Atmospheric Fluorescence.* PhD thesis, Cornell University, 1967.

[24] M. J. Kidd. *Properties of Extensive Air Showers Around* 10^{17} *eV.* PhD thesis, University of Illinois at Urbana-Champaign, 1997.

[25] C. R. Wilkinson. *The Application of High Precision Timing in the High Resolution Fly's Eye Cosmic Ray Detecto.* PhD thesis, University of Adelaide, 1998.

[26] Jerome W. Elbert. The hires filter and its effect on the aperture. In *Proceedings of the Tokyo Workshop on Techniques for the study of Extremely High Energy Cosmic Rays*, page 232, Tokyo, 1993.

[27] D. Bird et al. The calibration of photomultiplier tubes in the hires experiment. In *Proceedings of the Tokyo Workshop on Techniques for the study of Extremely High Energy Cosmic Rays*, page 269, Tokyo, 1993.

[28] J. N. Matthews et al. The absolute calibration of hires-i. Internal HiRes document, 1997.

[29] T. Abu-Zayyad et al. The hires detector: Absolute calibration and alignment. In *25th ICRC*, volume 5, page 333, Durban, 1997.

[30] T. Abu-Zayyad et al. Radio controlled light sources for atmospheric monitoring at hires. In *25th ICRC*, volume 5, page 357, Durban, 1997.

[31] T. Abu-Zayyad et al. Atmosperic monitoring at the high resolution fly's eye: Data from the hires2 flasher array. In *25th ICRC*, volume 5, page 361, Durban, 1997.

[32] T. Abu-Zayyad et al. Atmosperic monitoring at the high resolution fly's eye: Monitoring data via the hires laser/lidar system. In *25th ICRC*, volume 5, page 365, Durban, 1997.

[33] Pierre Sokolsky. Sky noise and atmospheric transmission. In *Proceedings of the Tokyo Workshop on Techniques for the study of Extremely High Energy Cosmic Rays*, page 280, Tokyo, 1993.

[34] John Linsley. Empty. In *18th ICRC*, volume 12, page 135, Bangalore, 1983.

[35] R. M. Baltrusaitis et al. The utah fly's eye detector. *Nuclear Instruments and Methods in Physics Research*, A240:410–428, 1985.

[36] *Introduction to Ultrahigh Energy Cosmic Ray Physics*, chapter 5, page 51. Addison-Wesley Publishing Company, Inc., 1989.

[37] F. Kakimoto et al. A measurement of the air fluorescence yield. *NIM A*, 372, 1996.

[38] *Introduction to Ultrahigh Energy Cosmic Ray Physics*, chapter 15, page 201. Addison-Wesley Publishing Company, Inc., 1989.

[39] Mengzhi Luo. *Troposheric Aerosol Study by Fly's Eye and Lidar Technique.* PhD thesis, University of Utah, 1991.

[40] D. J. Bird et al. Preliminary analysis of monocular hires prototype data. In *24th ICRC*, volume 3, page 500, Roma, 1995.

[41] M.A. Lawrence, R.J.O. Reid, and A.A. Watson. Empty. *J. Phys. G*, 17:773, 1991.

[42] G. J. Feldman and R. D. Cousins. Unified approach to the classical statistical analysis of small signals. *Physical Review D*, 57:3873, 1998.